nagra.

Arbeitsbericht
NAB 16-22

**Pre-dismantling THM modelling
of the FEBEX in situ experiment**

June 2017

A. Papafotiou, C. Li & F. Kober (Eds.)

Contributors:
Y.F. Qiao, A. Ferrari, L. Laloui, M. Sánchez,
A. Gens & M. Åkesson

nagra.

Arbeitsbericht
NAB 16-22

Pre-dismantling THM modelling of the FEBEX in situ experiment

A. Papafotiou[1], C. Li[1,2] & F. Kober[3] (Eds.)

Contributors:
Y.F. Qiao[1], A. Ferrari[1], L. Laloui[1], M. Sánchez[4],
A. Gens[4] & M. Åkesson[5]

[1] INTERA Inc.
[2] EPFL
[3] Nagra
[4] CIMNE
[5] Clay Technology

**National Cooperative
for the Disposal of
Radioactive Waste**

Hardstrasse 73
P.O. Box 280
5430 Wettingen
Switzerland
Tel. +41 56 437 11 11

www.nagra.ch

Nagra Arbeitsberichte ("Working Reports") present the results of work in progress that have not necessarily been subject to a comprehensive review. They are intended to provide rapid dissemination of current information.

Table of Content

List of Tables

List of Figures

1   Introduction and purpose of this document

1.1   The FEBEX Project

FEBEX (Full-scale Engineered Barrier Experiment in Crystalline Host Rock) is a research and demonstration project that was initiated by ENRESA (Spain).

The aim of the project is to study the behaviour of near-field components in a repository for high-level radioactive waste in granite formations. The main objectives of the project may be grouped in two areas:

demonstration of the feasibility of constructing the engineered barrier system in a horizontal configuration according to the Spanish concept for deep geological storage (AGP-abbreviation in Spanish), and analysis of the technical problems to be solved for this type of disposal method

to develop a better understanding of the thermo-hydro-mechanical (THM) and thermo-hydro-geochemical (THG) processes in the near-field, and development and validation of the modelling tools required for interpretation and prediction of the evolution of such processes

The project consists of two large-scale tests (see Fig. 1-1) – "in situ" and "mock-up" (the latter is managed by CIEMAT in Spain) –, a series of laboratory tests, and THM and THG modelling tasks.

The full-scale heating test ("in-situ" test), to which this document refers, was performed at the Grimsel underground laboratory in Switzerland, also known as Grimsel Test Site (GTS) or Felslabor Grimsel (FLG in German). A complete description of the FEBEX project objectives and test program may be found in the "FEBEX Full-scale Engineered Barriers Experiment in Crystalline Host Rock. PRE-OPERATIONAL STAGE SUMMARY REPORT" (Fuentes-Cantillana et al. 1998a).
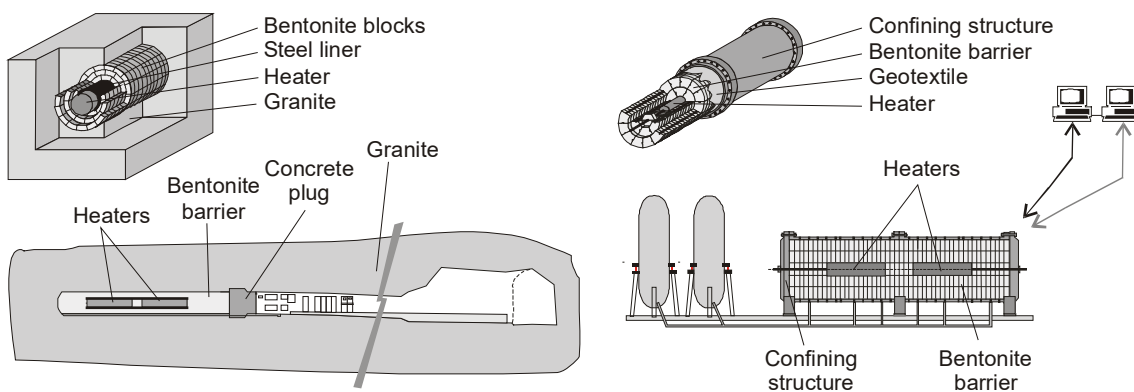
Fig. 1-1:   Overall layout of FEBEX "in situ" test (left) and "mock-up" test (right).

The project started in 1994, and has been supported by the European Commission through consecutive contracts, identified as FEBEX I (Contract No. FI4W-CT-95-0006) for the period January 1996 to June 1999, and FEBEX II (Contract No. FIKW-CT-2000-00016), from September 2000 to December 2004. Afterwards, NF-PRO took over from January 2005 to December 2007. Finally, in January 2008, the "in-situ" test was transferred from ENRESA to a consortium composed of SKB (Sweden), POSIVA (Finland), CIEMAT (Spain), Nagra (Switzerland) and more recently KAERI (South Korea), the FEBEXe Consortium, which supports it currently.

The "in-situ" experiment excavation was carried out in 2015 and new partners, interested in taking part in the planned sampling and analysis operations, have been incorporated in the Consortium (now called FEBEX-DP) for that purpose, namely US DOE (USA), OBAYASHI (Japan), RWM (UK), ANDRA (France), BGR (Germany) and SURAO (Check Republic).

1.2 Test configuration during FEBEX I

The installation of the "in-situ" test was carried out at the GTS. A horizontal drift with a diameter of 2.28 m was excavated in the Grimsel granodiorite especially for this experiment using a TBM (a tunnel boring machine). Two electrical heaters, of the same size and of a similar weight as the reference canisters, were placed in the axis of the drift. The gap between the heaters and the rock was backfilled with compacted bentonite blocks, up to a length of 17.40 m, this requiring a total 115'716 kg of bentonite. The backfilled area was sealed with a plain concrete plug placed into a recess excavated in the rock and having a length of 2.70 m and a volume of 17.8 m^3. Fig. 1-2 shows schematically the dimensions and layout of the test components.
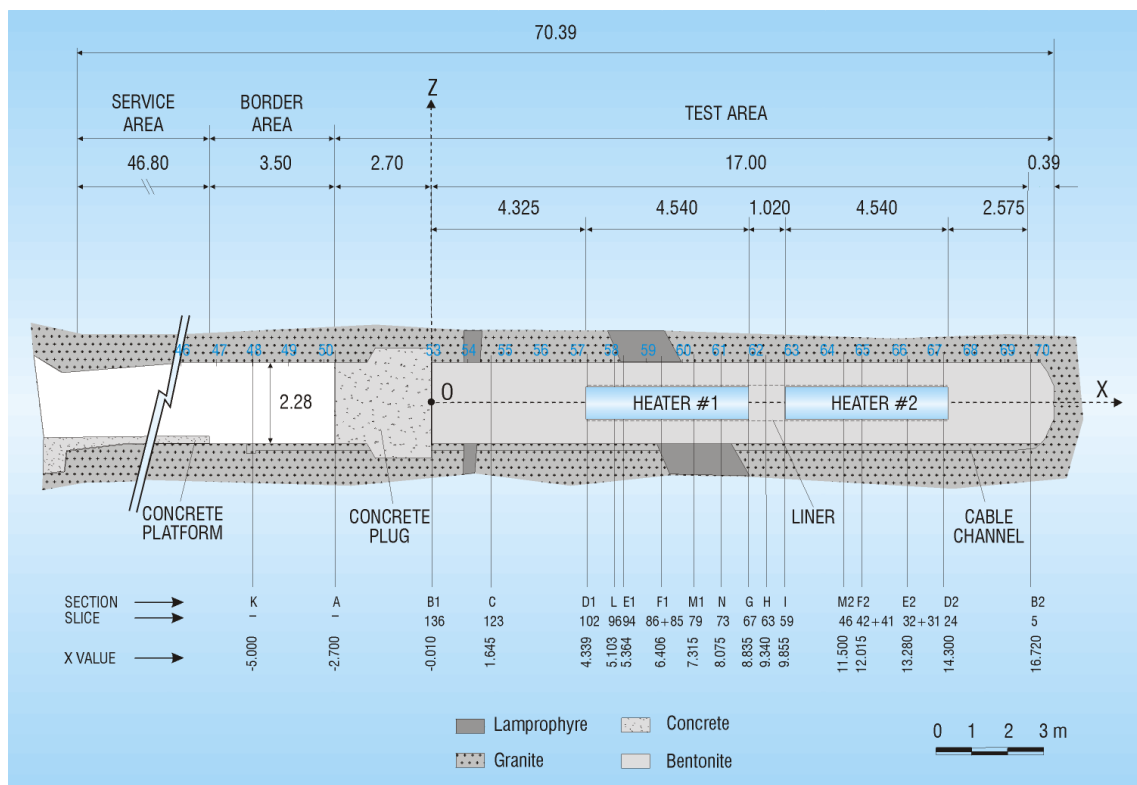
Fig. 1-2:   General layout of the FEBEX "in-situ" test (FEBEX I configuration).

A total of 632 instruments were placed in the system along a number of instrumented sections, both in the bentonite buffer and in the host rock, to monitor relevant parameters such as temperature, humidity, total and pore pressure, displacements, ... etc. The instruments were of many different kinds and their characteristics and positions are fully described in the report titled "FEBEX Full-scale Engineered Barriers Experiment in Crystalline Host Rock. FINAL DESIGN AND INSTALLATION OF THE IN-SITU TEST AT GRIMSEL" (Fuentes-Cantillana & García-Siñeriz 1998b).

A Data Acquisition and Control System (DACS) located in the service area of the FEBEX drift collected the data provided by the instruments. This system recorded and stored information from the sensors and also controlled the power applied to the electrical heaters, in order to maintain a constant temperature at the heaters/bentonite interface. The DACS allowed the experiment to be run in an automated mode, with remote supervision from Madrid. Data stored at the local DACS were periodically downloaded in Madrid and used to build the experimental Master Data Base.

The construction of the concrete plug was completed in October 1996, and the heating operation started on 28.02.1997. A constant temperature of 100 °C was maintained at the heaters/bentonite interface, while the bentonite buffer slowly hydrated with water naturally flowing from the rock. A complete report that includes both the installation of the test and the results gathered after two years of operation is given in "FEBEX full-scale engineered barriers experiment for a deep geological repository for high level radioactive waste in crystalline host rock FINAL REPORT" (Fuentes-Cantillana et al. 2000).

1.3   Dismantling of Heater #1 and test configuration afterwards (FEBEX II)

A partial dismantling of the FEBEX "in-situ" test was carried out during the summer of 2002, after 5 years of continuous heating ("first dismantling"). The operation included the demolition of the concrete plug, the removal of the section of the test corresponding to the first heater, and the sealing with a new shotcrete plug. A large number of samples from all types of materials were taken for analysis. A number of instruments were subsequently dismantled, as well as a few new ones installed. Accordingly, system design was adapted, and the physical layout was changed in order to ease the first dismantling operation.

The buffer and all components were removed up to a distance of 2 meters from Heater #2 to minimize disturbance of the non-dismantled area. A dummy steel cylinder with a length of 1 m was inserted in the void left by Heater #1 in the centre of the buffer. Some new sensors were installed in that one additional meter of bentonite buffer.

Additional sensors were introduced in boreholes drilled in the buffer parallel to the drift. To simplify this operation, the new concrete plug was constructed in two phases: an initial temporary plug measuring just 1 m in length was built immediately after dismantling, and a second section to complete the plug length to the 3 m as planned in the design of the experiment. Unlike FEBEX I, the new plug was a parallel plug, without a recess excavated in the rock, constructed by shotcreting.

The description of the first dismantling operation is given by the report titled "Dismantling of the Heater #1 at the FEBEX "in situ" test. Description of operations" (Bárcena et al. 2003). The configuration of the test, after completing the first dismantling operation and construction of the full plug length, is shown in Fig. 1-3.
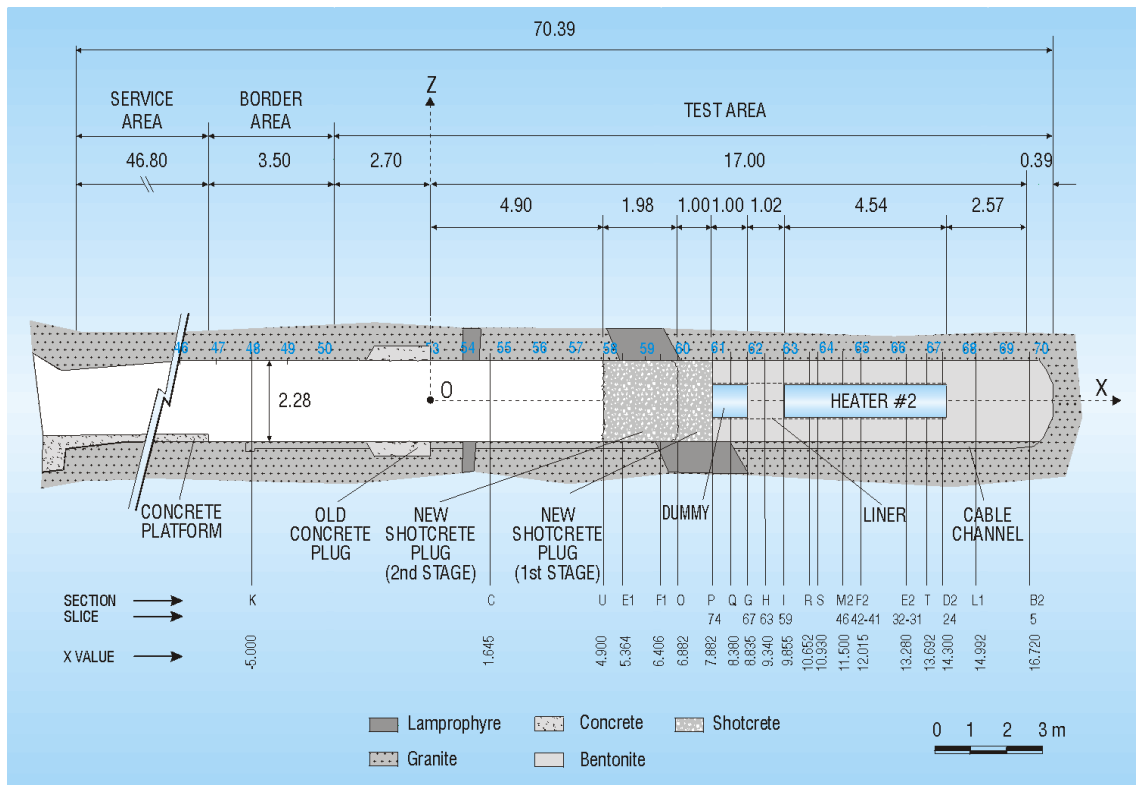
Fig. 1-3:   Status of the FEBEX "In-situ" test after the first dismantling (FEBEX II configuration).

A more complete report that describes the test from the conception up to two years of operation after the first dismantling is given in the document titled "FEBEX Full-scale Engineered Barriers Experiment. UPDATED FINAL REPORT 1994 – 2004" (Huertas et al. 2006).

1.4   Concept of dismantling Heater #2

The objective of the second dismantling operation, carried out throughout 2015, was to dismantle all the remaining parts of the "in-situ" test, including the Heater #2. This operation includes carrying out a complete sampling of the bentonite, rock, relevant interfaces, sensors, metallic components and tracers to allow analysing the barriers' condition after 18 years of heating and natural hydration.

Analytical results will be compared with data obtained from the first dismantling (Huertas et al. 2006); the monitoring data (Martinez et al. 2014) as well as with the results derived from modelling efforts (Lanyon & Gaus 2013). The results are expected to increase the current knowledge and confidence for the FEBEX-DP partners in bentonite performance with a focus on thermo-hydro-mechanical (THM) and thermo-hydro-chemical (THC) processes as well as on corrosion and microbial activity. The reporting of the laboratory analysis and dismantling results is expected to be complete by the end of 2017 with a final integrated report issued in 2018.

All details about the planned dismantling operation and sampling program are given in the reference documents: "FEBEX-DP (GTS) Full Dismantling Test Plan" (Bárcena & García-

Siñeriz 2015a), "FEBEX-DP (GTS) Full Dismantling Sampling Plan" (Bárcena & García-Siñeriz 2015b) and its update (Rey et al. 2015).

All sample logs of the dismantling operation are documented in AN 15-578 Sample Log Book 34 to 62 FEBEX-DP (Abós & Martínez 2015).

1.5   Objectives and contents

Thermo-hydraulic-mechanical modelling of the FEBEX In-Situ Test can be considered under the following headings:

- modelling during test design (Enresa 1996)

- pre-operational modelling carried out before the start of the test (Enresa 1998)

- concurrent modelling to aid interpretation during the performance of the test (Enresa 2006a, 2006b, Gens et al. 2009)

- modelling within the DECOVALEX III programme (Alonso et al. 2005; Tsang et al. 2005)

- additional modelling within FEBEXe (Dupray et al. 2013b; Olivella et al. 2012)

- post-mortem modelling after the first dismantling of FEBEX (Sánchez et al. 2012b; Olivella et al. 2012; Dupray 2013)

This report is intended for documenting the activities carried out and the main results gathered from the pre-dismantling modelling of the FEBEX-DP in situ test. Three modelling teams were tasked with pre-dismantling modelling, namely CIMNE (International Center for Numerical Methods in Engineering, Spain), EPFL (Laboratory for Soil Mechanics at the Swiss Federal Institute of Technology in Lausanne, Switzerland), and Clay Technology AB (Sweden). The teams were free to choose the modelling approach and tools used for their analyses. The objective is to improve understanding of the processes determining the THM evolution in the FEBEX "in-situ" test, evaluate the current predictive capabilities, and identify potential enhancements to modelling tools. Therefore, it is not the purpose of this report to compare the goodness of predictions between the different teams. Each team provides an in-depth evaluation of the approaches followed and the performed analyses, and discusses in detail the following aspects:

- the modelling approach followed for the THM simulations

- the presentation and evaluation of model predictions through direct comparison to sensor data as well as post-mortem measurements after the first dismantling (Heater #1)

- the interpretation of the model results

- the evaluation of the driving processes in the in-situ test

- the modelled density and water content distributions predicted at two cross-sections ("hot" and "cold", respective around Heater #2 and between the heaters) for future comparison to post-mortem measurements after the second dismantling (Heater #2)

- an evaluation of the progress made in this exercise and the remaining uncertainties

- an evaluation of the consequences for the early repository evolution, from the perspective of each team's approach

This report does not aim to provide an uncertainty or sensitivity analysis of the experiment. However, some of the key elements of the modelling analyses are affected by the conceptual uncertainties related to the representation of the experimental system in the numerical models. Conceptual uncertainty related to the conceptualization of the problem is discussed in a qualitative fashion by each team based on their model approach. Accordingly, the choice of constitutive models is done separately by each team. Values of input parameters used for modelling are based on experimental data that are cited throughout this report. The data sources were selected by the modelling teams depending on their modelling approach and assumptions, and may therefore differ. Parametric uncertainty related to the spatial (and temporal) variation of the input parameters used to conceptualize the different materials is not taken into account. Additional uncertainty that stems from numerical errors is beyond the scope of this study and is evaluated separately in the code documentation provided by each team. Modelling results are thus presented deterministically for the best estimate model. In some cases, deterministic variants are used to qualitatively assess parameter sensitivity and the impact of the associated parameter uncertainty on the predictions. Potential measurement errors in input parameters as well as in-situ observations is discussed separately in the series of sensor data, dismantling, and on-site analyses reports (García-Siñeriz et al. 2016; Villar et al. 2016; Martínez et al. 2016; Rey et al. 2016).

In this report, the modelling analyses are detailed in one chapter per modelling team. Chapters 2, 3, and 4 provide the detailed description of the modelling approaches followed by CIMNE, EPFL, and Clay Technology (hereafter Clay Tech), respectively. Chapter 5 presents the integration of the three modelling approaches and a joint interpretation of the modelling results. A synthesis of the modelling codes, model formulations, modelling strategies and approaches followed by the three teams is given. Moreover, a detailed discussion is carried out on the evaluation and interpretation of the results, interpreting the differences and similarities from the three approaches. Chapter 6 provides a comparison of model results from the three teams to post-mortem measurements after the second dismantling (Heater #2). The comparison provides additional feedback in the THM evaluation achieved with the model predictions. Chapter 7 provides a synthesis and the conclusions of this modelling study. The discussion highlights the lessons learned and the "missing pieces" identified through the analyses.

2   THM modelling by CIMNE

This chapter describes the modelling analyses performed by CIMNE. Section 2.1 provides the model description including the balance equations, constitutive laws, and underlying assumptions. Section 2.2 gives a short overview of the development history of the FEBEX model. Section 2.3 provides the initial and boundary conditions as well as input parameters used in the simulations. Section 2.4 discusses the model outcomes in the following steps:

- analysis until the switch-off and excavation of Heater #1

- analysis just after the switch-off and excavation of Heater #1

- simulation of the first dismantling involving Heater #1

- THM behaviour during cooling down and dismantling of Heater #1

- analysis of post-mortem tests related to the clay barrier involving Heater #1

- simulation of the second dismantling involving Heater #2

- analysis until the switch-off and excavation of Heater #2

The analysis from CIMNE concludes with an interpretation of the results in Section 2.5.

2.1   Description of the model and underlying assumptions

The theoretical framework adopted to analyse the problem is the coupled THM formulation proposed by Olivella et al. (1994). The framework is formulated using a multi-phase, multi-species approach: solid, liquid and gas are the phases whereas mineral, water and air are the species. The liquid phase may contain water and dissolved air, and the gas phase may be a mixture of dry air and water vapour. Dry air is considered as a single species.

The approach is composed of three main parts: i) balance equations, ii) constitutive equations and iii) equilibrium restrictions. The main balance equations considered in the formulation are: mass balance of species (i.e. water, air and solid), balance of internal energy, and momentum balance. One main (state) variable is associated with each balance equation. For example, liquid pressure (P_l) is associated with water mass balance; temperature (T) with internal energy balance; and displacements (**u**) with momentum mass balance. The constitutive equations establish the link between these main (state) variables and the dependent variables, including the degree of saturation (S_l), stresses (σ), and heat flux ($\mathbf{i}_c$). A short description of the mathematical formulation and main constitutive models is presented in the following.

2.1.1   Balance equations

Mass balance equations were established following the compositional approach, which consists of balancing the species rather than the phases.

Water is present in liquid and gas phases. The total mass balance of water is expressed as (Olivella et al. 1994):

$$\frac{\partial}{\partial t}\left(\theta_l^w S_l n + \theta_g^w S_g n\right) + \nabla \cdot \left(\mathbf{j}_l^w + \mathbf{j}_g^w\right) = f^w \tag{2-1}$$

The main variable associated with this equation is the liquid pressure (P_l). A similar equation can be written for the mass balance of air (Olivella et al. 1994), however this equation has not been used in these analyses as a constant gas pressure has been assumed (Gens et al. 2009). Thermal equilibrium between phases has been assumed; consequently, only one equation is required to establish energy balance. The total internal energy per unit volume of porous media is obtained adding the internal energy of each phase corresponding to each medium. Applying the balance equation to this quantity, the following equation is obtained:

$$\frac{\partial}{\partial t}\left(E_s\rho_s\left(1-n\right)+E_l\rho_lS_ln+E_g\rho_gS_gn\right)+\nabla.\left(\mathbf{i}_c+\mathbf{j}_{Es}+\mathbf{j}_{El}+\mathbf{j}_{Eg}\right)=f^E \tag{2-2}$$

The temperature (T) is the main variable associated with this equation. The balance of momentum for the porous medium reduces to the equilibrium equation in total stresses:

$$\nabla.\boldsymbol{\sigma}+\mathbf{b}=0 \tag{2-3}$$

Through an adequate constitutive model (presented in the next section), the equilibrium equation is transformed into a form expressed in terms of solid velocities and fluid pressures. The assumption of small strain rate is also made. The displacement field (**u**) is the main variable associated with this equation. In addition, the mass balance of the solid is established for the whole porous medium and it is used to update the porosity (Olivella et al. 1996).

2.1.2   Constitutive equations and equilibrium restrictions

Laboratory tests carried out in the context of the FEBEX project have been used to determine independently the different parameters of the constitutive models used in the numerical simulation of the in-situ test. The main constitutive laws and the corresponding adopted parameters are presented in the following sections.

Mechanical constitutive model

The Barcelona Basic Model (*BBM*) has been adopted to model the mechanical behaviour of the clay barrier (Alonso et al. 1990). The model is formulated in terms of the three stress invariants (p; J; θ); suction and temperature. The descriptions of the stress invariants are provided in Section 2.1.4. The trace of the yield function on the isotropic *p-s* plane is called the *LC* (Loading-Collapse) yield curve, because it represents the locus of activation of irreversible deformations due to loading increments or wetting (collapse compression). The position of the *LC* curve is given by the value of the hardening variable $p_o{}^*$. The *BBM* yield surface (*F*) is then expressed as:

$$F=3J^2-\left[\frac{g(\theta)}{g(-30°)}\right]^2M^2\left(p+p_s\right)\left(p_0-p\right)=0 \tag{2-4}$$

When yielding takes place the increment of plastic deformations is evaluated through:

$$\dot{\boldsymbol{\varepsilon}}^p = \lambda \frac{\partial G}{\partial \boldsymbol{\sigma}}$$

(2-5)

where G is the plastic potential as follows:

$$G = \alpha_G 3J^2 - \left[\frac{g(\theta)}{g(-30°)} \right]^2 M^2 (p + p_s)(p_0 - p) = 0$$

(2-6)

where α_G is the material parameter that controls the degree of non-associative, determined according to (Alonso et al. 1990).

The hardening law is expressed as a rate relation between the volumetric plastic strain and the saturated isotropic pre-consolidation stress "p^*_0", according to:

$$\frac{\dot{p}^*_0}{p^*_0} = \frac{(1+e)}{(\lambda_{(0)} - \kappa)} \dot{\varepsilon}^p_v$$

(2-7)

The dependence of the tensile strength on suction and temperature is given by (Gens 1995):

$$p_s = ks \ e^{-\rho \Delta T}$$

(2-8)

The dependence of p_0 on suction is given by:

$$p_0 = p_c \left(\frac{p^*_{0T}}{p_c} \right)^{\frac{\lambda_{(0)} - \kappa}{\lambda_{(s)} - \kappa}} \text{(a)}; \quad p^*_{0T} = p^*_0 + 2\left(\alpha_1 \Delta T + \alpha_3 \Delta T |\Delta T| \right) \text{(b)}$$

(2-9)

The compressibility parameter for changes in net mean stress for virgin states of the soil ($\lambda_{(s)}$) depends on suction according to:

$$\lambda_{(s)} = \lambda_{(0)} \left[r + (1-r)\exp(-\zeta s) \right]$$

(2-10)

The bulk modulus (K) for changes in mean stress is evaluated with the following law:

$$K = \frac{(1+e)}{\kappa} p \tag{2-11}$$

The bulk modulus for changes in suction is computed according to the following law:

$$K_s = \frac{(1+e)(s + p_{atm})}{\kappa_s} \tag{2-12}$$

The bulk modulus for changes in temperature is computed by the following law:

$$K_T = \frac{1}{(\alpha_0 + \alpha_2 \Delta T)} \tag{2-13}$$

where α_o and α_2 are parameters related to the elastic thermal strain.

Due to the high compaction the bentonite blocks have been subjected to, the description of the behaviour of the material inside the yield surface is particularly important. The variation of stress-stiffness with suction and the variation of swelling potential with stress and suction have been considered. The resulting elastic model is the following:

$$\dot{\varepsilon}_v^e = \frac{\kappa}{(1+e)} \frac{\dot{p}}{p} + \frac{\kappa_s}{(1+e)} \frac{\dot{s}}{(s+0.1)} + (\alpha_0 + \alpha_2 \Delta T)\dot{T} \text{ a); } \dot{\varepsilon}_s^e = \frac{\dot{J}}{G_t} \text{ b)} \tag{2-14}$$

where (CODE_BRIGHT Manual 2015):

$$\kappa = \kappa_i (1+\alpha_s s) \text{ a); } \kappa_s = \kappa_{s0}\left(1+\alpha_{sp} \ln p / p_{ref}\right) \text{b); } G_t = \frac{3(1-2\mu)K}{2(1+\mu)} \text{ c)} \tag{2-15}$$

The model parameters were determined from the experimental laboratory campaign carried out during the FEBEX project (Gens et al. 2009). As an example, Fig. 4a shows the computed results of two swelling pressure tests according to Lloret et al. (2003).

The thermomechanical behaviour of the rock and concrete has been described using a linear elastic model in term of a bulk modulus (K) and shear modulus (G_t); and a coefficient of linear expansion α_0.

Constitutive models related to the hydraulic behaviour

The models introduced below have been adopted to describe the behaviour of the porous materials (i.e. clay barrier, granite and concrete). Advective fluxes are computed using generalized Darcy's law, expressed as:

$$\mathbf{q}_\alpha = -\mathbf{K}_\alpha \left(\nabla P_\alpha - \rho_\alpha \mathbf{g} \right); \ \alpha = l, g \tag{2-16}$$

The permeability tensor is evaluated according to:

$$\mathbf{K}_\alpha = \mathbf{k} \frac{k_{r\alpha}}{\mu_\alpha}; \qquad \alpha = l, g \tag{2-17}$$

The dependence of intrinsic permeability on porosity has been based on Kozeny's law:

$$\mathbf{k} = k_0 \frac{n^3}{(1-n)^2} \frac{(1-n_0)^2}{n_0^3} \mathbf{I} \tag{2-18}$$

Permeability tests performed on saturated samples have been used to adopt the reference values: $k_0 = 1.9 \times 10^{-21}$ m^2 for a porosity of 0.40 (Fig. 2-4b). The well-known power law has been adopted to describe the dependence of liquid permeability on the degree of saturation:

$$k_{rl} = S_l^{\ n_s} \tag{2-19}$$

A value of $n_s = 3$ has been determined from back-calculating hydration tests on FEBEX bentonite. The water retention curve relates the degree of saturation of the material with suction. The law adopted is based on the van Genuchten model (van Genuchten, 1978), as follows:

$$S_l = \left[1 + \left(\frac{s}{P_o} \right)^{\frac{1}{1-\lambda_o}} \right]^{-\lambda_o} f_d \ \text{a)}; \ f_d = \left(1 - \frac{s}{P_d} \right)^{\lambda_d} \ \text{b)} \tag{2-20}$$

Fig. 4.c presents the results of tests carried out at conditions of constant volume on FEBEX bentonite, together with the adopted relationship. Model parameters are: $P_0 = 20$ MPa; $\lambda_0 = 0.18$, $P_d = 1100$ MPa, and $\lambda_d = 1.10$.

Non-advective fluxes of species inside the fluid phases are computed through Fick's law, which expresses them in terms of gradients of mass fraction of species through a hydrodynamic dispersion tensor that includes both molecular diffusion and mechanical dispersion:

$$\mathbf{i}_\alpha^i = -\mathbf{D}_\alpha^i \nabla \omega_\alpha^i \ \ i = w, a \ ; \qquad \alpha = l, g \tag{2-21}$$

In particular, for the vapour transfer the following model is used:

$$\mathbf{i}_g^w = - \left(\phi \rho_g S_g \tau D_m^w \mathbf{I} + \rho_g \mathbf{D}_g^{'} \right) \nabla \omega_g^w; \quad D_m^w \left(m^2 / s \right) = 5.9 \times 10^{-12} \frac{\left(273.15 + T \right)^{2.3}}{P_g} \tag{2-22}$$

Where $\tau = 0.8$; more details can be find elsewhere (e.g. Olivella et al. 1994; CODE_BRIGHT User's Manual 2015).

Constitutive models related to the thermal behaviour

Fourier's law has been adopted to describe the conductive flux of heat. The thermal conductivity (λ) depends on the saturation of the clay and is expressed by the geometric mean of the thermal conductivities of the components:

$$\mathbf{i}_c = -\lambda \nabla T \ \text{a) ;} \ \lambda = \lambda_{sat}^{S_l} \lambda_{dry}^{(1-S_l)} \ \text{b} \tag{2-23}$$

Based on experimental results (Fig. 2-2), the following thermal conductivities have been adopted: $\lambda_{dry} = 0.47$ [W/mC°] and $\lambda_{sat} = 1.15$ [W/mC°].

2.1.3   Equilibrium restrictions

It is assumed that phase changes are rapid in relation to the characteristic times typical of the problem under consideration. So, they can be considered in local equilibrium, giving rise to a set of equilibrium restrictions that must be satisfied at all times. The vapour concentration in the gaseous phase is governed by the psychometric law and the amount of air dissolved in water is given by Henry's law (Olivella et al. 1994, 1996).

2.1.4   Stress invariants

The stress invariants are defined as follows:

$$p = \left(\frac{1}{3}\right)\left(\sigma_x + \sigma_y + \sigma_z\right) \tag{2-14}$$

$$J^2 = \frac{1}{2} \operatorname{trace}\left(\mathbf{s}^2\right) \tag{2-25}$$

$$\theta = -\frac{1}{3} sin^{-1}\left(1.5\sqrt{3} \ det \ \mathbf{s}/J^3\right) \tag{2-26}$$

with:

$$s = \boldsymbol{\sigma} - p\,\boldsymbol{I} \qquad\qquad (2\text{-}27)$$

where **I** is the identity tensor.

2.2 History of the development of the FEBEX model

The numerical analysis is carried out with the "Operational Base Case" model, which will be referred to in the following as "OBC'. The OBC model was established prior to the start of the heating experiments to incorporate all available information obtained from laboratory tests of FEBEX bentonite at the beginning of the operational phase. Due to uncertainty in the initial power-up schedule and integration of laboratory tests, model analysis and test overlapped for a few months, but no adjustments were made to the model. The model analyses are compared with observations over a period of approximately eighteen years. Therefore, the analysis results reported herein can be reasonably considered as blind predictions.

Previous to the OBC, a number of numerical simulations were performed considering different hypotheses and conditions (including sensitivity analyses using 1-D and 2-D models). The aim of these modelling exercises was to gain a better understanding of the coupled behaviour associated with nuclear waste disposal under real conditions in crystalline rock. Details about these analyses can be found elsewhere (e.g. Gens et al. 1998; Huertas et al. 2000).

2.3 Description of the initial and boundary conditions, input parameters

The model results presented in this section include two main phases of the experiment: a) an initial isothermal hydration of the barrier taking place in the 135 day-period between the sealing of the drift and the start of heating and b) simultaneous (natural) hydration and heating of the test with the two heaters switched on lasting 1'827 days.

Fig. 2-1 shows the 2-D axisymmetric longitudinal section adopted for the modelling of the in-situ test. A number of analyses were performed to study the sensitivity of the model results with respect to: a) the adopted mesh (i.e. element size, discretization, element shape), and b) the distance to boundaries. Based on those analyses, a mesh composed of 2'387 quadrilateral bilinear elements with 4 integration points was adopted in this study. Selective integration according to Hughes (1980) has been adopted. The outer boundary of the model is placed at a distance of 50 m from the tunnel axis. The geometry also takes into account the presence of the access drift and the concrete plug.
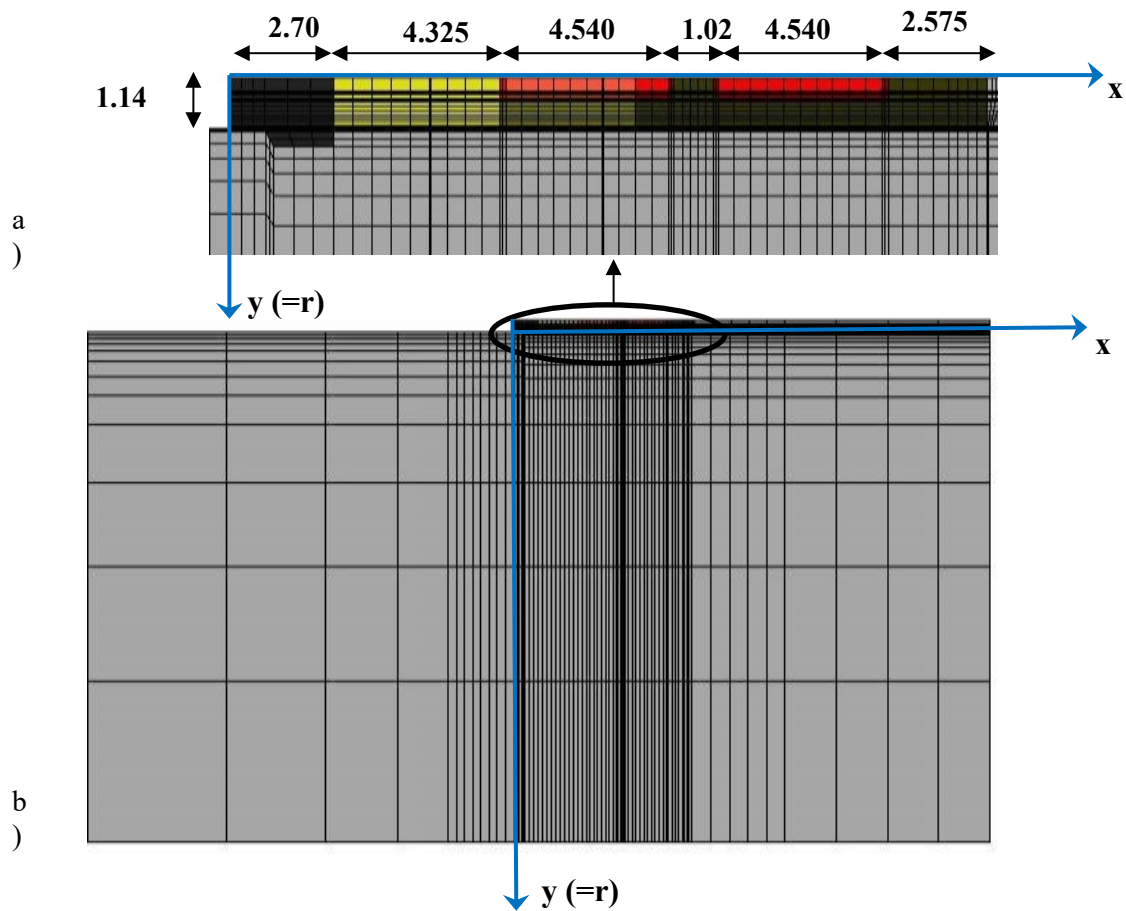
Fig. 2-1:   2-D axisymmetric mesh of the in-situ test.

Axis "x" is coincident with the tunnel axis, and axis "y" is in the direction of the tunnel radius ("r"). a) Detailed view of the mesh, showing the different materials to be excavated and the ones that will remain in the mesh. b) Entire mesh used for the THM modelling.

Fig. 2-2 shows a comparison between the constitutive relationships used in the analysis (lines) and the related experimental results obtained for the FEBEX bentonite (symbols), respectively. Fig. 2-2a shows results related to the mechanical model. The experimental data were obtained from swelling pressure tests (Lloret et al. 2003), whereas the model results correspond to Eqs. 2-4 to 2-15 (see Section 2-1 and Tab. 2-1). Fig. 2-2b shows the estimated relationship between intrinsic permeability and porosity. The experiments were performed with samples under constant saturation (Villar 2002), whereas a modified Kozeny's relationship (Eq. 2-18) has been used in the model. Results from water retention tests performed under constant volume conditions (Villar 2002) are shown in Fig. 2-2c); along with the van Genuchten relationship (van Genuchten 1978) used in the model (Eq. 2-19). Fig. 2-2d shows the relationship between thermal conductivity and saturation, together with the corresponding model adopted in the analysis (Eq. 2-23).

The coupled formulation was implemented in the finite element program CODE_BRIGHT (Olivella et at. 1996). All equations (i.e. mass balance, momentum balance, constitutive and equilibrium restrictions) are solved in a fully coupled way. The Newton-Raphson method is used to solve the non-linear problem and finite differences are adopted to solve the evolution in time. The code has been extensively validated in different simulations involving coupled geomechanical problems (e.g., Olivella et al. 1996; Alonso & Alcoverro 2005; Sánchez et al. 2008, 2012a; Gens 2009).
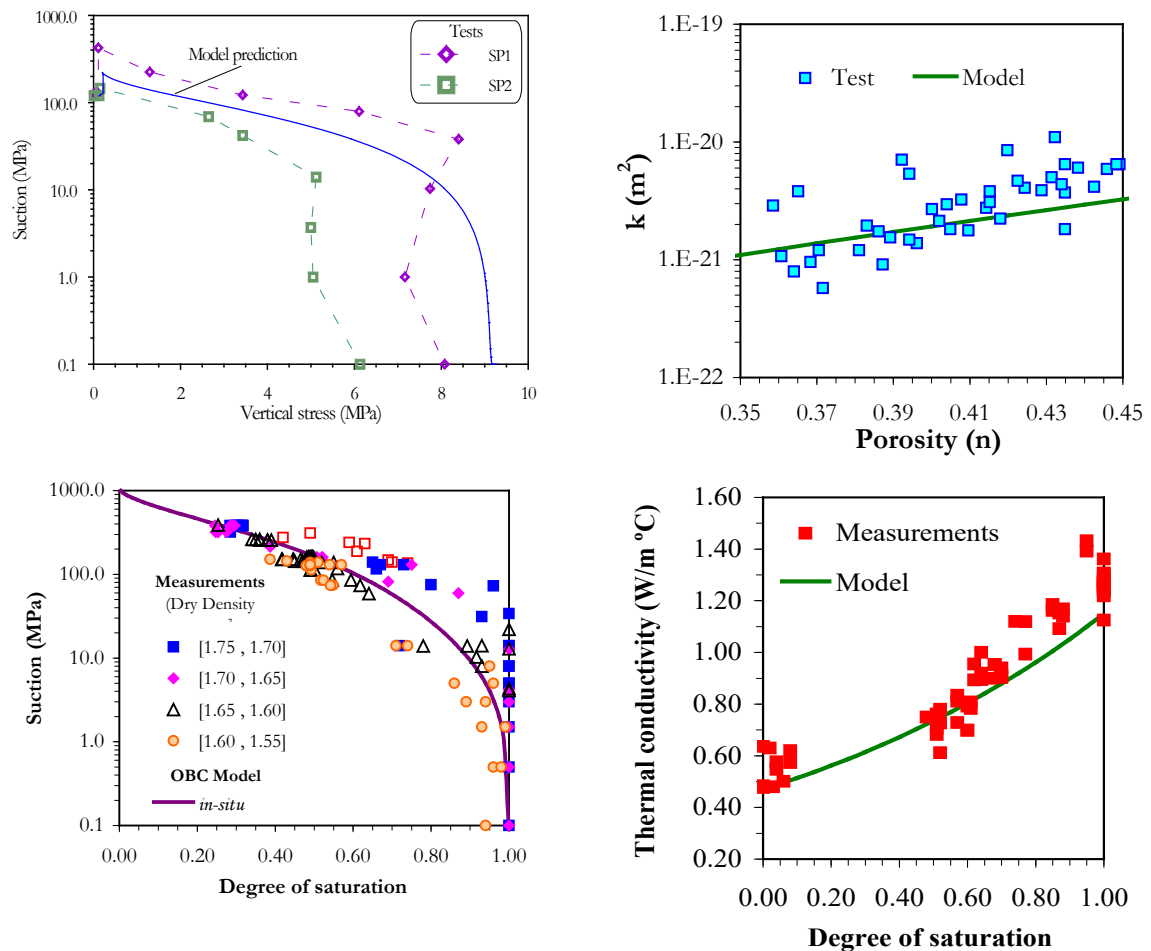
Fig. 2-2:   Main constitutive laws.

a) Mechanical: computed stress path for swelling pressure tests using the BBM. Experimental results (SP1 and SP2 paths) are provided for comparison. b) Hydraulic: estimated relationship between saturated permeability and porosity. Experimental data and adopted model for the intrinsic permeability law. c) Hydraulic: retention curve adopted in the analyses, together with the experimental data for FEBEX bentonite. d) Thermal: Thermal conductivity: FEBEX bentonite experimental results and model fit.

The analyses performed include simulation of the tunnel excavation, allowing, subsequently, sufficient time for both hydraulic and mechanical equilibration. Based on measurements in the gallery zone (Huertas et al. 2006), an initially uniform and isotropic stress field ($\sigma_r = \sigma_\theta = \sigma_z = 28$ MPa) before excavation has been assumed in the host rock. Initial granite porosity is assumed to be equal to 0.01 (Huertas et al. 2006). In accordance with the measurements made during installation, an initial water content of 14 % has been assumed for the clay barrier. This water content corresponds to a global degree of saturation of 0.55. Considering this degree of saturation and the retention curve of the bentonite (Fig. 2-2c), it can be anticipated that the initial suction is approximately 135 MPa. Based on the available installation data, an average dry density of 1.60 Mg/m^3 has been adopted for the analysis. Initial stress in the buffer is assumed isotropic and equal to 0.2 MPa, corresponding to the self-weight at the centre of the clay barrier. An initial uniform temperature of 12 °C was assumed for the entire model domain. It has been assumed that there is full contact between the steel liner and bentonite, and between bentonite and the rock (i.e. there is no gap and no relative displacement between adjacent materials).

The hydraulic boundary conditions are based on information obtained during the hydrogeological characterization (Huertas et al. 2006). In accordance to the observations made, the water flow close to the tunnel is mainly radial, converging gradually towards the regional flow direction over a distance of 50 m. Therefore, it is assumed that the water pressure varies along the boundary according to the water pressure measurements made in borehole sections far away from the test. The experiment is not considered airtight and, in consequence, a constant value of gas pressure is assumed.

The design conditions of the experiment contemplate a maximum temperature of 100 °C at the contact between the heater and bentonite. The heating schedule used to reach the target temperature reported in Huertas et al. (2006) was adopted in this simulation (Gens et al. 2009). The prescribed temperature at r = 50 m is 12 °C, and the boundary radial stress is 28 MPa.

The main model parameters associated with the constitutive models of the different components of the barrier system are presented in Tab. 2-1. Within the test zone, the granite is crossed by a lamprophyre dyke. As would be expected, there are significant variations of permeability in different zones of the rock, depending on the degree of fracturing and on the presence of contact with the lamprophyre dykes. However, it has been shown that these local variations did not affect the performance of the test, because the low permeability of the bentonite controlling the rate of water inflow. Effectively, all parts of the granite supplied sufficient amounts of water along the entire test area (Gens et al. 2009). The lamprophyre has not been explicitly accounted for in the model, and the values given in Tab. 2-1 correspond to averaged properties for the test section. In the absence of any evidence of desaturation of the rock, the granite is assumed saturated throughout the simulation.

Tab. 2-1:   Hydromechanical parameters used in the numerical simulations.

Constitutive Model	Parameters*		
	Bentonite	**Granite**	**Concrete**
Fourier's law Equation A.23	$\lambda_{sat} = 1.15$; $\lambda_{dry} = 0.47$ [W/mC°]	$\lambda_{sat} = 3.30$; $\lambda_{dry} = 3.20$ [W/mC°]	$\lambda_{sat} = 1.40$; $\lambda_{dry} = 1.10$ [W/mC°]
Intrinsic permeability Equation A.18	$k_0 = 1.9\ e^{-21}$ [m²]; $n_0 = 0.40$	$k_0 = 8.18\ e^{-21}$ [m²]; $n_0 = 0.01$	$k_0 = 1.0\ e^{-22}$ [m²]; $n_0 = 0.05$
Relative permeability Equation A.19	$n = 3$	$n = 1$	$n = 1$
Fick's law Equation A.22	$\tau = 0.80$	$\tau = 1.00$	$\tau = 1.00$
Retention curve Equation A.20	$P_0 = 7.00$ [MPa]; $\lambda = 0.10$ $P_d = 1'100$ [MPa]; $\lambda_d = 2.10$	$P_0 = 2.10$ [MPa]; $\lambda = 0.70$ $P_d = 1'100$ [MPa]; $\lambda_d = 0.00$	$P_0 = 2.10$ [MPa]; $\lambda = 0.70$ $P_d = 1'100$ [MPa]; $\lambda_d = 0.00$
Mechanical model	Equations A.4 to A.15 $\kappa_0 = 0.04$; $\kappa_{s0} = 0.25$; $\mu = 0.40$ $\alpha_{sp} = -0.161$; $\alpha_s = -0.003$ [MPa] $\lambda_{(o)} = 0.14$; $P_o^* = 14$[MPa]; $M = 1.0$ $r = 0.925$; $p_c = 0.50$ [MPa]; $\zeta = 0.1$ $k = 0.10$; $\alpha = 0.5$; $\alpha_0 = 1.5 \times 10^{-4}$ [1/C]; $\rho = 0.2$ [1/C]	Linear elastic model $K = 3.92 \times 10^4$ [MPa] $G_t = 1.35 \times 10^4$ [MPa] $\alpha_0 = 7.8 \times 10^{-6}$ [1/C]	Linear elastic model $K = 2.51 \times 10^4$ [MPa] $G = 1.25 \times 104$ [MPa] $\alpha_0 = 6.9 \times 10^{-6}$ [1/C]

*   The parameters not indicated in this table are set equal to zero.

2.4   Model outcomes (impact of heater switch-off, sensitivity analysis)

Selected results of the OBC analysis are presented and compared with observations. All observations extend to the five-year duration of the heating stage (1'827 days). The analysis refers to the sections presented in Fig. 2-3. Selected results are presented here, whereas a more detailed analysis can be found in Gens et al. (2009) and Sánchez et al. (2012).
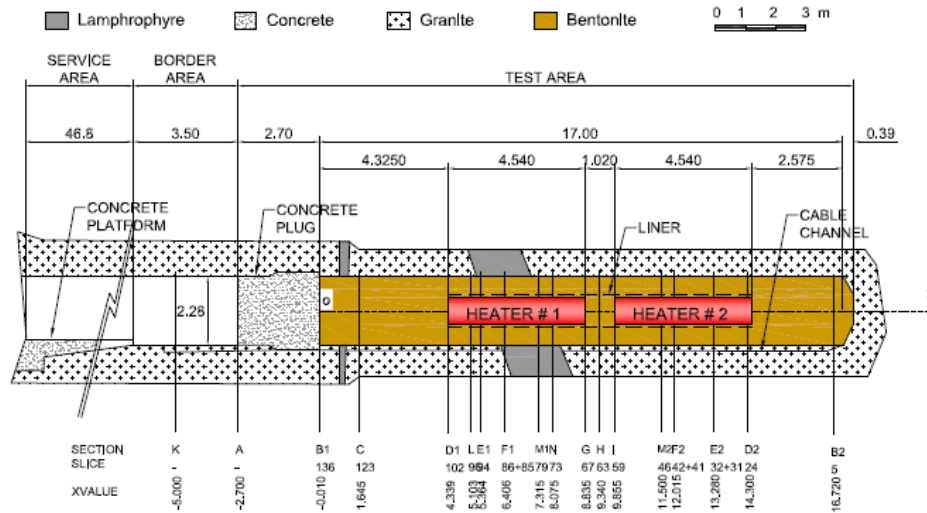
Fig. 2-3:   Scheme of the in-situ test and instrumented barrier sections.

Analysis until the switch-off and excavation of Heater #1

Fig. 2-4a shows that the power supplied by the heaters is slightly lower in the simulation at later times (difference of about 10 % in Heater #1). In spite of this, the model captures well the overall thermal trend of the test. As an example, the comparisons corresponding to Section D2 are presented in Fig. 2-4b). Detailed analysis on the temperature evolution will be provided in the next section.

The presence of heterogeneities in the natural system may make it more difficult to predict the hydration of the clay barrier correctly. Nevertheless, the response of the model is globally satisfactory. As an example, results from "Section E1' are presented in Fig. 2-4c. In the zone near the rock there is a monotonic increase of relative humidity, reflecting the process of hydration induced by the host rock water. The behaviour close to the tunnel axis is characterized by an initial increase of the relative humidity (induced by the passing of a vapour front driven by heating), followed by drying, and then by a slow increase of relative humidity due to the progress of the general hydration. In general terms, and considering also other sections of the barrier, the correspondence between computations and measurements are reasonably well, although at some locations near the heaters the observed drying is somewhat stronger than computed.

As expected, a significant increase of stresses has been observed during hydration. This is due to the confined conditions of the clay barrier and the high swelling of the heavily compacted bentonite (Fig. 2-4d). The measurement of total stresses in the in-situ test and comparison to predictions is challenging due to the conceptual uncertainty in the description of the system (e.g. contacts between materials and representation thereof). In the early phase, the model results can be considered as an upper bound of the measurements, which can be attributed to the effect of the early-phase contacts between the bentonite blocks in the experiment.
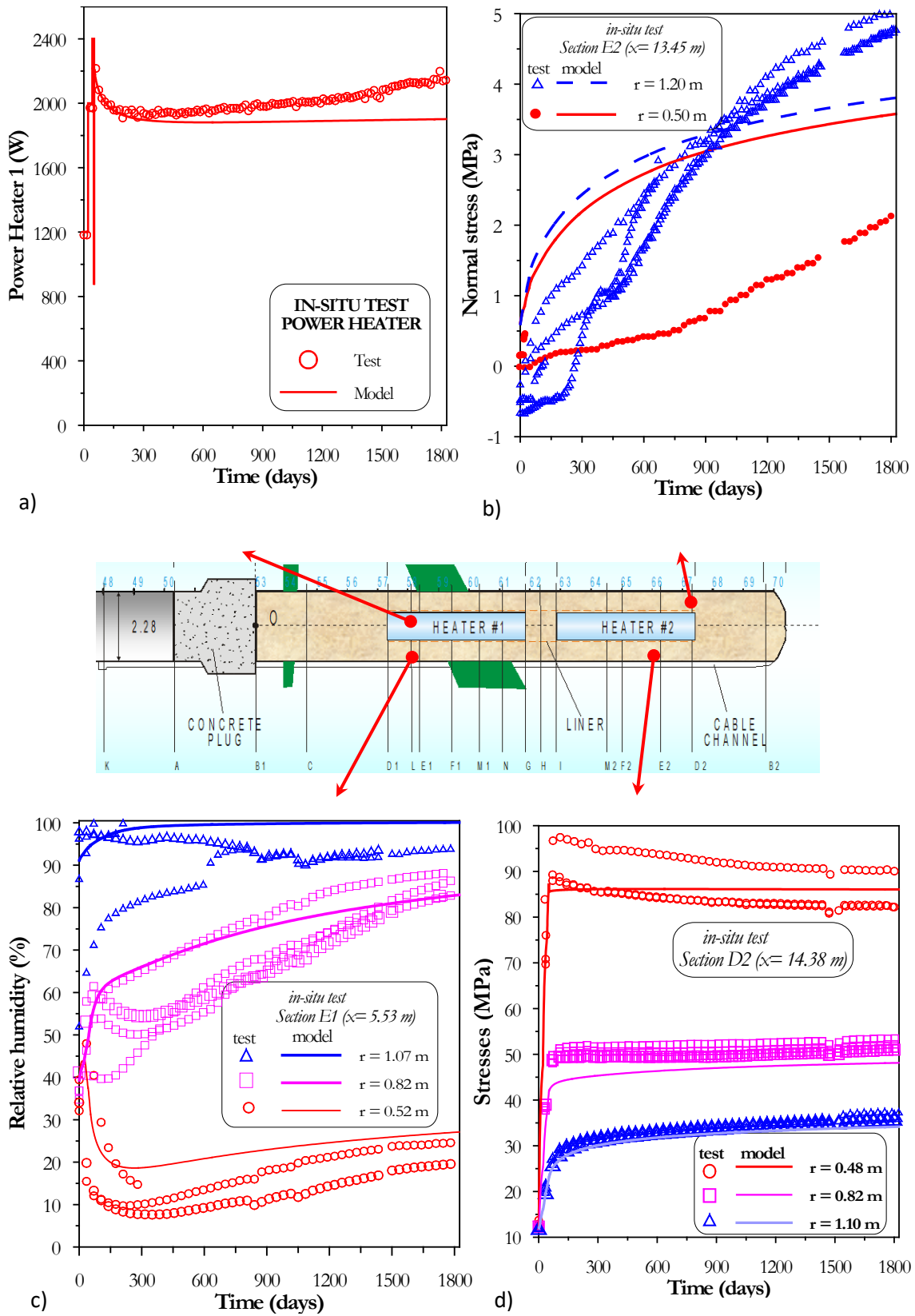
Fig. 2-4:   Evolution of main variables in the clay barrier; observed versus computed values
             (OBC model) a) heat power; b) temperature; c) relative humidity; and d) stresses.

Analysis just after the switch-off and excavation of Heater #1

Based on a number of preliminary numerical analyses, it was decided to switch-off Heater #1 in one step. It was predicted that after about one month of Heater #1 disconnection, the temperature in the sections of the barrier that were to be retrieved, would have decreased adequately to conduct the dismantling operations.

Fig. 2-5 shows experimental and modelling results of the evolution of the temperature at the heater/bentonite interface where the temperature was fixed at 100 °C prior to switch-off. The figure also shows the power emitted by Heater #1, indicating the somewhat lower values predicted by the model (approximately 10 % difference from actual heater output, see previous section). Up to day 1827 (28.02.2002), the heating power was adjusted automatically to maintain a constant temperature of 100 °C at the interface between heater and bentonite. From this date on, Heater #1 was switched off and this zone of the barrier cooled down as recorded by the sensor. The model provided a good prediction of the temperature decay at the thermal control point.
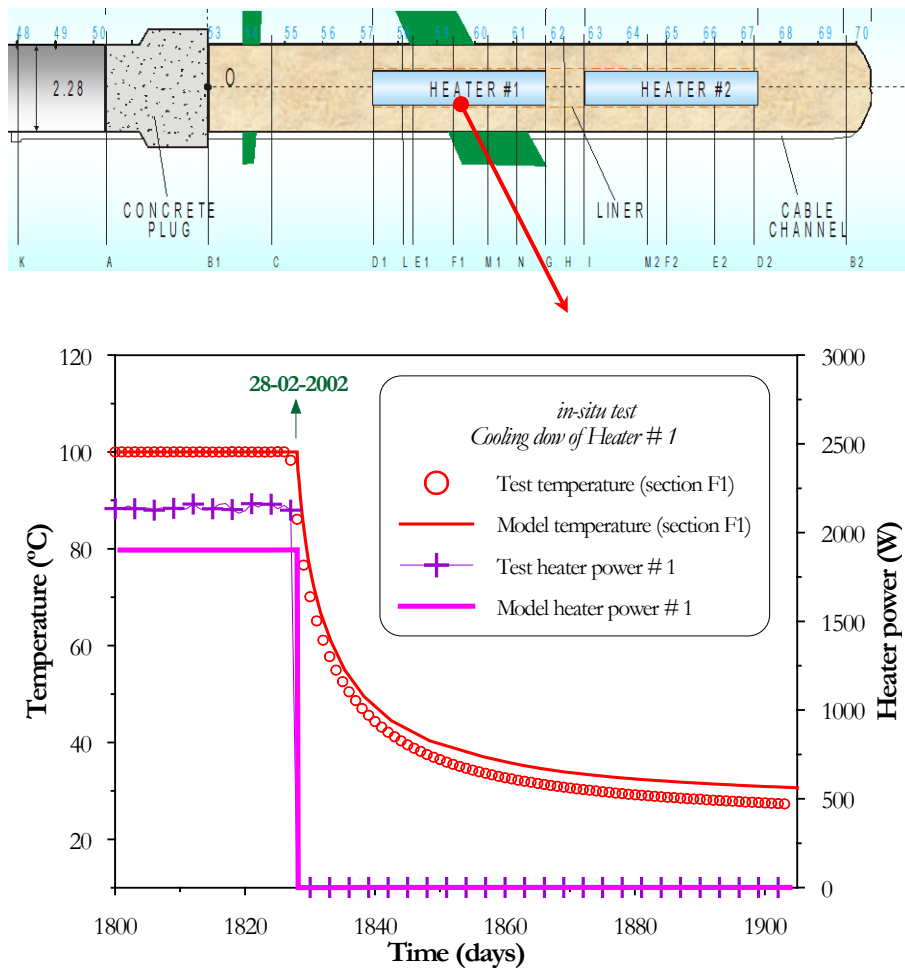
Fig. 2-5:   Evolution of temperature and power of Heater #1 shortly before switch-off and during cooling.

Simulation of the first dismantling involving Heater #1

The following stages have been considered in the numerical analysis of the first dismantling involving Heater #1:

Start of plug demolition:	02.04.2002	– day 1860
End of plug demolition:	28.05.2002	– day 1916
Start of bentonite excavation:	29.05.2002	– day 1917
Start of Heater #1 extraction:	19.06.2002	– day 1938
End of excavation:	19.07.2002	– day 1968

The dates used for these modelling stages correspond to the exact dates in the experiment (Bárcena et al. 2003). Fig. 2-6 shows the dismantling steps considered in the analysis and the corresponding times schematically.
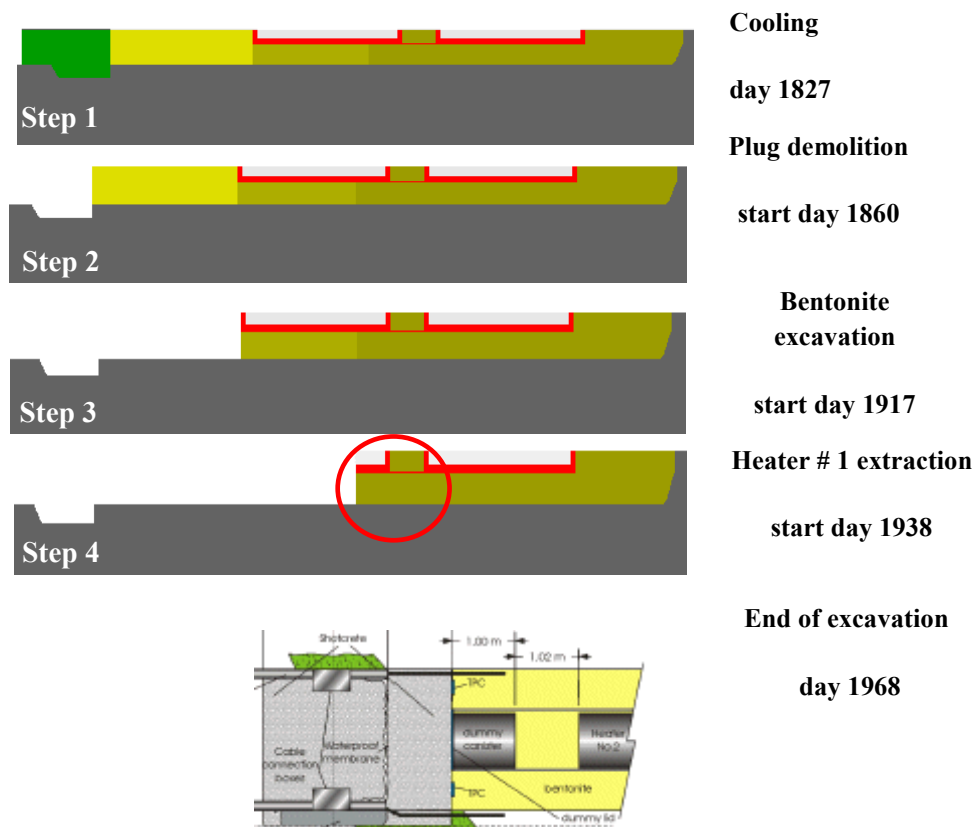
Fig. 2-6:   Excavation stages considered in the modelling of the first dismantling (Heater #1).

Fig. 2-7a and 2-7b present the contours of longitudinal displacement and axial stress computed at the different excavation stages. The high swelling capacity of the FEBEX bentonite and the confined conditions of the test induce the development of high swelling pressures in the clay barrier. As expected, axial displacements and reduction of axial stresses in the clay barrier are predicted after concrete plug demolition and subsequent excavation. It can also be observed that the effect of the relaxation of confinement during excavation is relatively local and mainly affects the zones close to the advancing front.
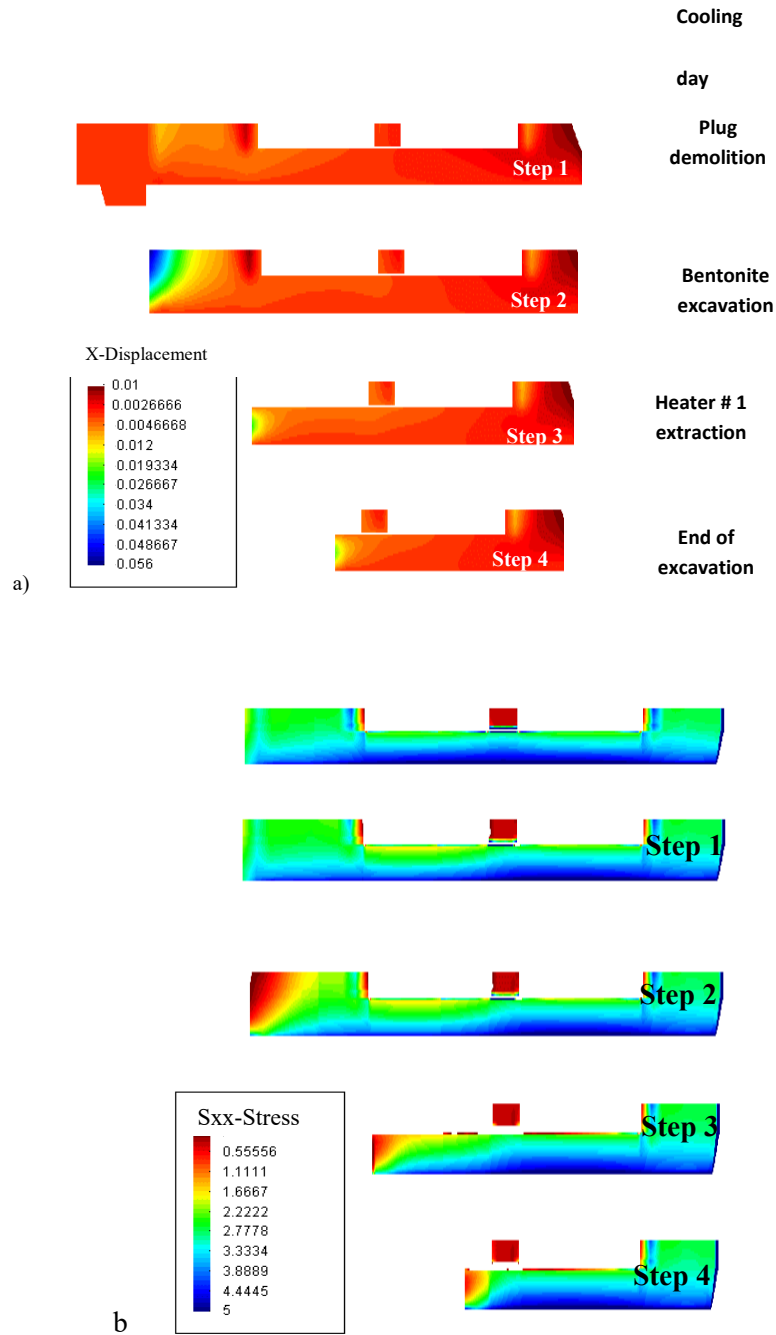
Fig. 2-7: Excavation Heater #1: contours of a) displacement, and b) axial stress during excavation (compression is considered positive).

THM behaviour during cooling down and dismantling of Heater #1

The first dismantling was carried out with the fundamental aim of maintaining Heater #2 and all the sensors in the clay barrier and surrounding rock operative throughout the process. This has provided the opportunity to analyse the evolution of the main THM variables of the problem during the cooling down of Heater #1 and the subsequent excavation. The analysis of the main sensor measurements in both the bentonite barrier and surrounding rock and their comparison with the model predictions are discussed next. The results are presented for times ranging from day 1750 (i.e. a few days before switching off Heater #1) to one thousand days later, when the transient processes induced by the first dismantling appear to have disappeared. In those sections that were dismantled, the experimental observations are presented until the time at which the sensors were removed from the experiment.

With regards to the thermal behaviour of the clay barrier, the model predicts the decrease of temperature at different sections close to Heater #1 very well. This can be seen, for example, in the comparison between measured and simulated temperatures in sections G and I, shown in Fig. 2-8a and 2-8b, respectively.

As expected, the disconnection of Heater #1 strongly affected the hydraulic behaviour of the clay barrier in its vicinity. This is mainly because of the key effect of water vapour transfer phenomena on clay barrier hydration. During heating, an increase of the water vapour concentration is expected near the heater. Consequently, water vapour from the internal part of barrier moves outwards driven by the gradient of vapour concentration; which is governed by Fick's law. When this water vapour front reaches zones of lower temperature, the water vapour condensates and turns into liquid. The corresponding behaviour during cooling can be observed in Fig. 2-8c. Just after turning off Heater #1 (day 1827), a rapid increase of the relative humidity was observed in zones close to the heater (i.e. radii r = 0.52 m, Fig. 2-8c due to the lack of water evaporation (and the corresponding drying). Furthermore, the progressive increase of relative permeability further out in the buffer contribute to the hydration in the form of advective liquid fluxes. As hydration progresses, the hydraulic gradient decreases and consequently the hydration rate of the barrier diminishes progressively. The sensors confirmed the model predictions while they were operative.

A different behaviour was observed at intermediate radii of the barrier, where a moderate reduction of the relative humidity during cooling down is recorded (i.e. r = 0.82 m, Fig. 2-8c). This apparent drying is attributed to two main factors. On the one hand, vapour transfer from the heater surface stopped when Heater #1 was turned off (as explained above), and therefore water vapour was no longer arriving in these intermediate zones. On the other hand, after Heater #1 was turned off an increase in the liquid water transfer from the external part to the internal part of the barrier in the form of advective flux took place (as explained above). These two factors contribute to the reduction of the availability of liquid water in this zone of the barrier. Finally, the zones near the host rock were not affected by the cooling down of the barrier (i.e. r = 1.10 m, Fig. 2-8c).

Section H was moderately affected by the thermal changes induced during the switch-off of Heater #1 due to its relative proximity to it. The trends in Section H are qualitatively similar to the ones observed in Section E1 (commented above), but with a less marked effect of the temperature variations (Fig. 2-8d). The model also describes the main trends observed in this section well, but with a slight under-prediction of the relative humidity in the section closer to the heater.

It can be concluded that the model provides a reasonable overall prediction of the experimental observations, as described above. Note that capacitive type transducers manufactured by Vaisala

(Huertas et al. 2006), were used to measure the relative humidity. This type of sensors automatically accounts for the effect of temperature on relative humidity, so the measurements shown in Fig. 2-8d depend on the local wetting or drying of the bentonite in the vicinity of the sensor.

Regarding the evolution in the host rock, the changes observed in the thermal field depend on the distance to Heater #1. For example, Fig. 2-9a shows the simulated and observed temperature shortly before and after switch-off in borehole SF24. Just before switching off Heater #1, the maximum temperature at the sensor nearest the clay barrier (i.e., r = 1.3 m, measured from the axis of the drift) was around 42.5 °C, and a reduction of around 3 °C was recorded just after Heater #1 was turned off. At a distance of 2.9 m the reduction of temperature was around 2.5 °C and the changes were practically imperceptible at a distance of 9 m. Moving away from the heaters' zone, the temperature around the barrier decreases. For example, Fig. 2-9b shows that in borehole SB12 (near the concrete plug) the temperature close to the gallery (i.e. r = 1.41 m) was around 19 °C and it reduced by around 5 °C after Heater #1 disconnection. The model was able to predict the temperature evolution in these two different zones very well.

Cooling down and the first dismantling slightly affected the liquid pressure in the host rock. Fig. 2-9c shows the results of a piezometer. It is clear that the model underestimates the observed change in the liquid pressure. With regards to the mechanical behaviour, a noticeable reduction of the normal stresses can be observed (Fig. 2-9d). This behaviour can be associated with two main factors:

a) the contraction of materials during cooling

b) the removal of the clay barrier in Heater #1 zones, with the corresponding release of the bentonite swelling pressure acting against the gallery rock

The fact that the more significant reduction of stresses took place just after switching off Heater #1 indicates that the first factor is the more influential one. As for the stresses in rock mass, the model underestimates somewhat the strong stress decrease observed just after switching off Heater #1 but it predicts the stress field variations observed afterwards reasonably well.
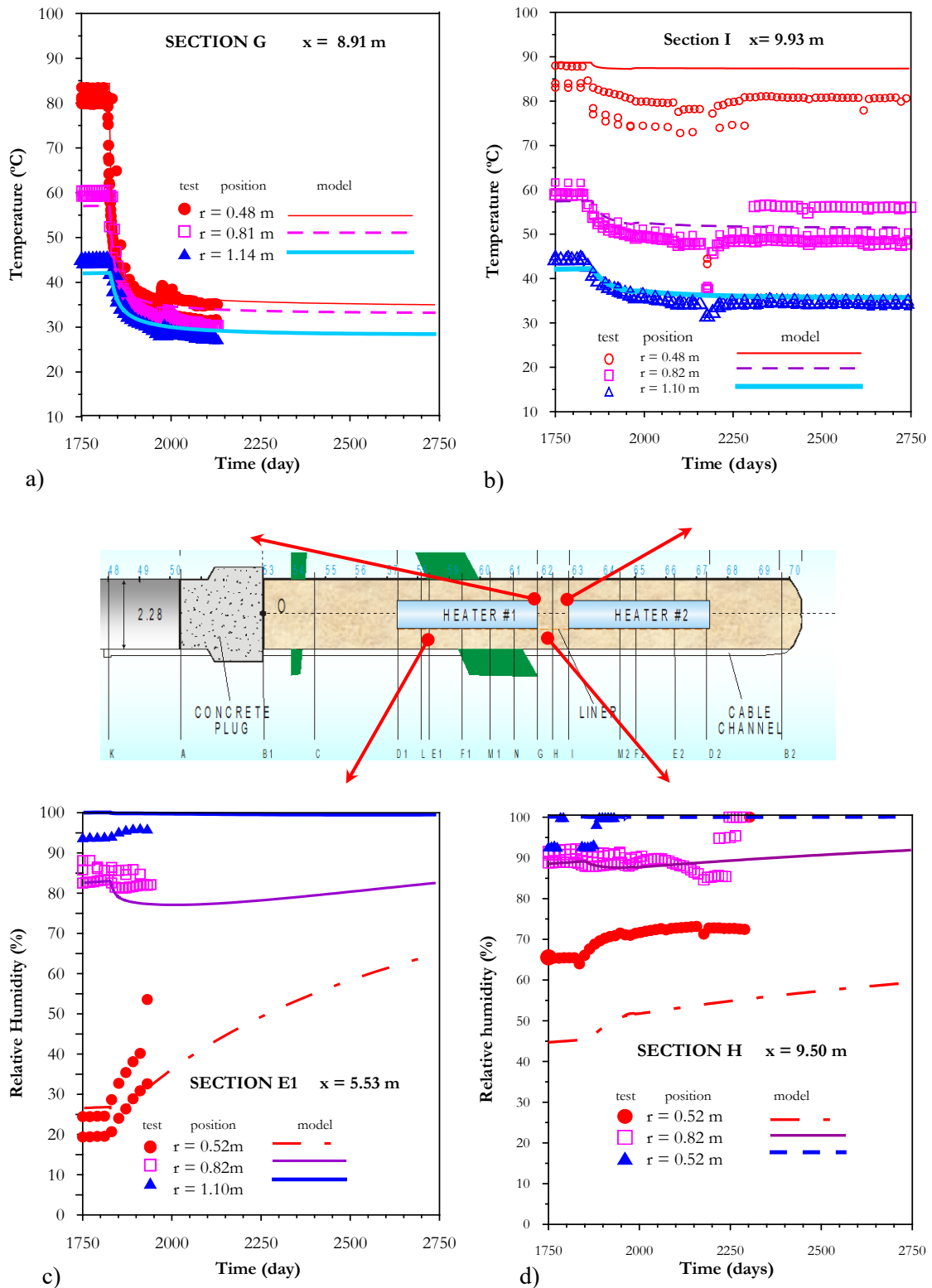
Fig. 2-8:   Evolution of temperatures and relative humidity in the clay barrier shortly before and after switch-off of Heater #1: Observed versus computed values of: a) temperature in Section G; b) temperature in Section I; c) relative humidity in Section E1; and d) relative humidity in Section H.
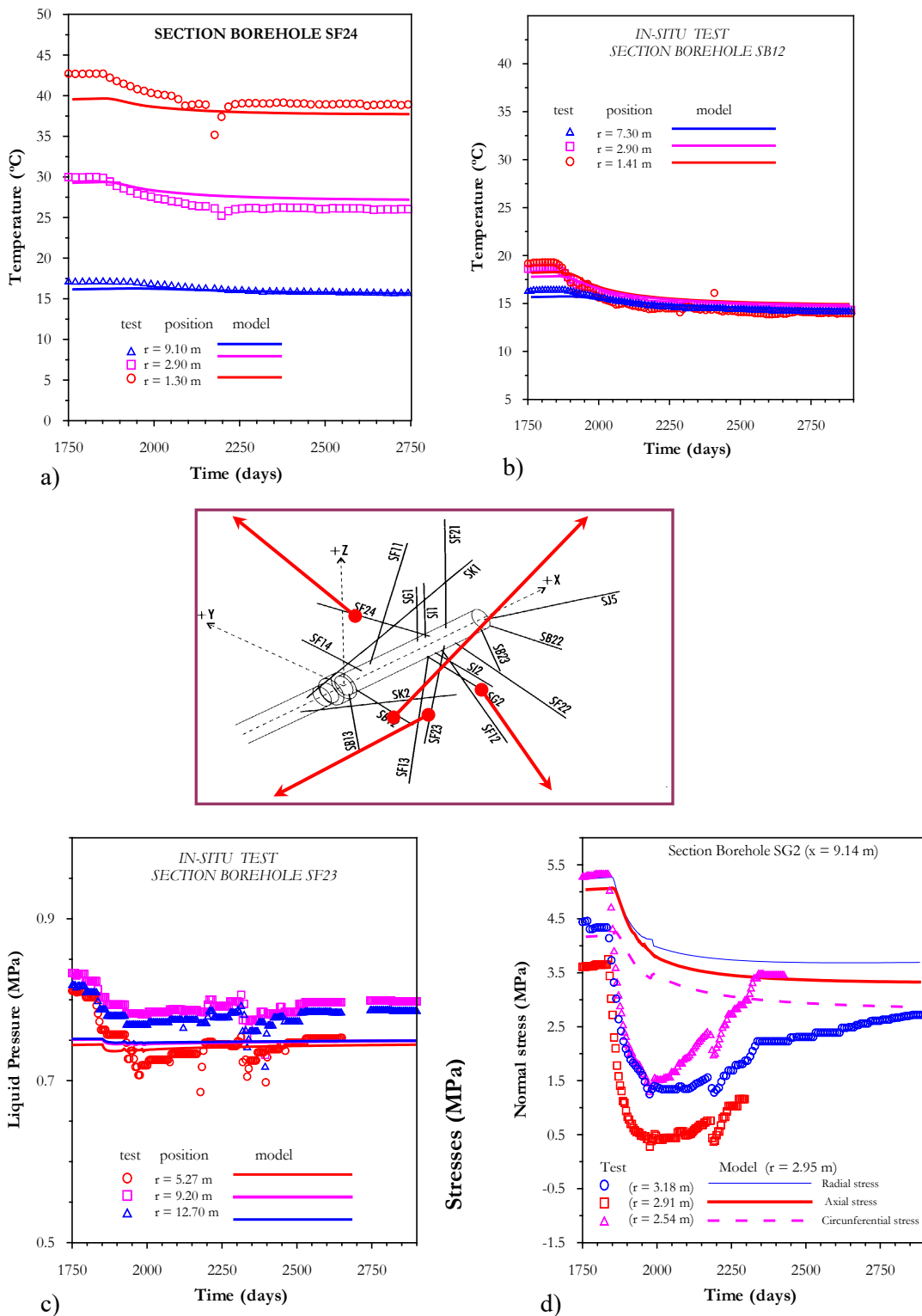
Fig. 2-9:   Evolution of temperatures, liquid pressure and stresses in the host rock shortly before and after switch-off of Heater #1. Observed versus computed values of: a) temperature in SF24; b) temperature in SB12; c) liquid pressure in SF23; and d) stress in SG2.

Analysis of the post-mortem tests related to the clay barrier involving Heater #1

During the first dismantling, various sections were earmarked for sampling. A detailed description of the dismantling procedures is presented in Bárcena et al. (2003). This first dismantling allowed the direct and detailed observation of the state of the barrier after five years of heating and hydration (Gens et al. 2009). In addition, large amounts of quantitative data could be obtained: this information is very valuable for providing an independent check on the performance of the numerical model, as well as on the reliability of the predictions. At selected sections, a large number of specimens were cored from the barrier, and dry density and water content were determined immediately in a field laboratory in order to minimize disturbance and humidity loss. This comprehensive set of values of dry density and water content helped to provide a complete picture of the state of the bentonite barrier. Block samples were also taken for laboratory testing, but those results are outside the scope of this report (Villar et al. 2005). Thanks to the high density of measurements, contours of dry density and water content could be plotted in the sampled sections (Gens et al. 2009). From these plots, it could be observed that the process of hydration and associated density changes is basically axisymmetric, supporting the assumption made in the numerical analysis (Gens et al. 2009). The post-mortem measurements are compared to the values from the simulation including the cooling stage and the excavation performed prior to sampling. Dismantling operations lasted for two months; the time required to reach each particular sampling section has also been incorporated in the modelling analysis.

Fig. 2-10 shows the values of water content and dry density as a function of distance to the tunnel axis measured with the post-mortem tests at a section near the centre of Heater #1. The same figure shows a comparison to the values simulated with the OBC model. This section is representative of a hot region of the test and is, therefore, referred to as a "hot section". It can be seen that water content increases closer to the rock due to the process of natural hydration from the rock. It is also indicated that the part of the barrier close to the heater remains below its initial value of water content, which is a consequence of the strong drying that occurred in this area before Heater #1 was switched off. Although a certain amount of water has already reached the inner region, it is still insufficient after 5 years to compensate for the initial drying. It is also noticeable that the barrier as a whole is very far from full saturation at the end of the heating phase.

The distribution of dry density in the "hot section" shows that the clay has expanded close to the rock, as indicated by values of dry density well below its initial value. On the other hand, the dry density in the zone near the heater has increased. Because of the confined nature of the test, the variation of dry density in the inner part is compensated for by the reduction of dry density in the outer part. The change of dry density (i.e. porosity) is the combined effect of expansion due to temperature increase (thermal effect), suction changes (hydraulic effect) and stress increase due to the development of swelling pressure (mechanical effect).

Fig. 2-11 presents water content and dry density for another "hot section" around Heater #1, showing the reasonable agreement between measured and simulated values.
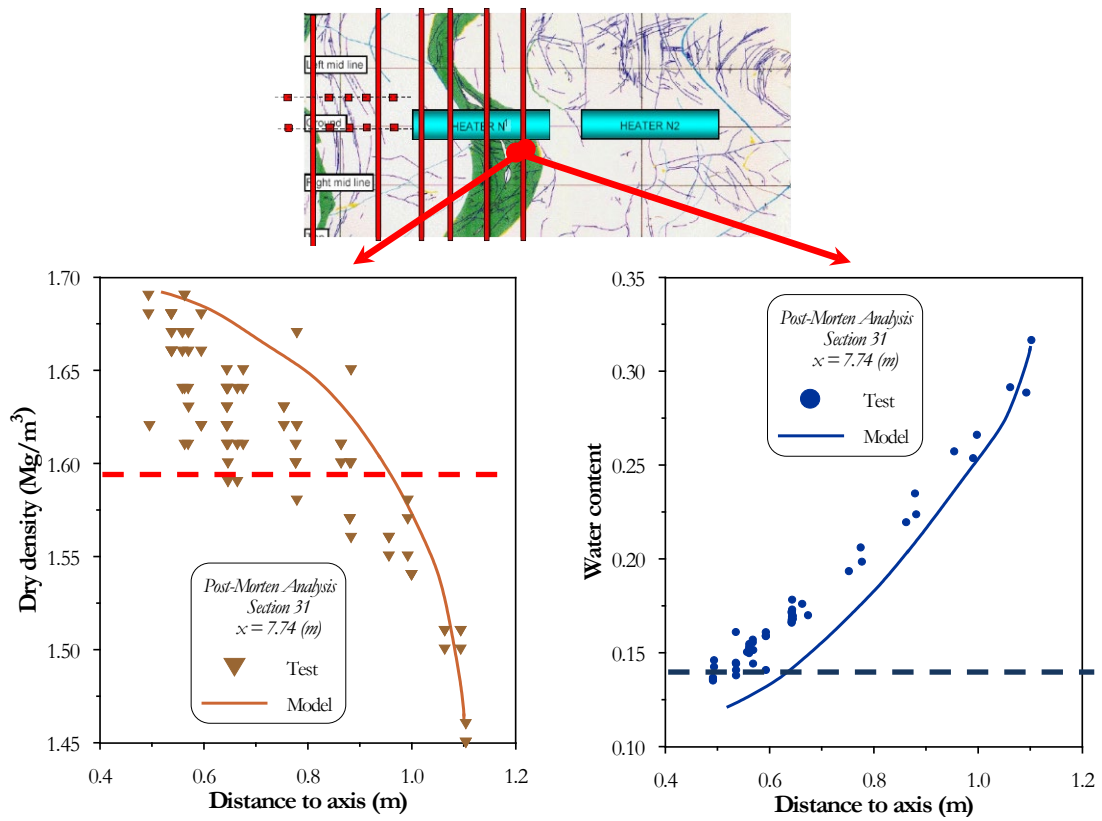
Fig. 2-10:   Values of (a) water content and (b) dry density measured during dismantling in
              Section 27 (hot section): observations and computed results.
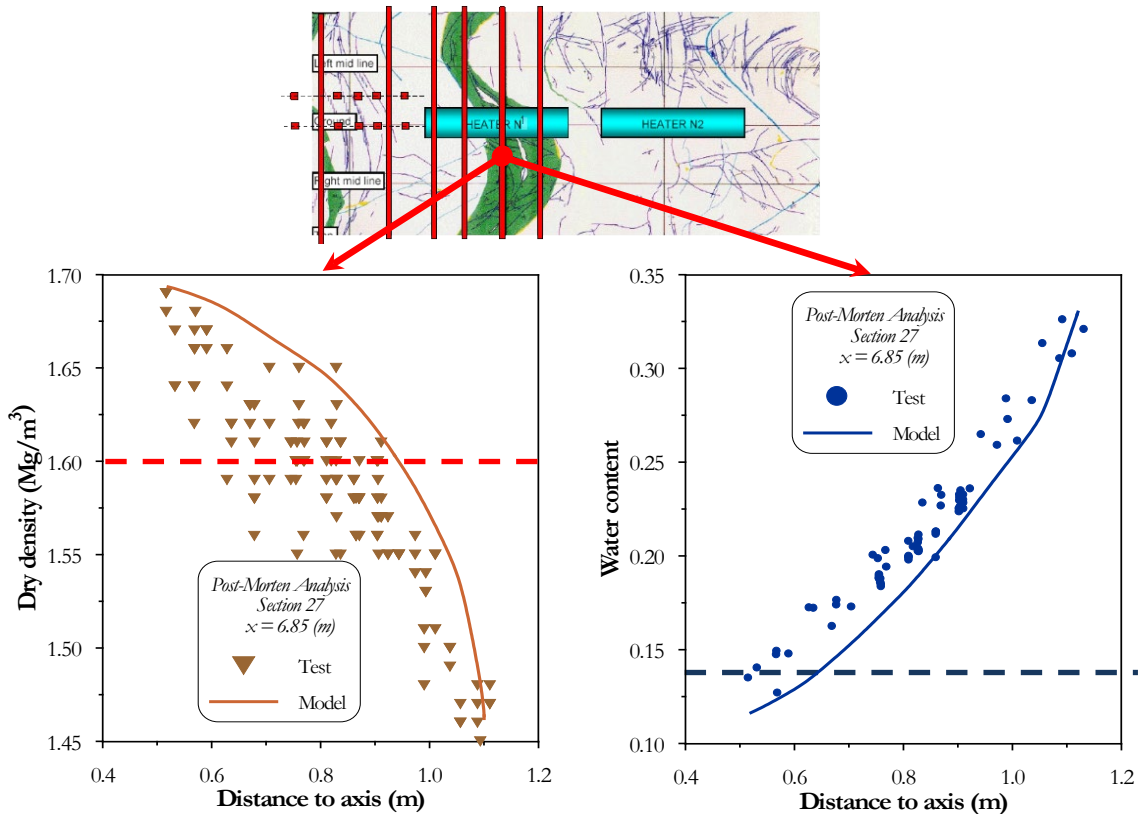
Fig. 2-11:   Values of (a) water content and (b) dry density measured during dismantling in Section 31 (hot section): observations and computed results.

Water content and dry density values are also plotted for a section between the tunnel plug and Heater #1, referred to as a "cool section" (Fig. 2-12). In this case, the temperature increase is very limited and some differences are observed in the patterns of observed water content and dry density compared to the "hot section". Water content in the "cool section" increases closer to the rock, but there is also a net (albeit small) increase of water content near the centre of the tunnel. There has been no drying in this region, but the amount of hydration is very small, even after five years, because of the thickness of the barrier in this section. The dry density also shows a significant reduction closer to the rock, but a somewhat smaller increase in the inner part, where the change appears to be more uniform; the net volume change of the section is quite small. Similar to the previous, it is indicated that the OBC model captures the general experimental trend well.
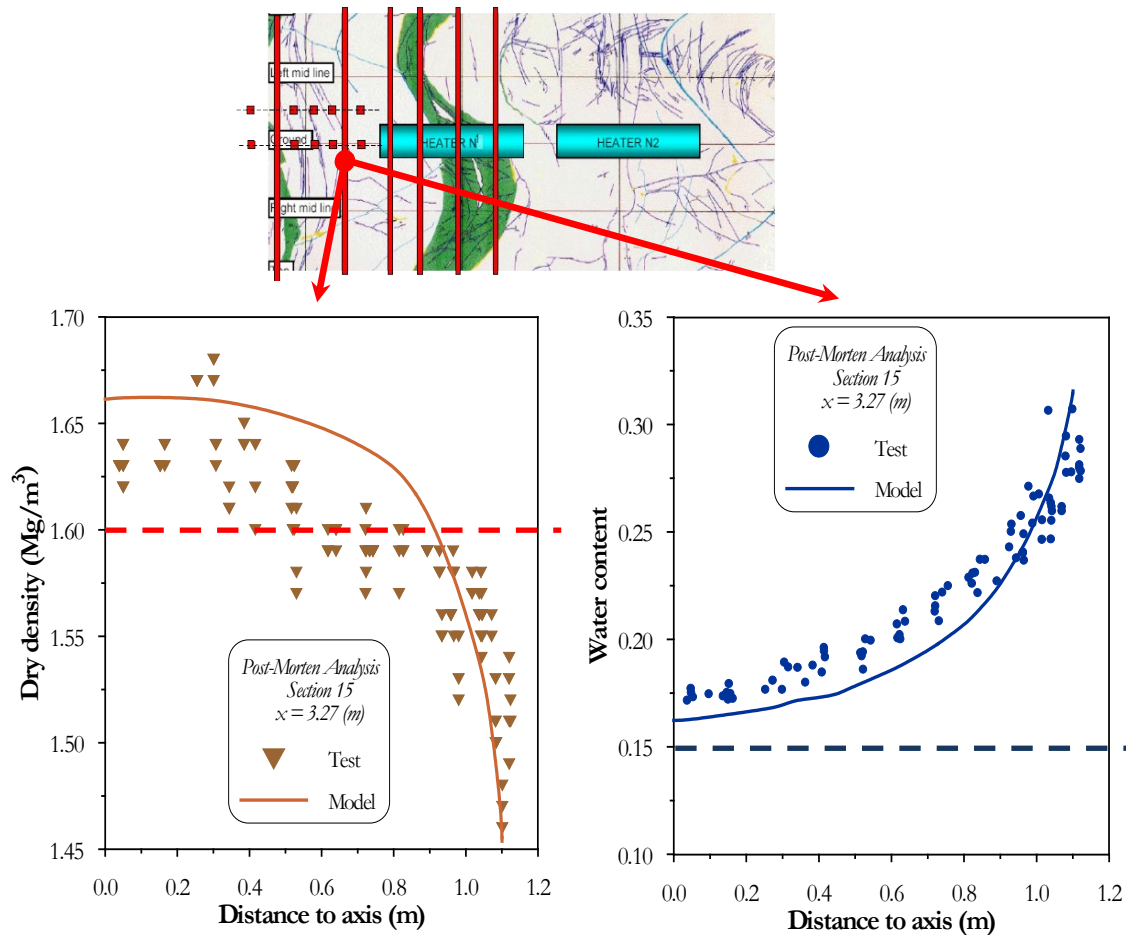
Fig. 2-12:   Values of (a) water content and (b) dry density measured during dismantling in Section 15 (cool section): observations and computed results.

The simulation results presented here are essentially blind predictions as they correspond to the OBC analysis that had been formulated at the start of the heating test. The results of the numerical analysis show very good agreement with the measurements taking into account the coupled THM phenomena that occur in the early stages of the experiment as compared to the long-term behaviour of the later stages. The patterns of the hot and cool sections are reproduced very well by the model, and the quantitative agreement between observations and predictions is satisfactory. However, a closer comparison between observations and predictions indicates some systematic differences. In all sections, the observed water content is somewhat higher than the computed one, especially in the middle and inner regions of the barrier. Similarly, there is a certain over-prediction of dry density also observed in the middle and inner regions of the barrier.

Simulation of the second dismantling involving Heater #2

The following stages have been considered in the numerical analysis of the second dismantling:

Cooling of Heater #2:	20.04.2015	– day 6621
Start excavation up to Heater #2 (Step 6)	11.05.2015	– day 6642
Start excavation up to half Heater #2 (Step 7)	01.06.2015	– day 6663
Start excavation bentonite up to end of Heater #2 (Step 8)	22.06.2015	– day 6684
Start excavation bentonite up to end of experiment (Step 9)	06.07.2015	– day 6698
End of excavation:	20./07.2015	– day 6712

The dates associated with the stages considered in the analysis are based on those provided by Nagra. Fig. 2-13 shows the dismantling steps considered in the analysis and the corresponding times schematically.

Fig. 2-14a and 2-14b present the contours of longitudinal displacement and axial stress computed at the different excavation stages associated with the second dismantling (Heater #2). The high swelling capacity of the FEBEX bentonite and the confined conditions of the test induce the development of high swelling pressures in the clay barrier. As expected, axial displacements and reduction of axial stresses in the clay barrier are predicted after concrete plug demolition and subsequent excavation. It is also indicated that the effect of the relaxation of confinement during excavation is relatively local and mainly affects the zones close to the advancing front.
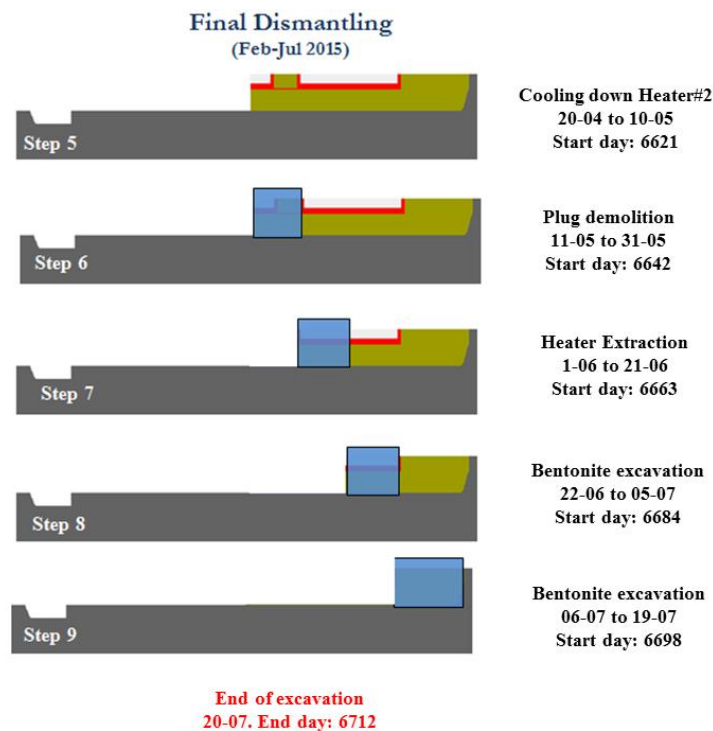
Fig. 2-13:   Excavation stages considered in the modelling of the second dismantling (Heater #2).
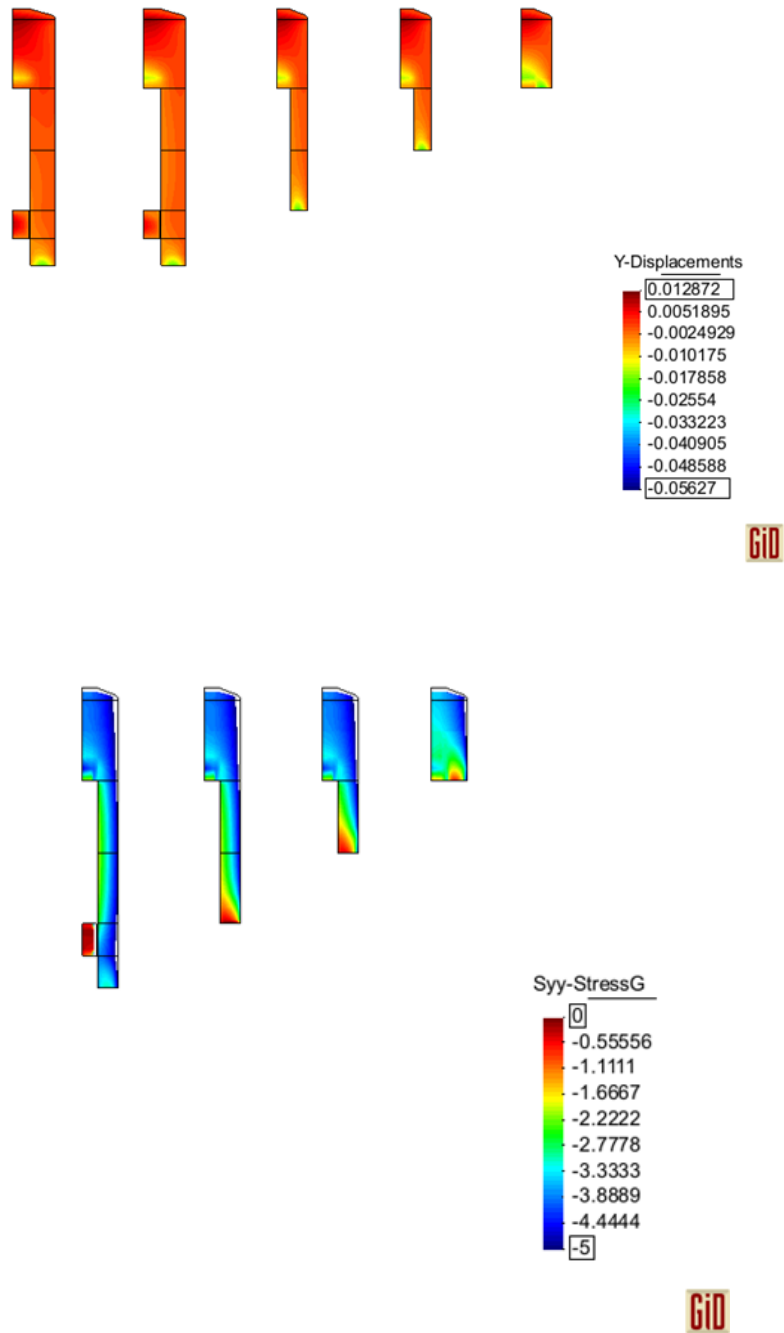
Fig. 2-14:   Excavation Heater #2: a) contours of displacement, and b) of axial stress during
             excavation (compression is considered positive).

Analysis until the switch-off and excavation of Heater #2

In this section, the model predictions of the OBC prior to switching off Heater #2 are presented. The evolution of temperature, relative humidity, and stress is presented for selected sections in Fig. 2-15. Fig. 2-15a shows the evolution of temperature at Section D2. It can be observed that the model captures the overall thermal trend of the test well.

As mentioned in the analysis presented for the switch-off and excavation of Heater #1, the presence of heterogeneities in the natural system make predictions of the hydration of the clay barrier a challenging task. Moreover, several sensors are out of order in this advanced stage of the experiment, resulting in a limited amount of experimental data that can be used for model validation. Nevertheless, it can be said that the response of the model seems satisfactory globally. The comparison between measured and simulated relative humidity is shown in Fig. 2-15b and 2-15c for sections G and I, respectively. It is indicated that in Section G (close to the end of the former Heater #1), the model slightly over-predicts the saturation of the barrier at the location of the sensor closest to the tunnel axis (i.e. $r = 0.60$ m).

Thermal effects are more influential in Section I, where the model predicts a dryer inner barrier compared to Section G (Fig. 2-15b, 2-15c). The relative humidity sensor located closest to the tunnel axis at Section I ($r = 0.60$ m) indicates an even lower saturation. However, the trends observed in the measurements of this sensor make the reliability of these readings questionable. The external part of the barrier is fully saturated, as indicated by the measured and simulated values closest to the rock.

As discussed in the analysis for the switch-off and excavation of Heater #1, a significant increase of the stress level has been observed during hydration. This is due to the confined conditions of the clay barrier and the high swelling of the heavily compacted bentonite. Fig. 2-15d presents the evolution of stresses at Section F2. It is observed that stresses continue to increase at the very advanced stages of the experiment, whereas the model predicts a gentler increase of stresses over time.

Fig. 2-16a to 2-16c shows the measured and simulated temperature and liquid pressure in the rock around the clay barrier indicating the thermo-hydraulic behaviour. The results show the effect of the Heater #1 switch-off (day 1827) affecting the nearfield and inducing a transient thermal phase that lasted for approximately three years. This transient effect is more pronounced in locations close to Heater #1. The model provides a good prediction of the measured temperature decay in the granite. In the long term a very slow increase of temperatures is observed in the host rock which is more pronounced in the experimental observations. On the other hand, liquid pressures remain practically constant in the long term. As shown in Fig. 2-16c and 2-16d, pressures remain practically unchanged after a porewater pressure increase during the initial heating, which is also reproduced by the model. The switch-off of Heater #1 has a relatively insignificant impact on the liquid pressure, as indicated in both experimental observations and numerical results.
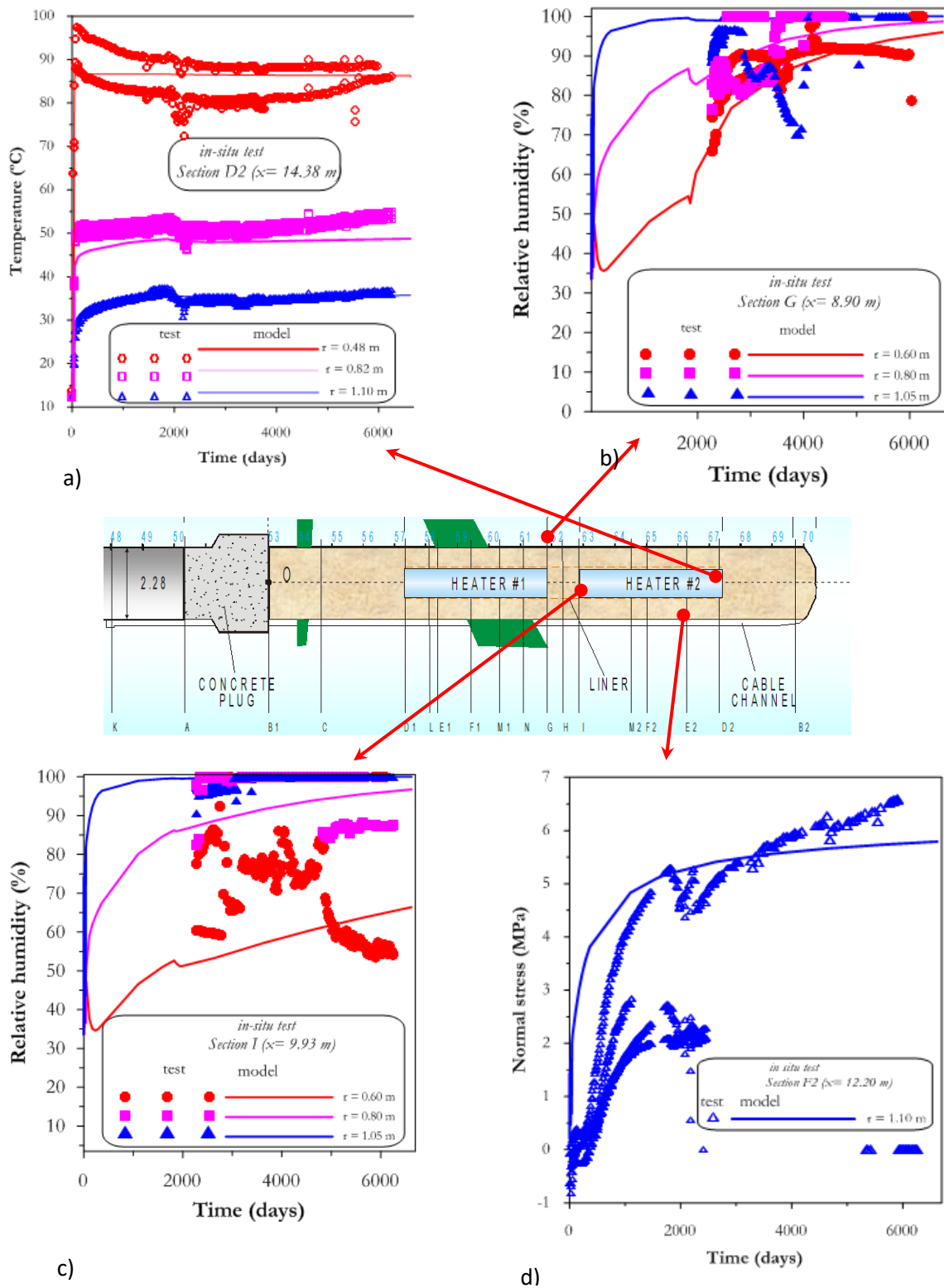
Fig. 2-15: Evolution of main variables in the clay barrier; observed versus computed values (OBC model) a) temperature in Section D2; b) relative humidity in Section G; c) relative humidity in Section I; and d) stresses in Section F2.
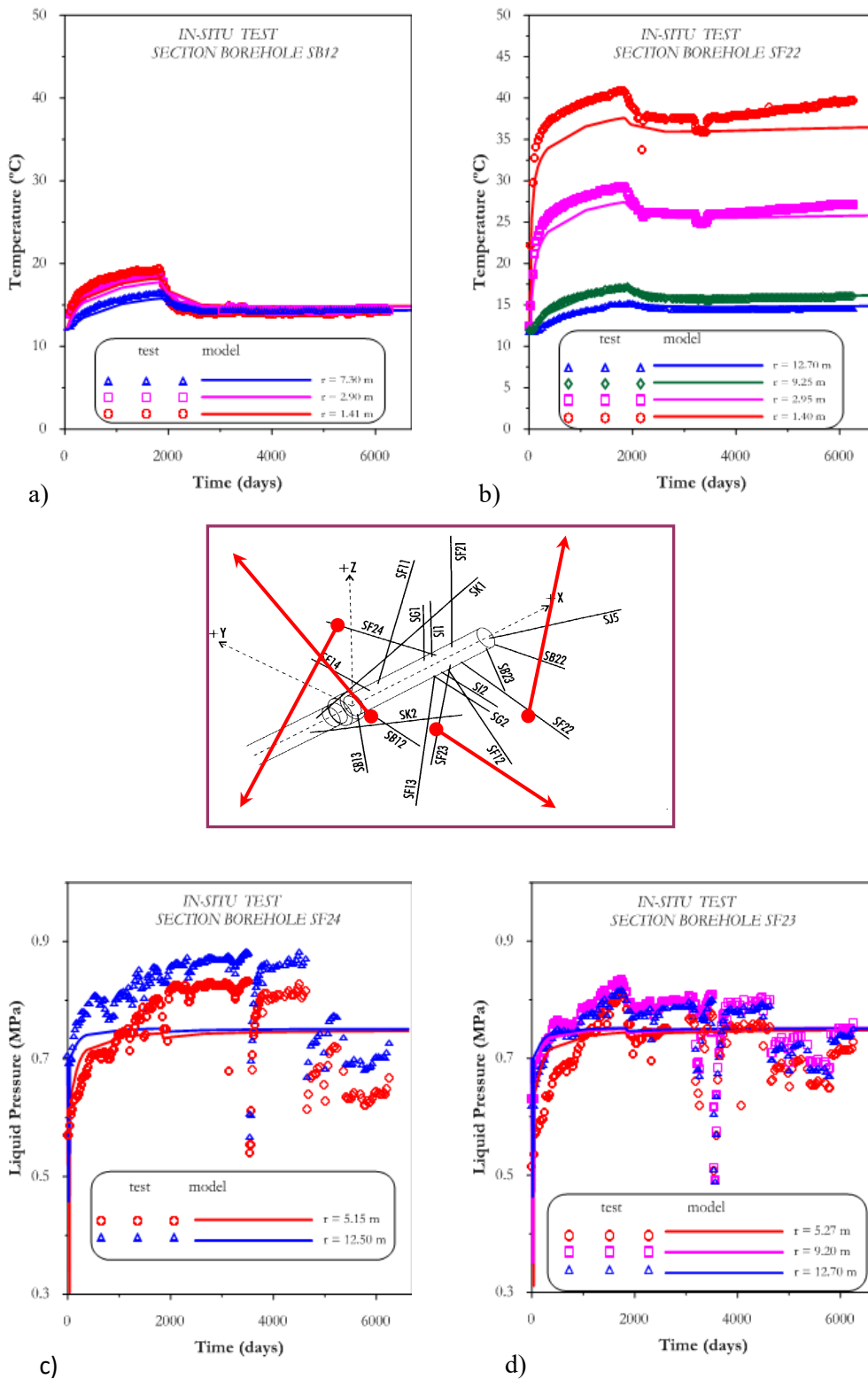
Fig. 2-16:   Model predictions of TH variables in the host rock. Observed versus computed values of: a) temperature in borehole SB12; b) temperature in borehole SF22; c) liquid pressure in borehole SF24; d) liquid pressure borehole SF23. Middle panel: radial borehole layout ().

2.5   Interpretation of the results

A detailed interpretation of the model results was performed in the previous sections through the comparison to the experimental data. The main conclusions are summarized in this section.

The results of the numerical analyses involving the different components and stages of the FEBEX Grimsel experiment presented in the previous sections have been obtained with the Operational Base Case (OBC) model. As mentioned earlier in this report, the OBC model was prepared at the beginning of the experiment, and no further modifications have been incorporated afterwards. In this context, the results obtained with this model can be considered as blind predictions from the start of the test. It is also important to highlight that the experimental information available at that time of the calibration of the constitutive models was quite limited. Therefore, some differences between the experimental data and the model predictions can be anticipated, particularly when modelling a complex THM test performed under natural conditions.

In general terms, it can be stated that the performance of the model is globally satisfactory. The main tendencies observed in the test associated with the more relevant THM variables are captured correctly by the model, both in terms of time evolution and post-mortem results. A tendency to slightly under-predict the moisture in the inner parts of the clay barrier was observed in the comparisons between model output and post-mortem tests. However, it is worth highlighting that in terms of the comparisons involving time evolution, the model appears to over-predict the saturation of the barrier in several sections (e.g., Fig. 2-4c, 2-15b and 2-15c). A similar behaviour is observed in the FEBEX mock-up test. This presumably relates to the conceptual uncertainty in the model representation (i.e., related to local effects and associated variations of state variables) and to some extent also to the measurement uncertainty (i.e., sensor calibration). Such aspects require further study and interpretation including a systematic uncertainty analysis that is beyond the scope of this report.

2.5.1   Driving processes

The main driving processes in this type of problem have been extensively discussed in several publications (e.g. Gens et al. 1998, 2009; Sánchez et al. 2012). The main phenomena and interactions are briefly described in the following. The major actions that affect the bentonite barrier are heating and hydration from the surrounding rock. At the inner boundary, the barrier receives a very strong heat flux from the heaters. The dominant heat transfer mechanism is conduction through the three phases of the material. A temperature gradient will therefore develop in the near field, and heat dissipation will basically be controlled by the thermal conductivity of the clay barrier and surrounding host rock. In the inner zones of the barrier, the heat supplied by the heater results in a large temperature increase and the associated water evaporation, which results in bentonite drying. The degree of saturation and water pressure will reduce significantly in this region. Vapour arising from the drying of the bentonite will move outwards until it finds a cooler region, where it will condense, causing a local increase in water saturation. Vapour diffusion is a significant mechanism of water transfer, and it also contributes, albeit to a much lesser extent, to heat transport. Owing to the high suction initially present in the unsaturated material that constitutes the backfill, hydration will occur, with water moving from the host rock into the barrier. The distribution of water potential inside the clay barrier is strongly affected by the phenomena of bentonite drying and vapour transport, as described above. Hydration should eventually lead to saturation of the barrier, but full saturation times can be very long, owing to the low permeability of the bentonite and/or the host rock. In addition to the thermo-hydraulic behaviour, there are also important mechanical phenomena occurring. Drying of the bentonite will cause shrinking of the material, whereas hydration will produce

swelling, which may be quite pronounced in highly compacted bentonite barriers. Because the barrier is largely confined between the heater and the rock, the main result of hydration is the development of swelling pressures in a process quite akin to a swelling pressure test. The magnitude of the stresses developed is critically dependent on the emplacement density of the bentonite, and may reach values of several MPa, as it was observed in the FEBEX in-situ test.

2.5.2 Modelled density, saturation distributions and the remaining uncertainties

The predictions of dry density and saturation distributions will be evaluated at a "hot section" (F2) and a "cold section" (G) for subsequent comparison to the post-mortem measurements from the second dismantling (Fig. 2-17).
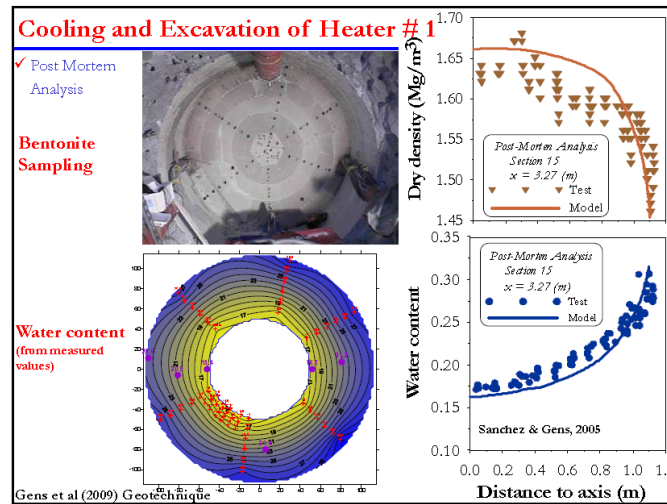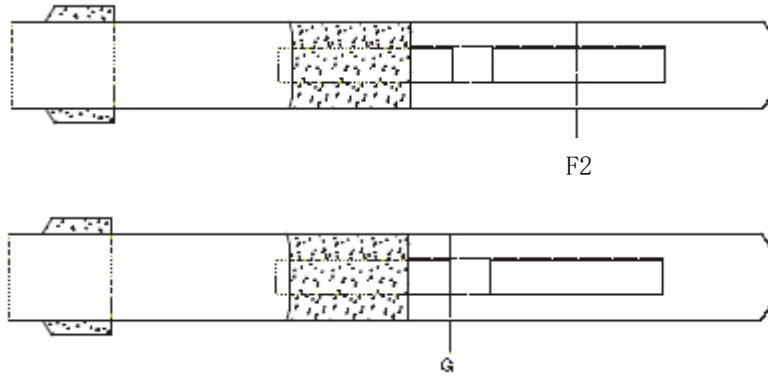
Fig. 2-17: Selected cross-sections for comparison to the measurements after the second dismantling (top); dry densities and water contents measured at corresponding hot and cold sections after the first dismantling.

The model predictions in terms of water content and dry density after the second dismantling are presented for Section F2 in Fig. 2-18a and 2-18b, respectively. The comparison of these blind predictions to the measurements obtained after the dismantling of Heater #1 (Fig. 2-17) shows that the progress of the hydration front in the inner part of the barrier is slower in the model. The model predictions for the second dismantling indicate minor changes in terms of water content compared to the values from the first dismantling. Furthermore, the OBC resulted in somewhat lower values of water content when compared against the post-mortem experimental results. Considering that the post-mortem tests were performed after five years of heating and hydration, it is expected that predictions made for the entire lifetime of the experiment (eighteen years of heating and hydration) will possibly under-predict the moisture content of the barrier compared to values measured after the second dismantling. In terms of dry density, the model does not indicate significant changes compared to the observations obtained with the first dismantling. However, this predicted behaviour is a direct consequence of the mechanical constitutive law used (see more details in Section 2.5.3). An additional model prediction is shown in Fig. 2-18b, taking into account the changes in dry density that may occur due to the unloading process during the extraction of the sample; it is represented by a dashed line.

a)   b)
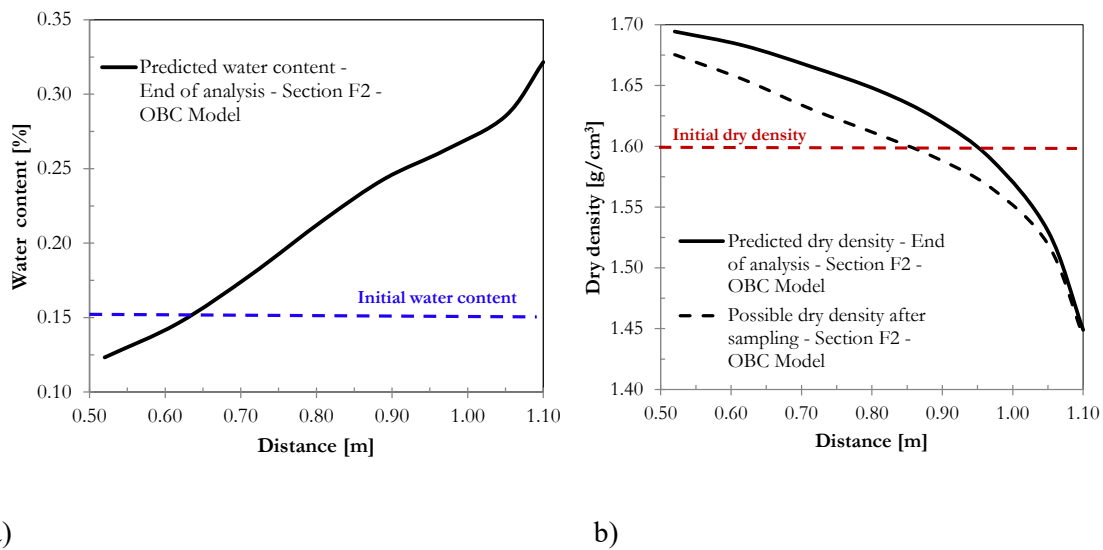
Fig. 2-18:   Section F2, predicted values of (a) water content and (b) dry density.

In Section G, the OBC model considered the presence of a steel liner at a radius of 0.45 m. This is noted in the model predictions of the dry density with a discontinuity at the liner position. It is worth mentioning that the mesh discretization inside the liner is not refined, so model predictions may not be very accurate. It is also worth noting that this section may be influenced by the proximity to the shotcrete plug. The model predictions in terms of water content and dry density for Section G are shown in Fig. 2-19a and 2-19b, respectively. An estimation of the possible changes in dry density during sample extraction is also shown in Fig. 2-19b.
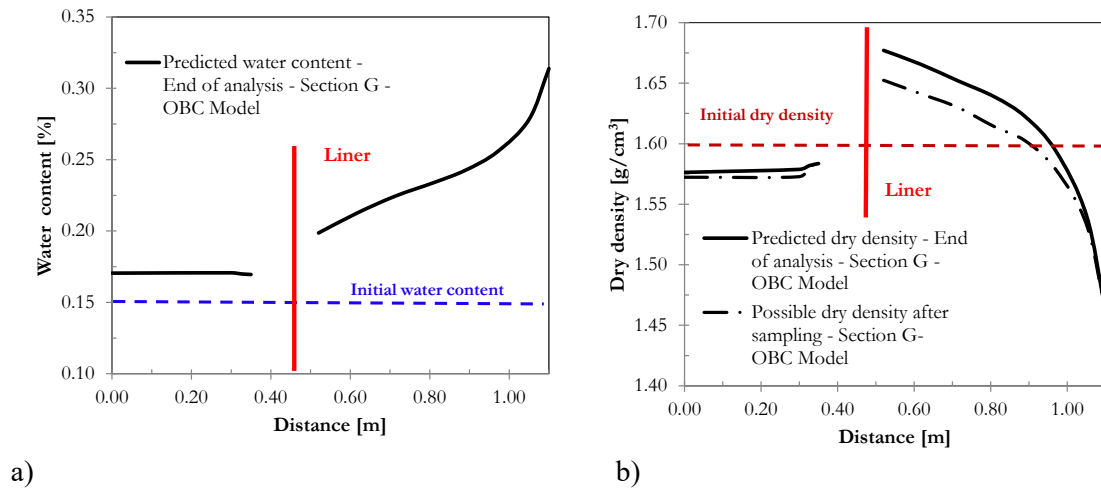
Fig. 2-19:   Section G, predicted values of (a) water content and (b) dry density measured.

2.5.3   Progress made in this exercise, remaining uncertainties

An issue identified in this study is the long time required to complete the experiment. The understanding and modelling of the hydration of expansive clays is a topic that still requires significant research effort. The behaviour of swelling clays is complex and the prediction of their hydration under repository conditions is a challenging task.

However, the analysis of the hydration of the FEBEX in-situ test contributes to advance the current state of understanding in this subject. For example, the first dismantling involving Heater #1 and the associated post-mortem analyses of the clay barrier material allowed to assess the predictive capability of the numerical models used to predict the THM behaviour in this study. A strong element of the performed numerical analyses is the ability of the proposed formulation and models to properly capture the main tendency observed in the experiment, and in many cases, provide blind predictions, at least in qualitative terms.

Very importantly, since no recalibration of the model was made using the post-mortem observations after 5 years of heating, the performance of the OBC model with respect to the longer-term behaviour of the barrier can be improved using the incremental results from first dismantling to second dismantling instead of using directly the computational results for the whole experiment.

Concerning uncertainties, no systematic analysis was made in the context of this project. However, different sets of parameters and constitutive laws are likely to be applicable and, being consistent with available experimental observations, may result in different predictions for the outcome of the experiment. To illustrate this point and to provide an example of the uncertainties involved, a partial deterministic sensitivity study has been carried out to demonstrate the effect of small variations in the retention curve on predictions. From past experience, it is known that hydraulic results are often sensitive to the specific retention curve adopted.

The range of retention curves used in this set of analyses involves the following values of the parameter P_0: 7 MPa (OBC), 12 MPa, 16 MPa and 20 MPa (see equation A20). As Fig. 2-20 shows, the retention curves used all fall well within the range of available experimental results.
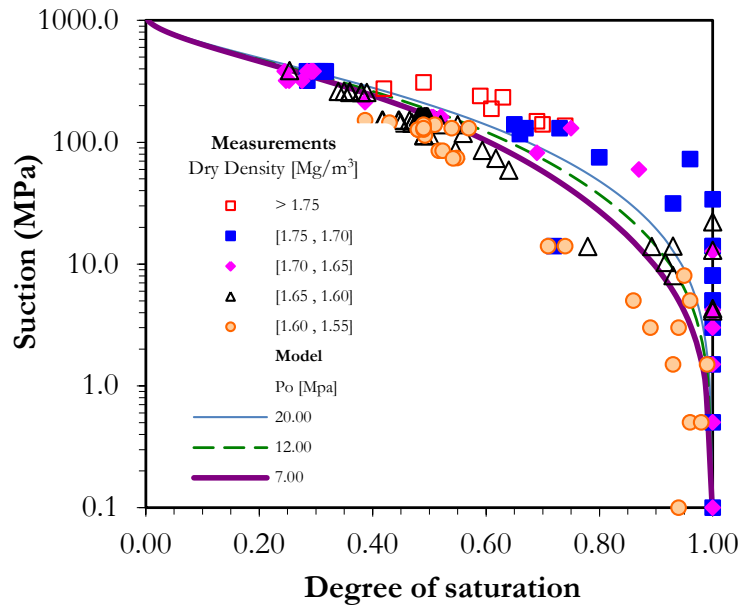
Fig. 2-20:   Range of retention curves used in the sensitivity analysis.

The predictions of distributions of water content and dry density for Section F2 for the second dismantling are presented in Fig. 2-21 and 2-22, respectively. The retention curve used in each case is identified by the value of the parameter P_0. For qualitative comparison, the same figures show the dismantling observations of the equivalent section of Heater #1 (dismantling Section 37). It can be observed that, in all cases, the agreement with the observations after five years of heating could be considered satisfactory. It is noted here that the data from the second dismantling may indicate somewhat reduced water contents due to the longer period of heating. The predictions of the same analyses for Section G are shown in Fig. 2-23 and 2-24.
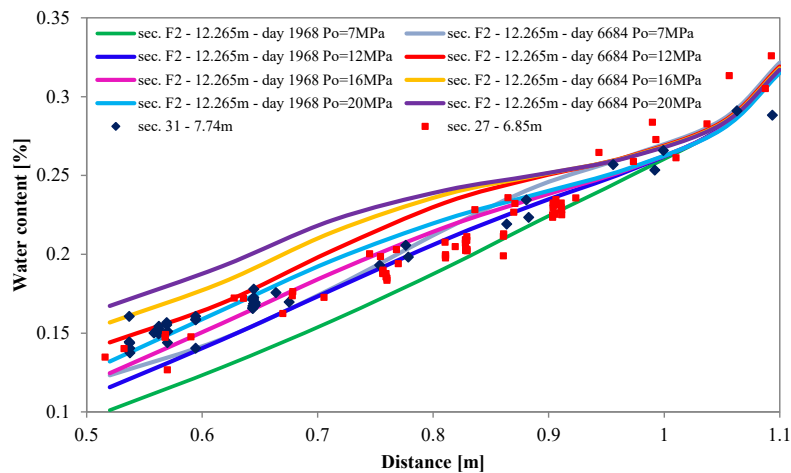
Fig. 2-21:   Predicted values of water content distributions for the different water retention curves adopted in the analyses (Section F2).
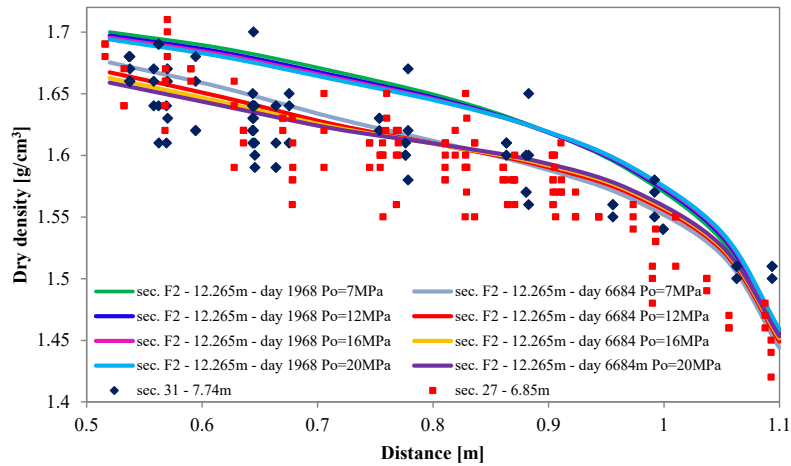
Fig. 2-22: Predicted values of dry density distributions for the different water retention curves adopted in the analyses (Section F2).
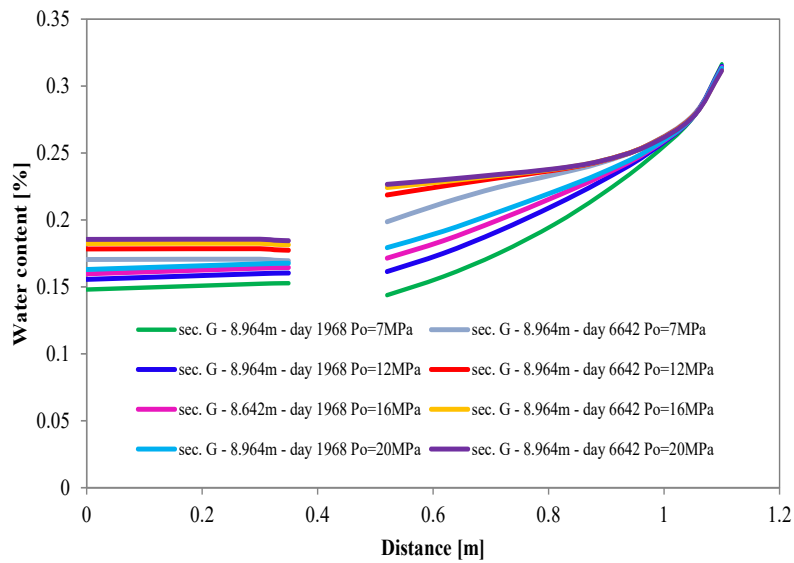
Fig. 2-23: Predicted values of water content distributions for the different water retention curves adopted in the analyses (Section G).
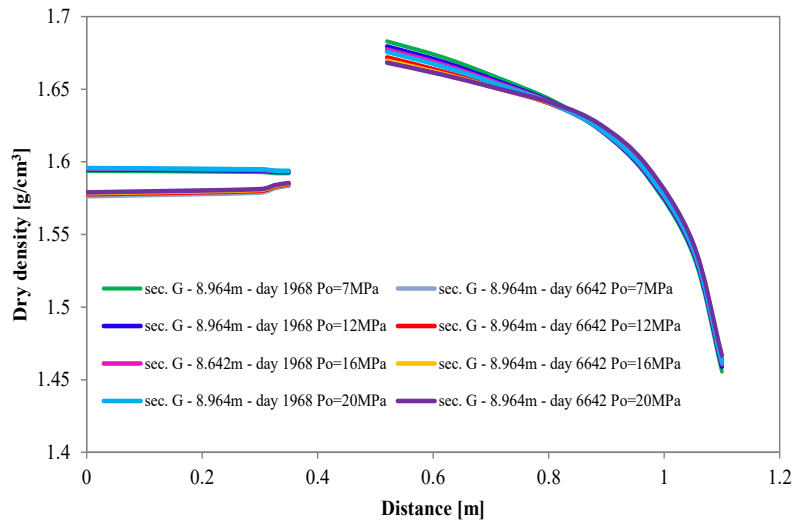
Fig. 2-24: Predicted values of dry density distributions for the different water retention curves adopted in the analyses (Section G).

2.5.4 Consequences for the early repository evolution viewpoint

The modelling analysis performed with the OCB model for the FEBEX in-situ experiment does not indicate any processes or factors that would prevent the extrapolation of the main modelling results over longer timescales.

With respect to the hydraulic processes, the long-term analysis will tend towards a full saturation of the barrier over a time depending mainly on the evolving hydraulic conductivity of the bentonite. A decrease of temperature (not contemplated in the performance of the experiment) would also lead to an enhanced hydration progress.

The prediction of the long-term evolution of the dry density throughout the barrier is more nuanced as it depends strongly on the specific features of the mechanical constitutive model adopted for the analysis. The type of mechanical model used here will tend to predict that the higher densities of the bentonite will be localized near the canister, whereas lower densities occur in zones close to the hydration front. This is because the adopted model for the elastic bulk modulus (K, Eq. 2-10) includes a direct dependence of the K on stress level (i.e. which is established in terms of mean average stress p). This implies that as the swelling pressure increases with the hydration of the barrier, the material becomes stiffer and less deformable. Therefore, the distribution of dry densities formed at the earliest stages of the experiment, with the higher values of density near the canister and the lower values near the rock (i.e. see Fig. 2-10a, 2-11a, and 2-12a), will tend to persist in the long-term. The observations of the distribution of dry density in the barrier after the second dismantling will thus provide key information concerning the mechanical constitutive model for the bentonite, and support potential modifications.

3   THM modelling by EPFL

This chapter describes the modelling analyses performed by EPFL. Section 3.1 provides the description of the THM coupling framework and constitutive laws used. Section 3.2 gives a short overview of the history of the development of the FEBEX model. Section 3.3 provides the initial and boundary conditions, as well as input parameters used in the simulations. Section 3.4 discusses the model outcomes in the following steps:

- Ventilation process results

- Temperature evolution results

- Relative humidity results

- Impact of heater switch-off

An interpretation of the results is provided in Section 3.5., and conclusions are given in Section 3.6.

3.1   Description of the model and underlying assumptions

3.1.1   THM coupling framework

Equilibrium and balance equations

Buffer and host rock materials are modelled as porous media. To describe the diffusive processes in such media, the theory of mixtures (Bowen 1982) is used. The porous media is assumed to be composed of a solid matrix and voids filled with liquid and gas phases. The liquid phase contains two species: liquid water and dissolved air, while the gas phase is composed of dry air and water vapour. The equilibrium between liquid water and water vapour is controlled by temperature. To uniquely describe the state of the material, four primary state variables are required: gas pressure p_g, water pressure p_w, temperature T, and the displacement vector $\boldsymbol{u}$. The intrinsic solid phase component is assumed to be incompressible (incompressible grains) while the water phase is slightly compressible. The solid, liquid, and water phases are assumed in thermal equilibrium, and a unique temperature is defined for the whole medium. This assumption is justified by the relatively slow kinematics of the governing processes which allow a continuous thermal equilibrium between phases.

Moreover, the compositional approach (Panday & Corapcioglu 1989; Collin et al. 2002) is adopted to write the mass balance equations, meaning that the mass balances are described for the species rather than for the phases. Therefore, the conservation of mass of each chemical species (water and air) is assumed. Using this approach, the phase exchange terms will cancel in the balance equations. In the following equations, the subscripts l, g, w, da, a, and v are related to the liquid phase, the gas phase, the liquid water, the dissolved air in water, the dry air, and the water vapour, respectively. An extended description of the governing equations can be found in [Collin et al. 2002, 2006; Collin 2003].

The equilibrium and balance equations, as well as the water and heat flows, are expressed in the moving current configuration through a Lagrangian actualised formulation (Charlier 1987). According to these assumptions, the mass balance equation of the solid skeleton is necessarily met. For a given mixture volume V, the mass balance equation reads (Collin et al. 2006):

$$\frac{\partial \rho_s (1-n) V}{\partial t} = 0$$

(3-1)

Where ρ_s is the density of solid grains, n the soil porosity, and t the time.

The mass conservation equations for the water and gas species are, respectively:

$$\underbrace{\frac{\partial}{\partial t}\left(\rho_w n S_r\right) + div\left(\rho_w \mathbf{f_l}\right) - Q_w}_{\text{Liquid water}} + \underbrace{\frac{\partial}{\partial t}\left(\rho_v n \left(1 - S_r\right)\right) + div\left(\mathbf{i_v} + \rho_v \mathbf{f_g}\right) - Q_v}_{\text{Water vapour}} = 0$$

(3-2)

$$\underbrace{\frac{\partial}{\partial t}\left(\rho_a n \left(1 - S_r\right)\right) + div\left(\rho_a \mathbf{f_g} + \mathbf{i_a}\right) - Q_a}_{\text{Dry air in gas phase}} + \underbrace{\frac{\partial}{\partial t}\left(\rho_a H_s n S_r\right) + div\left(\rho_a H_s \mathbf{f_l}\right) - Q_{da}}_{\text{Dissolved air in water}} = 0$$

(3-3)

where ρ_w, ρ_v, and ρ_a are the bulk density of liquid water, water vapour, and dry air. $\mathbf{f_l}$ and $\mathbf{f_g}$ are the macroscopic velocity of the liquid and gas phases, respectively. $\mathbf{i_v}$ and $\mathbf{i_a}$ are the non-advective flux of water vapour and dry air. S_r is the degree of saturation. Henry's coefficient, H_s, defining the proportion of dissolved air in the liquid phase, is taken equal to 0.017. Q_w, Q_v, Q_a, and Q_{da} are volume sources of liquid water, water vapour, dry air, and dissolved air in water, respectively.

The energy balance equation of the mixture has the following form:

$$\underbrace{\frac{\partial S_T}{\partial t} + L \frac{\partial}{\partial t}\left(\rho_v n \left(1 - S_r\right)\right)}_{\text{Heat storage}} + \underbrace{div\left(\mathbf{f_T}\right) + L \frac{\partial}{\partial t}\left(\mathbf{i_v} + \rho_v \mathbf{f_g}\right)}_{\text{Heat transfer}} - Q_T = 0$$

(3-4)

where $\mathbf{f_T}$ is the heat flow and Q_T is a volume heat source. L is the latent heat of water vaporisation. The enthalpy of the system S_T is given by:

$$S_T = \rho C_p (T - T_0)$$

(3-5)

Where ρ and C_p are the density and the specific heat of the mixture (solid matrix with voids filled by gas and liquid), respectively. Those parameters are deduced from the properties of each phase:

$$\rho C_p = n S_r \rho_w c_{p,w} + (1-n) \rho_s c_{p,s} + n (1 - S_r) \rho_a c_{p,a} + n (1 - S_r) \rho_v c_{p,v}$$

(3-6)

Where ρ_s is the soil grain bulk density and $c_{p,w}$, $c_{p,s}$, $c_{p,a}$, and $c_{p,v}$ are the specific heat of liquid water, solid, dry air, and water vapour respectively.

The soil equilibrium equation is given by:

$$div(\boldsymbol{\sigma}) + \mathbf{b} = 0$$

(3-7)

where $\boldsymbol{\sigma}$ is the total (Cauchy) stress tensor, with compressive stress taken as positive, and $\mathbf{b}$ is the body force vector which is equal to $\rho\mathbf{g}$ as the only body force is gravity.

Constitutive relations

The conservation equations which govern the THM equilibrium of the system (Eqs. 3-1 to 3-7) are expressed in terms of the primary state variables ($\mathbf{u}$, p_w, p_g, and T), after introduction of the following constitutive relationships. The liquid water bulk density depends on the pore water pressure p_w and temperature T through the water bulk modulus χ_w and the volumetric water thermal expansion coefficient β_w':

$$\rho_w = \rho_{w0}\left(1 + \frac{p_w - p_{w0}}{\chi_w} - \beta_w'\left(T - T_0\right)\right)$$

(3-8)

Where ρ_{w0}, p_{w0}, and T_0 are the initial values of water bulk density, pore water pressure, and temperature, respectively. The bulk density of the water vapour is determined through the following equation:

$$\rho_v = \exp\left(\frac{\left(p_w - p_g\right)M_v}{R\,T\rho_w}\right)\frac{p_{v,0}M_v}{R\,T}$$

(3-9)

where p_w and p_g are the liquid water and gas pressures, respectively, M_v is the vapour molar mass (= 0.018 kg/mol), T is temperature expressed in Kelvin, and $p_{v,0}$ is the saturated vapour pressure given by an experimental expression depending on temperature (Charlier 1987; Nuth & Laloui 2008):

$$p_{v,0} = a\exp\left(-b/T\right)$$

(3-10)

With a = 112'659 MPa and b = 5'192.74 K for the temperature range between 273 K and 373 K.

The bulk density of dry air can be deduced considering that the gas phase is an ideal gas to which the Dalton law can be applied:

$$p_g = p_a + p_v$$

(3-11)

Consequently, the bulk density of dry air is:

$$\rho_a = \frac{p_a M_a}{R\,T} = \frac{\left(p_g - p_v\right)M_a}{R\,T} = \frac{p_g M_a}{R\,T} - \frac{\rho_v M_a}{M_v}$$

(3-12)

where M_a is the dry air molar mass (= 28.8×10^{-3} kg/mol).

The liquid phase motion is governed by the Darcy's law:

$$\mathbf{f_l} = -\frac{\mathbf{k_w}}{\mu_w}\left(\mathbf{grad}\left(p_w\right) + g\rho_w\mathbf{grad}\left(y\right)\right)$$

(3-13)

where $\mathbf{k_w}$ is the tensor of intrinsic water permeability, g the gravity acceleration, y the vertical, upward directed coordinate, and μ_w the dynamic viscosity of the water. The water permeability, assumed isotropic ($\mathbf{k_w} = k_w\mathbf{I}$, $\mathbf{I}$ being the identity matrix), depends on the degree of saturation S_r according to the following equation:

$$k_w = k_{w,sat}S_r^{CKW1}$$

(3-14)

where $CKW1$ is a material parameter. $k_{w,sat}$ saturated permeability which depends on the soil porosity n through the Kozeni-Carman relation:

$$k_{w,sat} = k_{w0,sat}\frac{n^{EXPN}}{\left(1-n\right)^{EXPM}}\frac{\left(1-n_0\right)^{EXPM}}{n_0^{EXPN}}$$

(3-15)

where $k_{w0,sat}$ is the saturated water permeability corresponding to the reference porosity n_0 and $EXPN$ and $EXPM$ are material parameters of the Kozeny-Carman relation.

The dynamic viscosity of the water is assumed dependent on the temperature with the following form:

$$\mu_w = 0.6612\left(T - 229\right)^{-1.562}$$

(3-16)

In Eq. 3-13, it is assumed that the ρ_w, $\mathbf{k_w}$, and μ_w are unaffected by the amount of dissolved air in the liquid phase.

The gas phase velocity is governed by the generalized Darcy's law for a multiphase medium:

$$\mathbf{f_g} = -\frac{\mathbf{k_g}}{\mu_g}\left(\mathbf{grad}\left(p_g\right) + g\rho_g\mathbf{grad}\left(y\right)\right)$$

(3-17)

where $\mathbf{k_g}$ is the tensor of intrinsic gas permeability, and μ_g is the dynamic viscosity of the gas. This last parameter is assumed to be linearly dependent on the temperature:

$$\mu_g = \mu_{g0}\left(1 - \alpha_{g,T}\left(T - T_0\right)\right)$$

(3-18)

where μ_{g0} is the dynamic viscosity of the gas at initial temperature T_0 and $\alpha_{g,T}$ is a material parameter.

The velocity of water vapour diffusion is related to the air bulk density gradient:

$$\mathbf{i_v} = n\left(1 - S_r\right)\tau D \rho_g \mathbf{grad}\left(\frac{\rho_a}{\rho_g}\right)$$

(3-19)

where D is the air diffusion coefficient expressed according to the work of Philip & De Vries (1957):

$$D = 5.893 \; 10^{-6} \frac{T^{2.3}}{p_g}$$

(3-20)

where D, T, and p_g are expressed in m²/s, Kelvin, and Pascal, respectively. τ is the tortuosity of the material.

The heat transport is governed by conduction and convection:

$$\mathbf{f_T} = -\Gamma \, \mathbf{grad}\left(T\right) + c_{p,w}\rho_w \mathbf{f_w} + c_{p,a}\left(\mathbf{i_a} + \rho_a \mathbf{f_g}\right) + c_{p,v}\left(\mathbf{i_v} + \rho_v \mathbf{f_g}\right)$$

(3-21)

where Γ is the thermal conductivity of the mixture as deduced from the thermal conductivity of each phase:

$$\Gamma = \lambda_s\left(1 - n\right) + \lambda_w nS_r + \lambda_g n\left(1 - S_r\right)$$

(3-22)

where λ_s, λ_w, and λ_a are the thermal conductivity of solid, liquid water, and gas phase, respectively. Notice that, since the current configuration is defined following the skeleton movement, the thermal convection effect is implicitly taken into account.

The behaviour of the solid matrix is assumed to be governed by the generalized effective stress tensor $\boldsymbol{\sigma}'$ through combinations of mechanical stresses and fluid pressures (Nuth & Laloui 2008):

$$\boldsymbol{\sigma}' = \boldsymbol{\sigma} - p_g \mathbf{I} + S_r\left(p_g - p_w\right)\mathbf{I}$$

(3-23)

In this Lagrangian approach, the Cauchy strain tensor is used:

$$\varepsilon = \frac{1}{2}\left(\mathbf{L} - \mathbf{L^T}\right)$$

(3-24)

where $\mathbf{L} = \dfrac{\partial \mathbf{u}}{\partial \mathbf{X}}$ is the displacement ($\mathbf{u}$) gradient defined in the global axis ($\mathbf{X}$) in the moving current configuration. This strain tensor is related to the generalized effective stress tensor through the mechanical constitutive model:

$$d\boldsymbol{\sigma}' = \mathbf{C} : d\boldsymbol{\varepsilon}$$

(3-25)

where **C** is the mechanical constitutive tensor. This last equation is written in an incremental form due to the non-linear behaviour of the solid matrix. The above presented THM coupling framework is the one implemented in the FEM software Lagamine (Collin et al. 2002; Charlier 1987) which has been used in this work.

3.1.2   ACMEG-TS model

Mechanical constitutive model

The constitutive model, called ACMEG-TS, is based on an elasto-plastic framework, which is used to capture the main mechanical behaviour of the buffer (François & Laloui 2008). The total strain increment $d\varepsilon$ being decomposed into elastic, $d\varepsilon^e$, and plastic, $d\varepsilon^p$, components. The elastic part of the deformation is expressed as follows:

$$d\mathbf{\varepsilon^e} = \mathbf{E}^{-1}d\mathbf{\sigma}' - \mathbf{\beta_T}dT$$

(3-26)

The first term of Eq. (3-26) is the contribution of the effective stress increment $d\mathbf{\sigma}'$ to the total elastic strain increment, through the elastic tensor **E**. According to Eq. 3-23, this part may follow from total stress or fluid pressure variations. The second term of Eq. 3-26 is related to the thermo-elastic strain of the material, through the thermal expansion coefficient matrix, $\mathbf{\beta_T} = (1/3)\beta'_s\,\mathbf{I}$.

The plastic mechanism of the material is induced by two coupled hardening processes: an isotropic and a deviatoric one. Using the concept of multi-mechanism plasticity, both mechanisms may induce volumetric plastic strain. Therefore, the total volumetric plastic strain rate $d\varepsilon^p_v$ is the coupling variable linking the two hardening processes. The yield functions of the two mechanical, thermo-plastic mechanisms have the following expressions (Fig. 3-1):

$$f_{iso} = p' - p'_c\,r_{iso} \quad ; \quad f_{dev} = q - Mp'\left(1 - b\,\ln\frac{d\,p'}{p'_c}\right)r_{dev} = 0$$

(3-27)

where p'_c is the pre-consolidation pressure. b, d and M are material parameters. p'_c depends on temperature T and suction s in addition to the volumetric plastic strain, ε^p_v .

$$p'_c = \begin{cases} p'_{c0}\exp\left(\beta\,\varepsilon^p_v\right)\left\{1 - \gamma_T\,\log\left[T/T_0\right]\right\} & \text{if } s \le s_e \\ p'_{c0}\exp\left(\beta\,\varepsilon^p_v\right)\left\{1 - \gamma_T\,\log\left[T/T_0\right]\right\}\left\{1 + \gamma_s\,\log\left[s/s_e\right]\right\} & \text{if } s \ge s_e \end{cases}$$

(3-28)

where p'_{c0} is the initial pre-consolidation pressure at ambient temperature T_0 and for suction lower than the air-entry value s_e. β is the plastic compressibility modulus and γ_T and γ_s are material parameters.

r_{iso} and r_{dev} are the degree of mobilization of the isotropic and the deviatoric mechanisms and are hyperbolic functions of the plastic strain induced by the isotropic and the deviatoric mechanisms, respectively. This enables a progressive evolution of the yield limit during loading and a partial comeback of this limit during unloading.
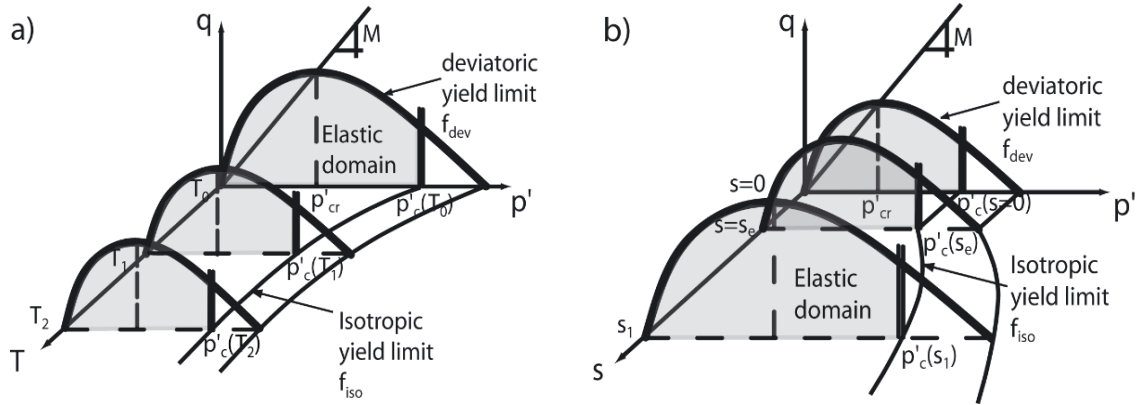
Fig. 3-1:   Effect of (a) temperature and (b) suction on the shape of coupled mechanical yield limits.

The flow rule of the isotropic mechanism is associated, while it is not associated for the deviatoric mechanism. The following expressions are assumed:

$$d\boldsymbol{\varepsilon}^{\mathrm{p,iso}} = \frac{\lambda_{iso}^{p}}{3}\mathbf{I}$$
(3-29)

$$d\boldsymbol{\varepsilon}^{\mathrm{p,dev}} = \lambda_{dev}^{p}\frac{1}{Mp'}\left[\frac{\partial q}{\partial \boldsymbol{\sigma}'} + \alpha\left(M - \frac{q}{p'}\right)\frac{1}{3}\mathbf{I}\right]$$
(3-30)

The plastic multipliers, λ_{iso}^{p} and λ_{dev}^{p}, are determined using Prager's consistency equation (Prager 1949) for multi-dissipative plasticity [11, 12]. α is a material parameter.

Water retention constitutive model

Hysteresis in water retention behaviour is modelled as a plastic process. As long as the soil is drying, suction increases and the degree of saturation, S_r, tends to decrease after the air-entry suction s_e is reached. Under re-wetting, a hysteretic phenomenon occurs, also represented by a yielding process (Fig. 3-2). A wetting-drying cycle activates two successive yield limits in the $(S_r - s)$ plane (f_{dry} and f_{wet}, along the drying and wetting paths, respectively):

$$f_{dry} = s - s_d = 0 \qquad ; \qquad f_{wet} = s_d s_{hys} - s = 0$$
(3-31)

where s_d is the drying yield limit and s_{hys} a material parameter considering the size of the water retention hysteresis. Because air-entry suction of the materials depends on temperature and dry density, in the general form of the model, s_d is a function of temperature T and volumetric strain, ε_v:

$$s_d = s_{d0}\left\{1 - \theta_T \log\left[T/T_0\right] - \theta_e \log\left[1 - \varepsilon_v\right]\right\}$$
(3-32)

where θ_T and θ_e are material parameters describing the evolution of air-entry suction with respect to temperature and volumetric strain, respectively. If the initial state is saturated, the initial drying limit s_{d0} is equal to air-entry suction s_e and increases when suction overtakes s_e as follows:

$$s_d = s_d \exp\left(-\beta_h \, \Delta S_r\right)$$

(3-33)

where β_h is the slope of the desaturation curve in the $\left(S_r - \ln s\right)$ plane (Fig. 2). The evolution of s_d with respect to T and ε_v is described by Eq. (3-32).
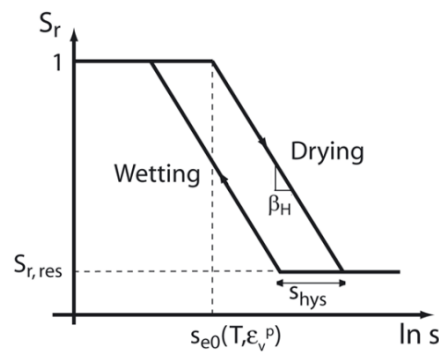
Fig. 3-2:   Schematic representation of water retention curve modelling

3.2   History of the development of the FEBEX model

LMS/EPFL has been involved for in the previous simulations and predictions of the FEBEX in-situ experiment, mainly focusing on the FEBEX, FEBEX Ⅱ and FEBEXe phases. The results of the LMS/EPFL work were presented in the following publications:

- Dupray, F., François, B. & Laloui, L.: Analysis of the FEBEX multi-barrier system including thermo-plasticity of unsaturated bentonite. International Journal for Numerical and Analytical Methods in Geomechanics, 2013a. 37:399-422.

- Dupray, F., Lamure, E. & Laloui, L.: Study of the second phase of the real-scale in-situ test FEBEXe. Technical report EPFL – Nagra project 9499, 2013b.

Dupray et al. (2013a) presented simulation results for the first phase of FEBEX as well as the comparison of numerical results with monitoring data; this work has proven the high quality of the LMS/EPFL modelling framework to capture the THM coupling process during the test. Dupray et al. (2013b) presented the FEBEX Ⅱ simulation results, including two final scenarios: continued heating and stopped heating.

For the work presented in this report, all the simulations were run from the beginning of the FEBEX in-situ experiment, including the excavation of the gallery and the ventilation phase.

3.3   The initial and boundary conditions, input parameters

3.3.1   Model geometry and boundary conditions

In order to avoid the undesired effects of the imposed boundary conditions, the distance of the external boundary to the engineered barrier is the same (60 m) in both the axial and radial directions. The imposed boundary conditions are illustrated in Fig. 3-3. The perpendicular displacements of boundaries are prevented, except for the gallery surface boundary of service tunnel which is assumed to be deformable during the whole simulation. The temperature and water pressures at the boundaries are fixed equal to the values measured in situ. The air pressure has been fixed equal to the atmospheric pressure over the entire domain.
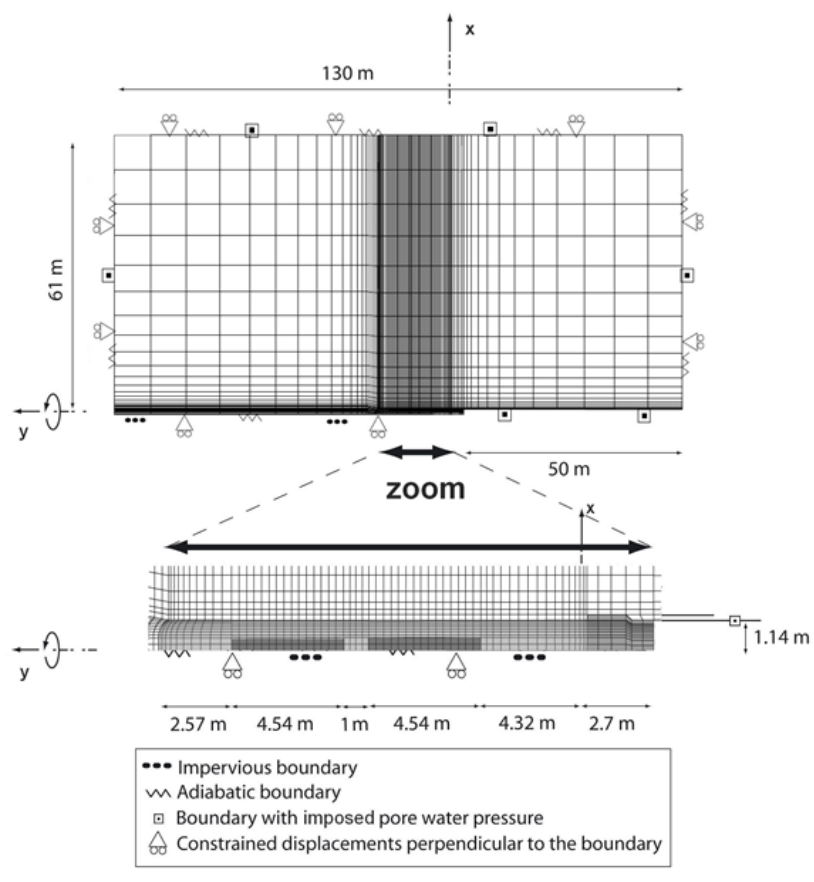
Fig. 3-3:   Finite element mesh used in the simulation of the in-situ FEBEX experiment.

The y axis is the axis of symmetry of revolution.

3.3.2   Simulated phases and initial conditions

The various phases considered in the simulations are: the excavation of the gallery, the ventilation phase, the initial heating phase, the constant temperature of the heater phase, the cooling processes and the dismantling phases. The corresponding time scale for each phase is summarized in Tab. 3-1.

Since the simulations also include the excavation and ventilation phases, the initial conditions refer to the original domain before the experiment was initiated. Based on the monitoring data in situ, the total stress at the depth of the test drift is about 28 MPa, and the water pressure is about 0.7 MPa (Dupray et al. 2013b). The test is modelled as an axisymmetric problem and gravity is not considered. An initial isotropic total stress of 28 MPa was assumed for the granite domain. The initial water pressure is also assumed to be uniform with a value of 0.7 MPa. The initial temperature is equal to 12 °C in the entire modelled domain.

The excavation process is simulated by releasing the radial stress along the drift from the initial value of 28 MPa to 0 MPa during the first 35 days. The ventilation process is simulated by setting the water pressure of the drift surface from the initial value of 0.7 MPa to atmospheric pressure for 385 days. During those processes, the bentonite, canisters and plug elements are not included in the mesh and virtual material elements with a small Young's modulus are used. The Engineering Barriers System (EBS) construction, canister installation and plug construction are modelled by activating the bentonite, canister and plug elements at day 385 to replace the virtual material elements. In the bentonite, suction of 114 MPa is considered as the initial hydraulic condition. The external total stress is initially equal to zero at the beginning of activating bentonite elements. Since there are also 135 days between the end of EBS construction and the beginning of the heating process, the water would flow into the buffer system from the granite during this period.

The temperature ramp in the experiment was imposed with a controlled power (1200 W per heater for 20 days and 2000 W per heater over the following 33 days until reaching the desired temperature of 100 °C). The same scheme has been reproduced in the simulation. The thermal losses due to the presence of air in the construction gaps (which are located mainly inside the liner containing the heaters and at the boundary between bentonite and granite) could be estimated at 15 %. Therefore, the power applied in the simulation is 85 % of the real power, with the same ramp and the centre of the heaters reaches 100 °C at the same time of the experiment. After the temperature of the heater centre reached 100 °C, the temperature on all heater nodes (both Heater #1 and #2) is then kept constant; this allows maintaining the small variations in heater temperature between the corners and centre. After 1'826 days of heating, the power of Heater #1 was switched off. To simulate this process, the temperature of all Heater #1 elements is no longer controlled. The dismantling process is simulated by shutting off the plug elements, bentonite elements and canister elements following the same sequence of the dismantling plan, while simultaneously activating virtual material elements with a very small Young's modulus to replace them. The initial external stress of the virtual material elements is zero, thus leading to an unloading of the EBS elements. The second plug construction is simulated by replacing the virtual material elements with concrete plug elements. The initial water pressure in the second plug is assumed to be at the atmospheric pressure. After 7127 days of heating, Heater #2 is switched off in the simulation: the temperature on the entire Heater #2 is set free without input heating power. The sequence used in the second dismantling is the same as the one used in the first dismantling phase. The simulation stops after day 7235.

Tab. 3-1:   The processes included in FEBEX in-situ test

Start time	Activities	Duration (days)	Total time (days)	Heating duration (days)	Problem analyses
25.09.1995	TBM excavation of FEBEX tunnel Excavation lasts 35days	278	278	-	HM
01.07.1996	Engineered barrier system construction	107	385	-	HM
15.10.1996	End of EBS construction	135	520	-	HM
28.02.1997	Heating 1'200W lasts 20 days 2'000W lasts 33 days Constant T from 21.04.1997, taking 8 days in three steps: 95-99-100 °C	1'826	2'346	1'826	THM
28.02.2002	Switch off Heater #1	33	2'379	1'859	THM
02.04.2002	First dismantling Concrete plug part, finished on 28.05.2002 Extraction of Heater #1 on 19.06.2002 Shotcrete plug on 23. – 24.07.2002 Second part on 23. – 27.06.2003	116	2'495	1'975	THM
26.07.2002	End of first dismantling	4'632	7'127	6'607	THM
01.04.2015	Switch off Heater #2	6	7'133	-	THM
07.04.2015	Second dismantling	102	7'235	-	THM

3.3.3   Calibration of model parameters

3.3.3.1   FEBEX bentonite

The buffer system was constructed with FEBEX bentonite blocks, which were compacted to a dry density of 1.7 g/cm^3. Taking into account the construction gaps between blocks, between buffer and rock, and between buffer and liner/canister, the average dry density is 1.6 g/cm^3. For a dry density of 1.6 g/cm^3, the swelling pressure is of the order of 5 MPa. However, the swelling pressure increases to reach about 10 MPa for the dry density of 1.7 g/cm^3. Thus, it can be predicted that the maximum swelling pressure for the in-situ test should be in the range of 5 MPa to 10 MPa. The initial water content of blocks is between 12.5 % and 15.5 %. The THM properties of the FEBEX bentonite have been extensively investigated over last two decades. Moreover, their mechanical response under non-isothermal and unsaturated conditions has been characterized by different experimental programs during the FEBEX project (Enresa 2000, 2004).

Each constitutive relationship is calibrated to specific laboratory tests. Fig. 3-4 shows the laboratory test paths of mechanical compression tests at different suction levels, which were used to calibrate the ACMEG-TS model (Enresa 2004). The test paths of the conventional tri-axial compression in saturated conditions are used to calibrate the deviatoric parameters. The isotropic plastic parameters are fixed from the isotropic compression test in saturated condition. The parameters related to effect of suction on the pre-consolidation stress are calibrated by determining the slope of the logarithmic increase of the pre-consolidation pressure with suction levels. The material parameters used in this numerical modelling are listed in Tab. 3-2.
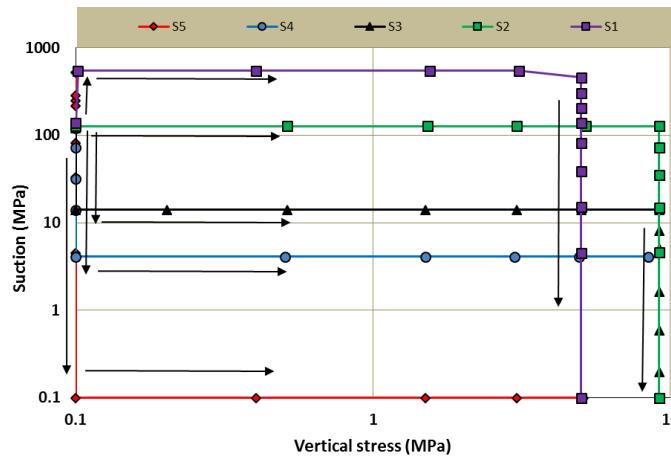
Fig. 3-4:   Generalized stress path for the tests.

           Data taken from [16].

Tab. 3-2:   Set of FEBEX bentonite parameters for ACMEG-TS model.

Elastic parameters		
K_{ref} , G_{ref} , n^e , β'_s	[MPa], [MPa], [-], [°C^{-1}]	19.5, 9.1, 0.75, 2.1 × 10^{-4}
Isotropic plastic parameters		
β_m , γ_s , γ_T , r^e_{iso} , p'_c , Ω	[-], [-], [-], [-], [-], [MPa] , [-]	27.0, 10, 0.2, 0.7, 60, 10^{-6}
Deviatoric plastic parameters		
b , d , M , g , α , a , r^e_{dev}	[-], [-], [°], [-], [-], [-], [-]	1, 2.0, 1.2, 0, 1, 0.001, 0.8
Water retention parameters		
s_{e0} , β_h , θ_T , θ_e , s_{hys}	[MPa], [-], [-], [-], [-]	4, 6.33, 0, 0, 0.9

Fig. 3-5 presents the comparison between the simulation and tests results. Note that the effective stress is computed based on Eq. 3-23. A good agreement with test results is observed, confirming that the ACMEG-TS model can capture the main swelling deformation behaviour of the bentonite. The deviation for the test with a suction of 500 MPa, can be explained by assuming that the stress framework adopted by ACMEG-TS may have some limitations for these suction values (François & Laloui 2008).

The thermo-mechanical parameters have been calibrated by Dupray et al. (2013a) to the laboratory test on thermal expansion of FEBEX bentonite, and the results are presented in Fig. 3-6.

The calibration of the water retention constitutive model is carried out by fitting the water retention model to the laboratory data presented in Fig. 3-7. The corresponding parameters are summarized in Tab. 3-2.

The intrinsic permeability depends on the porosity. This relationship is well captured by Eq. 3 14. The calibration of this relationship for FEBEX bentonite is presented in Fig. 3-8. The corresponding parameters are EXPM = 5.3, EXPN = 5.5. The intrinsic water permeability is 5E-21 m^2 for a dry density of 1.6 g/cm^3.

The thermal conductivity is calculated based on Eq. 3-22, and the calibration results are shown in Fig. 3-9. The corresponding parameters are summarized in Tab. 3-3.

a)

b)

c)

d)
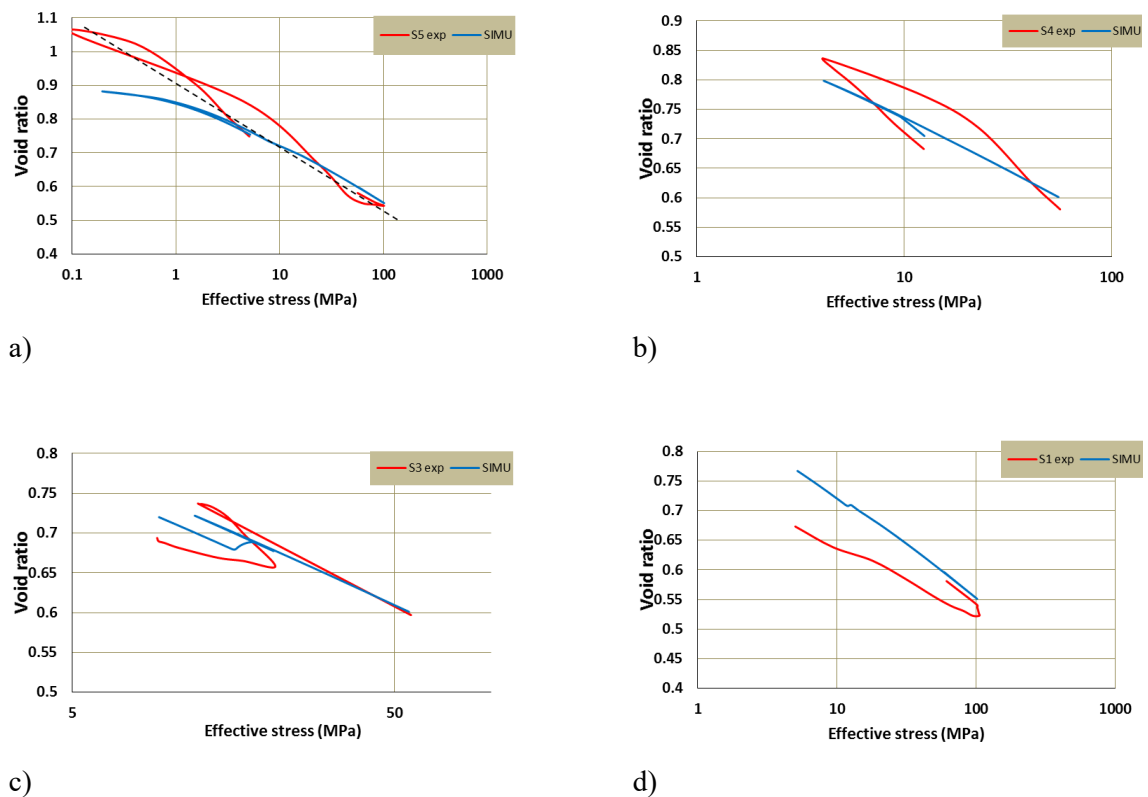
Fig. 3-5:   Comparison between simulation results and test data.

            Data taken from Enresa (2004).
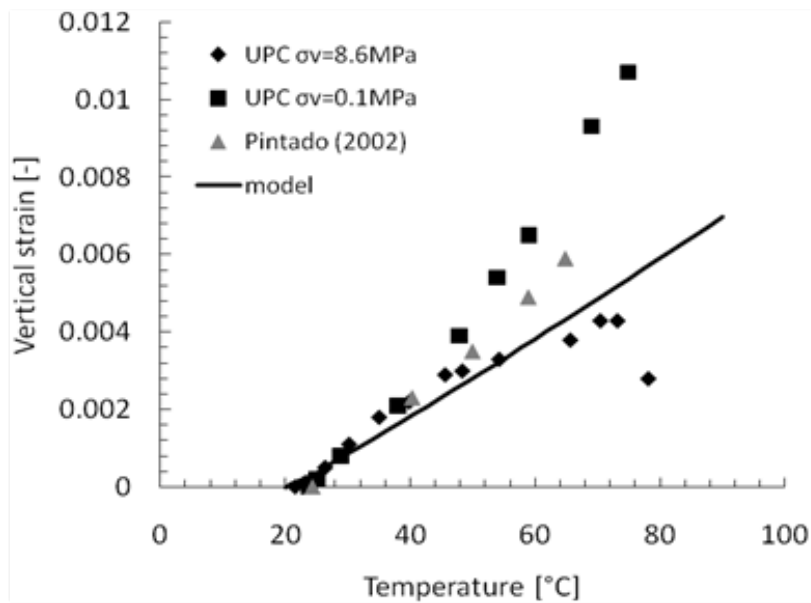
Fig. 3-6:   Thermally-induced strains in oedometric conditions.

Experimental data taken from Romero et al. (2005) and Pintado et al. (2002).
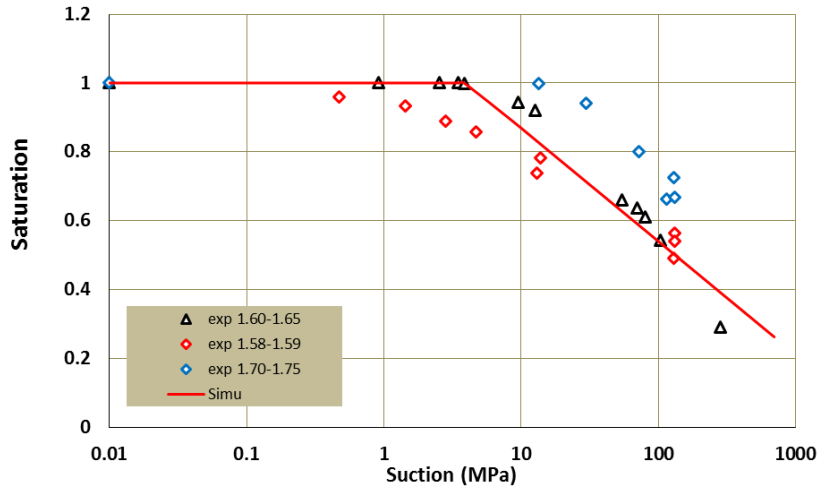
Fig. 3-7:   Numerical simulation of retention curves of FEBEX bentonite and comparison with experiments.

Data taken from Enresa (2004).
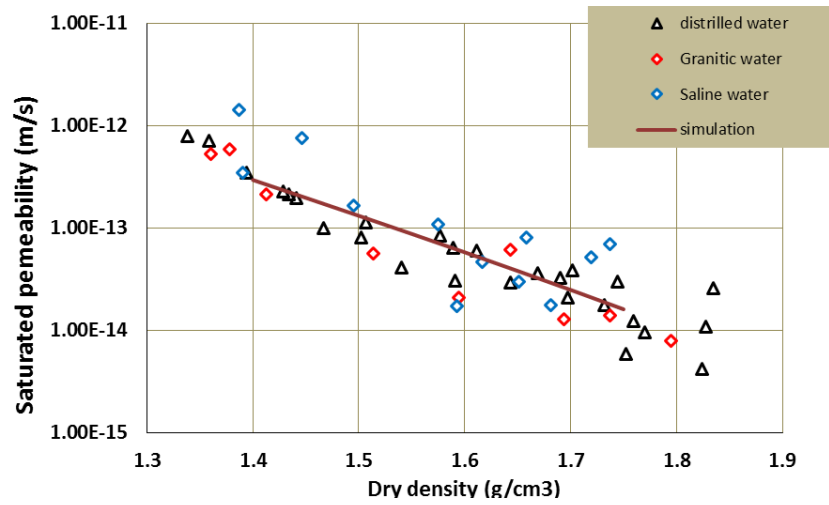
Fig. 3-8:   Calibration of Kozeny-Carman relationship for FEBEX bentonite.
Data taken from Enresa (2004).
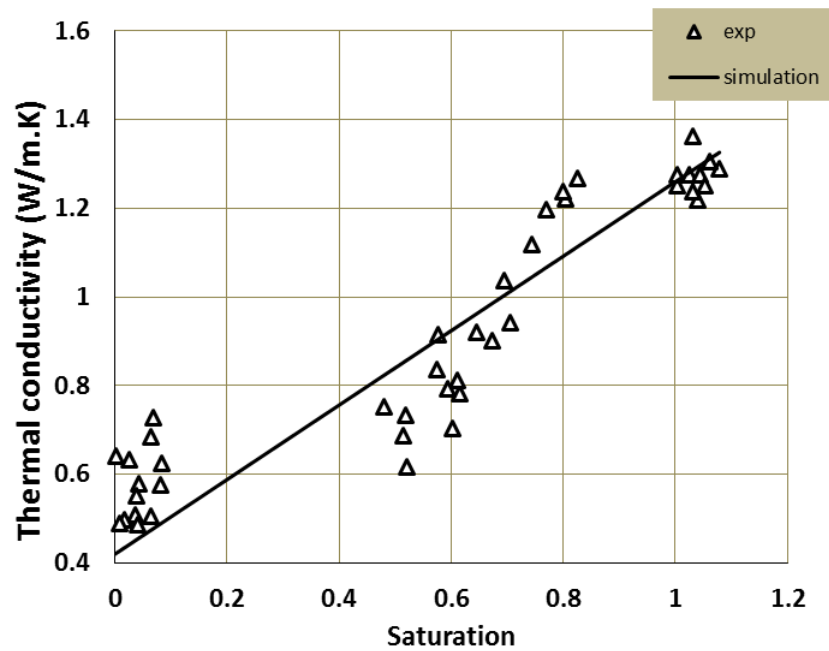
Fig. 3-9:   Calibration of saturation effects on thermal conductivity for FEBEX bentonite.
Data taken from Enresa (2004).

3.3.3.2   Host rock

Based on the previous work and experimental results, the air entry value of the rock may in fact be fairly high (up to 500 MPa) (Gens et al. 1998). In the simulations presented in this chapter, the granite is assumed to be fully saturated even under negative pore water pressure. For this, the option of a high air-entry value has been chosen. The stress-strain behaviour of granite is modelled with an elastic model. The mechanical, thermal and hydraulic parameters of the granite are given in Tab. 3-3.

3.3.3.3   Other materials

The parameters of the steel of the heaters, as well as the concrete of the plug, have been set in the range of usual parameters for those kinds of materials. Their mechanical behaviour has been assumed to be linear elastic. The steel is considered as impervious and the concrete plug as fully saturated. All these parameters are summarized in Tab. 3-3.

3.4   Model outcomes

To present the simulation results, different sections' results are reported. Those sections are selected based on instrumented sections in the field test. The instrumented bentonite sections at different experimental stages are shown in Fig. 3-10. For all following graphs, zero time corresponds to the start of the heating.

Tab. 3-3: Parameters of the various materials involved in the simulation of the FEBEX experiment.

Thermal parameters			Bentonite	Granite	Concrete	Canister
Solid thermal conductivity	λ_s	[W/(m.°C)]	0.7	-	-	-
Water thermal conductivity	λ_w	[W/(m.°C)]	2.1	-	-	-
Air thermal conductivity	λ_a	[W/(m.°C)]	0	-	-	-
Global thermal conductivity	Γ	[W/(m.°C)]	-	3.34	1.7	-
Solid heat capacity	$c_{p,s}$	[J/(kg.°C)]	1091	-	-	-
Water heat capacity	$c_{p,w}$	[J/(kg.°C)]	4200	-	-	-
Gas heat capacity	$c_{p,a}$	[J/(kg.°C)]	1000	-	-	-
Global heat capacity	C_p	[J/(kg.°C)]	-	1000	750	-
Liquid thermal expansion coefficient	β'_w	[°C^{-1}]	$4\ 10^{-4}$	$4\ 10^{-4}$	$4\ 10^{-4}$	-
Solid thermal expansion coefficient	β'_s	[°C^{-1}]	$2.1\ 10^{-4}$	$2.5\ 10^{-5}$	$1\ 10^{-5}$	$2.5\ 10^{-5}$
Hydraulic parameters						
Intrinsic water permeability	$k_{w0,sat}$	[m^2]	$5\ 10^{-21}$	$4.5\ 10^{-19}$	$1\ 10^{-19}$	
Kozeny-Carman coefficient 1	EXPM	[-]	5.3	0	0	-
Kozeny-Carman coefficient 2	EXPN	[-]	5.5	0	0	-
Relative permeability coefficient	CKW1	[-]	2.9	-	-	-
Volumetric parameters						
Initial porosity	n_0	[-]	0.4074	0.01	0.15	0
Tortuosity	τ	[-]	0.5	0.6	0.6	
Solid specific mass	ρ_s	[kg/m^3]	2'700	2'660	2'500	7'800
Water specific mass	ρ_w	[kg/m^3]	1'000	1'000	1'000	-
Air specific mass	ρ_a	[kg/m^3]	1.18	-	-	-
Liquid compressibility	$1/\chi_w$	[Pa^{-1}]	$3.33\ 10^{-10}$	$3.33\ 10^{-10}$	$3.33\ 10^{-10}$	-
Mechanical parameters						
Young elastic modulus	E	[MPa]	See Tab. 2	5'000	3'000	20'000
Poisson ratio	υ	[-]		0.35	0.2	0.3
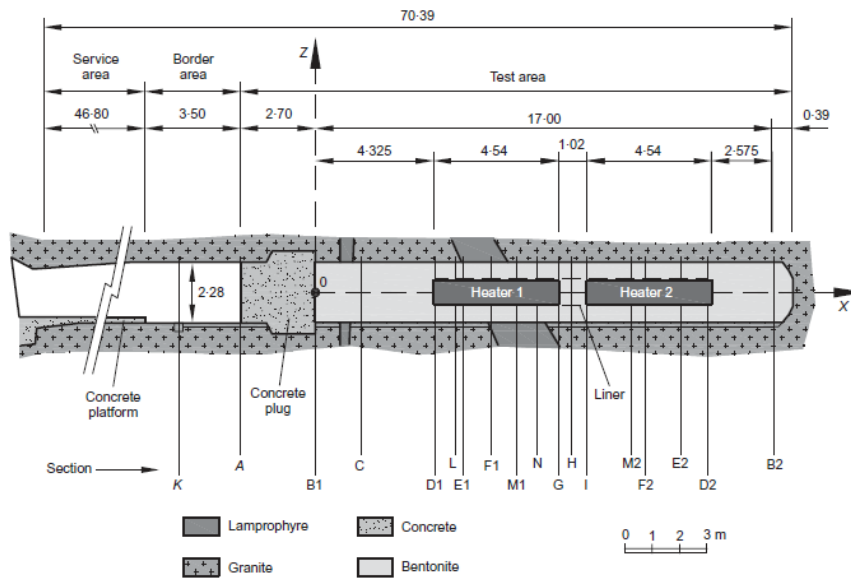
a)
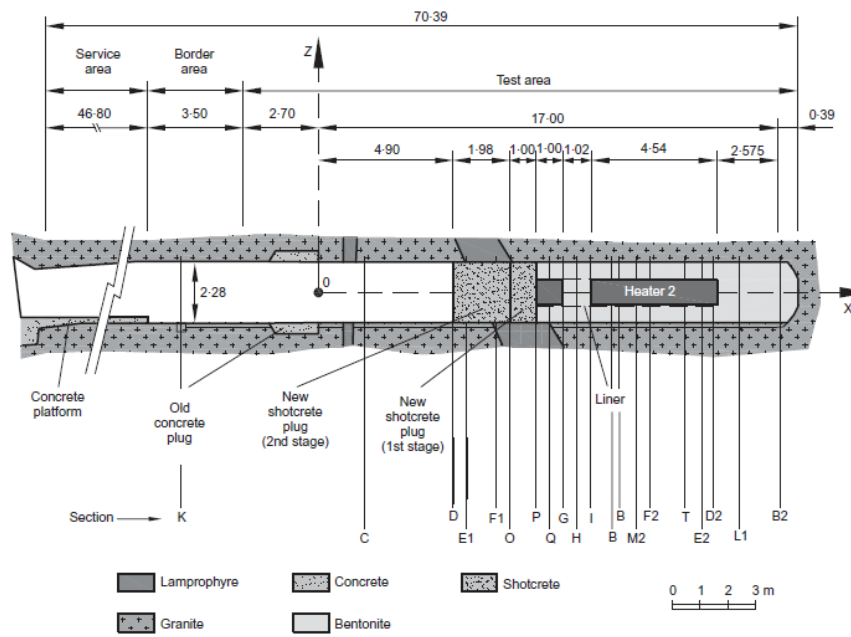
b)

Fig. 3-10:   Layout of FEBEX in-situ test. (a) Instrumented sections before first dismantling. (b) Instrumented section after first dismantling.

Figures taken from Gens et al. (2009).

3.4.1 Ventilation process results

During the 135 days between the end of EBS construction and the beginning of the heating process, the buffer system starts to absorb water from the granite. Modelling this process will generate a more realistic starting condition for the heating phase. The effects of this process are presented in Fig. 3-11 in terms of degree of water saturation and suction distribution in the buffer system.
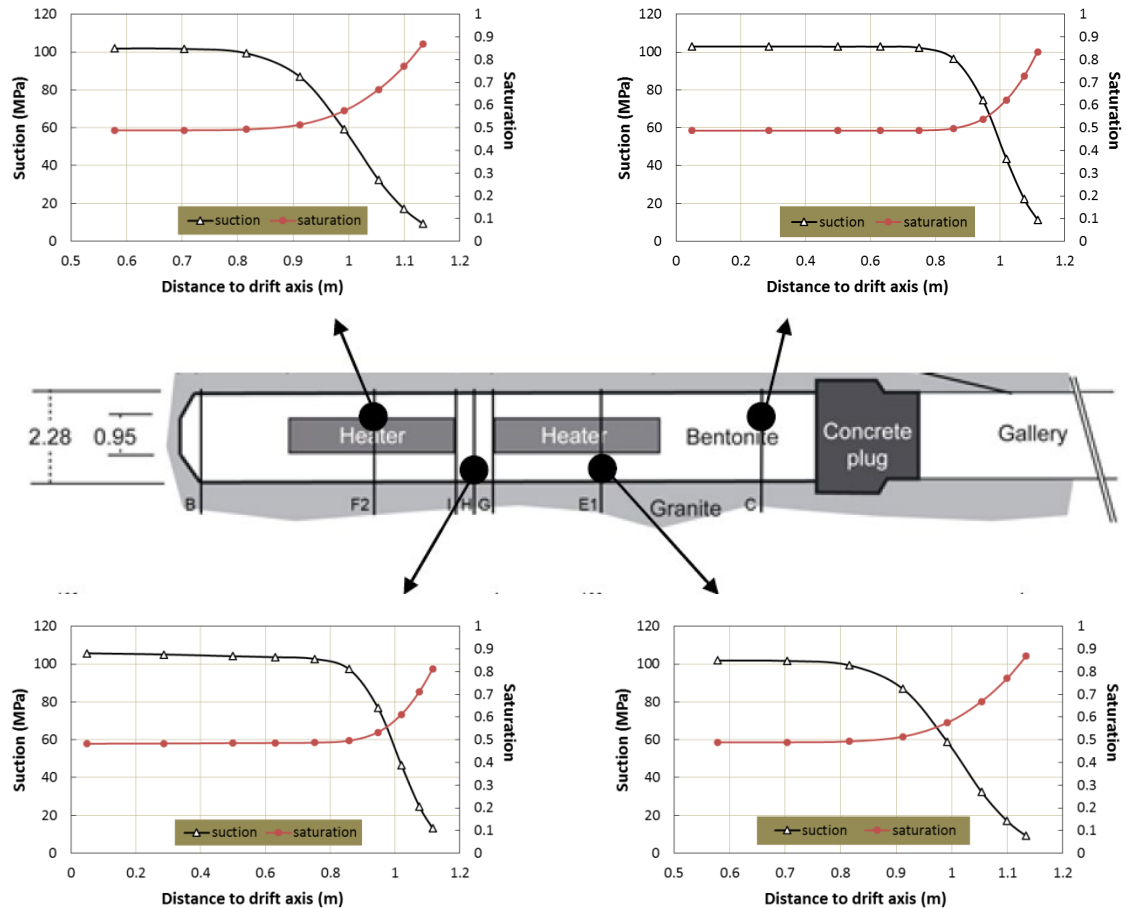
Fig. 3-11: The suction distribution and saturation degree of water distribution at the end of ventilation process.

It is clear that the suction in the outer part of the buffer decreases significantly during this period and consequently, saturation increases from an initial value of 0.47 to values ranging between 0.8 to 0.9. However, this process has little effect on the suction near the drift axis. The influence zone is about 0.3 m from the drift surface. With this modification, the water flow would change significantly since the water permeability is a power relationship with saturation, see Eq. 3-15. This process can shift the dry density variation at the first dismantling process. Therefore, it is important to model this process to obtain more realistic results.

3.4.2   Temperature evolution results

Fig. 3-12 shows the temperature evolution with time for some selected sections. The results for Section D1 are only available for about 1'860 days since it was excavated during the first dismantling. Note that several monitoring points for a particular radial distance are depicted for each section.
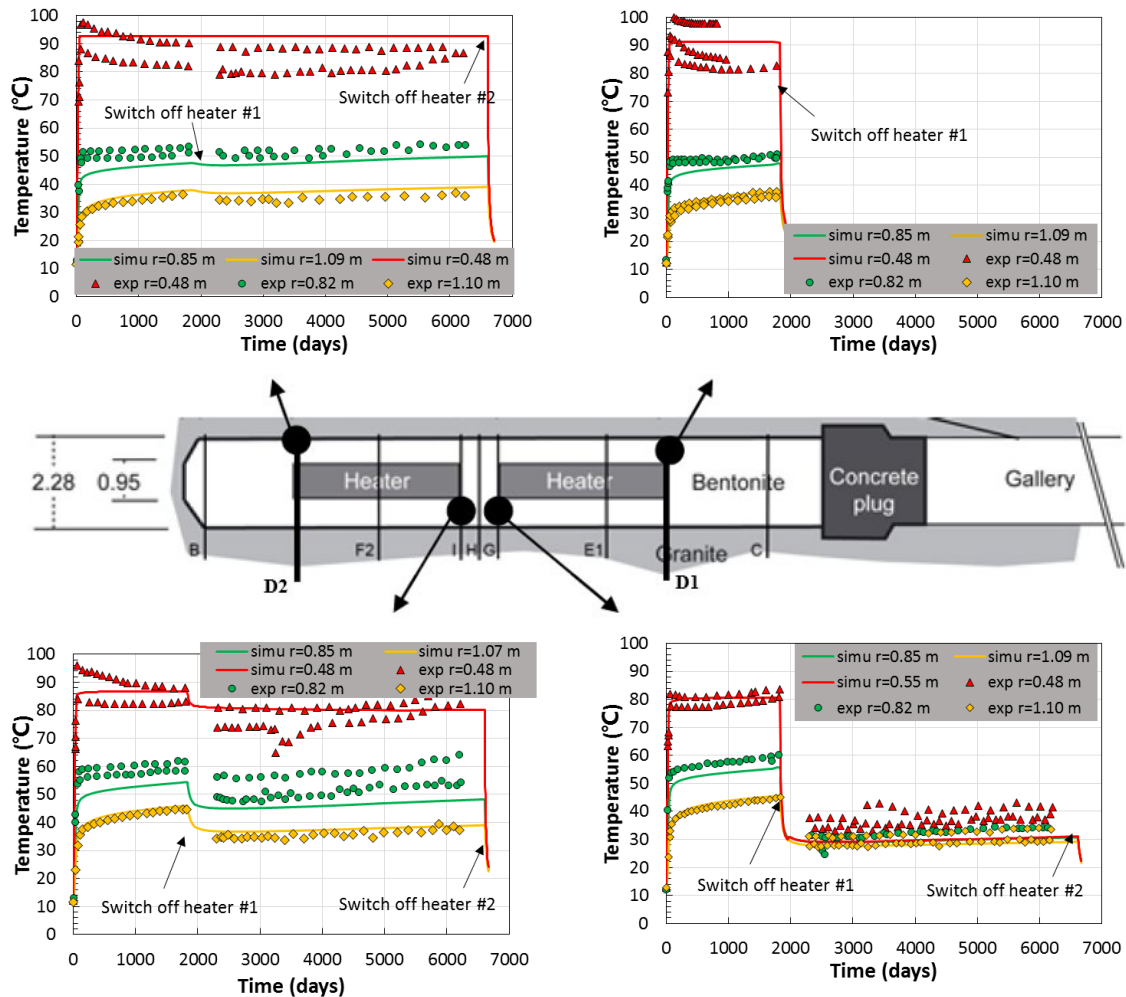
Fig. 3-12:   Evolution of temperature at different sections in buffer system of both monitoring data and simulation results.

The modelling results reproduce the monitoring data in a satisfactory manner. The good agreement at different radial distances also indicates that the thermal conductivity of the buffer system is well captured by Eq. 3-22 considering the effects of the degree of water saturation. During the two, constant-temperature heater phases, the temperature in the outer part increases slowly due to the saturation process. Also, the temperature gradient along the radial direction seems to be constant. Fig. 3-12 also shows that the temperature decreases due to Heater #1 switch-off. The reduction of temperature is related to the distance from Heater #1. Much further from Heater #1, a smaller decrease occurs. There seem to be no effects on the temperature distribution at Section D1 after Heater #1 switch-off, only about a 1 °C decrease of temperature. On the contrary, Section G and D1 show a significant variation. A detailed analysis about the impact of the heating switch-off can be found in Section 3.5.4.

3.4.3   Relative humidity (RH) results

Fig. 3-13 shows the RH evolution for some selected sections. The results for Section C and F1 are only available for about 1'890 days. Since no data for Section H after the first dismantling were available, the monitoring data of Section G were plotted. The distance between Section G and Section H is only about 0.5 m, thus it can be supposed that the RH of these two sections are similar. The good agreement between modelling results and filed data indicates that the THM framework adopted in this work can capture the hydraulic process very well. Unlike the temperature distribution, the measured RH values at the same radial distance seems to have a big variation (maximum variation can be about 30 %). It is interesting to note that the blocks under the heater always have a higher RH than those above the heater. One reason may be that there are some construction gaps at the top part of buffer system which may extend the starting time to absorb water from host water.

At the start of the heating (day 0), the RH at a radial distance of 1.0 m is about 80 %, which is much higher than the initial value. The reason is that the buffer system starts to absorb water from the granite during the ventilation phase (between day 385 to day 520). Moreover, it is obvious that the maximum difference in the monitoring data at Day 0 is about 30 %. This deviation decreases with time. This phenomenon also illustrates that the construction gaps at the upper side of the buffer system can prolong the time when water absorption starts. On the other hand, the swelling deformation of upper part of the buffer system would be larger due to presence of construction gaps. This leads to a higher porosity which indicates a higher water permeability. Thus, the RH increases quickly and the variation between upper and lower part decreases with time.

The RH of the buffer close to the heater shows a decrease after heating. This is due to the bentonite drying by the thermally induced water evaporation. Vapour generated from the drying moves outward and condensates in the cooler regions, leading to accelerated wetting of the bentonite in the central part (see Section F2 and H in Fig. 3-13). Both monitoring data and simulation results show that the RH decreases modestly at Section H and F2 after the switch-off of Heater #1. Much further from Heater #1, those effects disappear.

After about 6'700 days of heating, the whole Section H reaches full saturation, while the RH of the bentonite close to Heater #2 at Section F2 only reaches about 92 %. This is due to the high temperature in this zone; the thermally induced evaporation prolongs the time to reach the full saturation state. After Heater #2 switch-off, the RH decreases moderately due to the decrease of temperature.
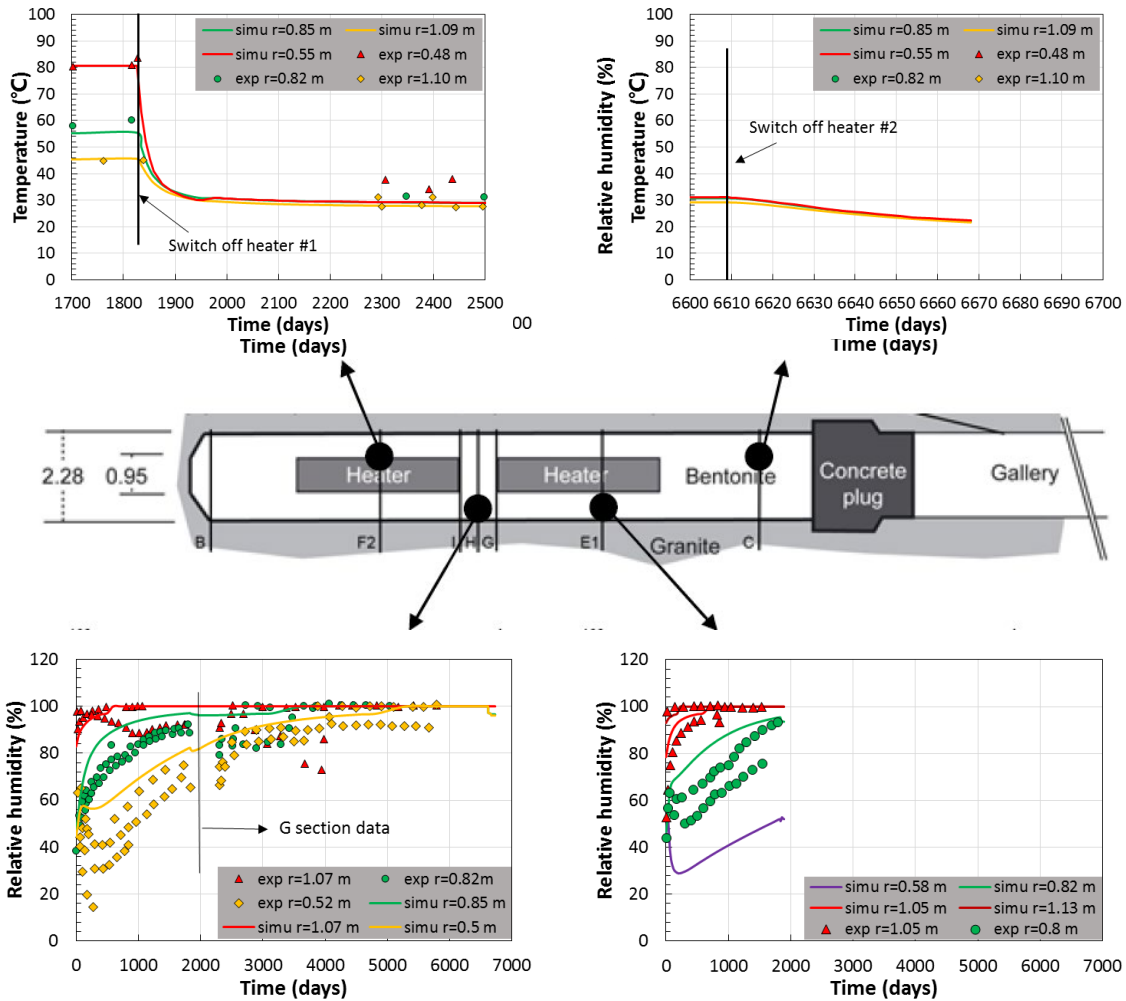
Fig. 3-13:   Evolution of relative humidity at different sections in buffer system of both monitoring data and simulation results.

3.4.4   Impact of heater switch-off

As discussed, the heater switch-off affects both temperature and RH distribution in the buffer. The temperature variation at different sections during both heaters' switch-off phases are plotted in Fig. 3-14. Since no monitoring data are available for the Heater #2 switch-off at the time of this report, only the simulation results are presented while both field data and modelling data are shown for the phase of the Heater #1 switch-off.

Due to the switch-off of Heater #1, the temperature at Section G decreases quickly and reaches a new steady state after about 150 days. The temperature gradient along the radial direction also disappears, since no heating power is applied. However, for Section I, the temperature gradient is maintained due to the heating power from Heater #2. The reduction of temperature along the different radial distances shown here is similar, about 8 °C. It is indicated that the Heater #1 switch-off has no effect on the temperature distribution at sections F2 and D2 because of the distance of those two sections from Heater #1.
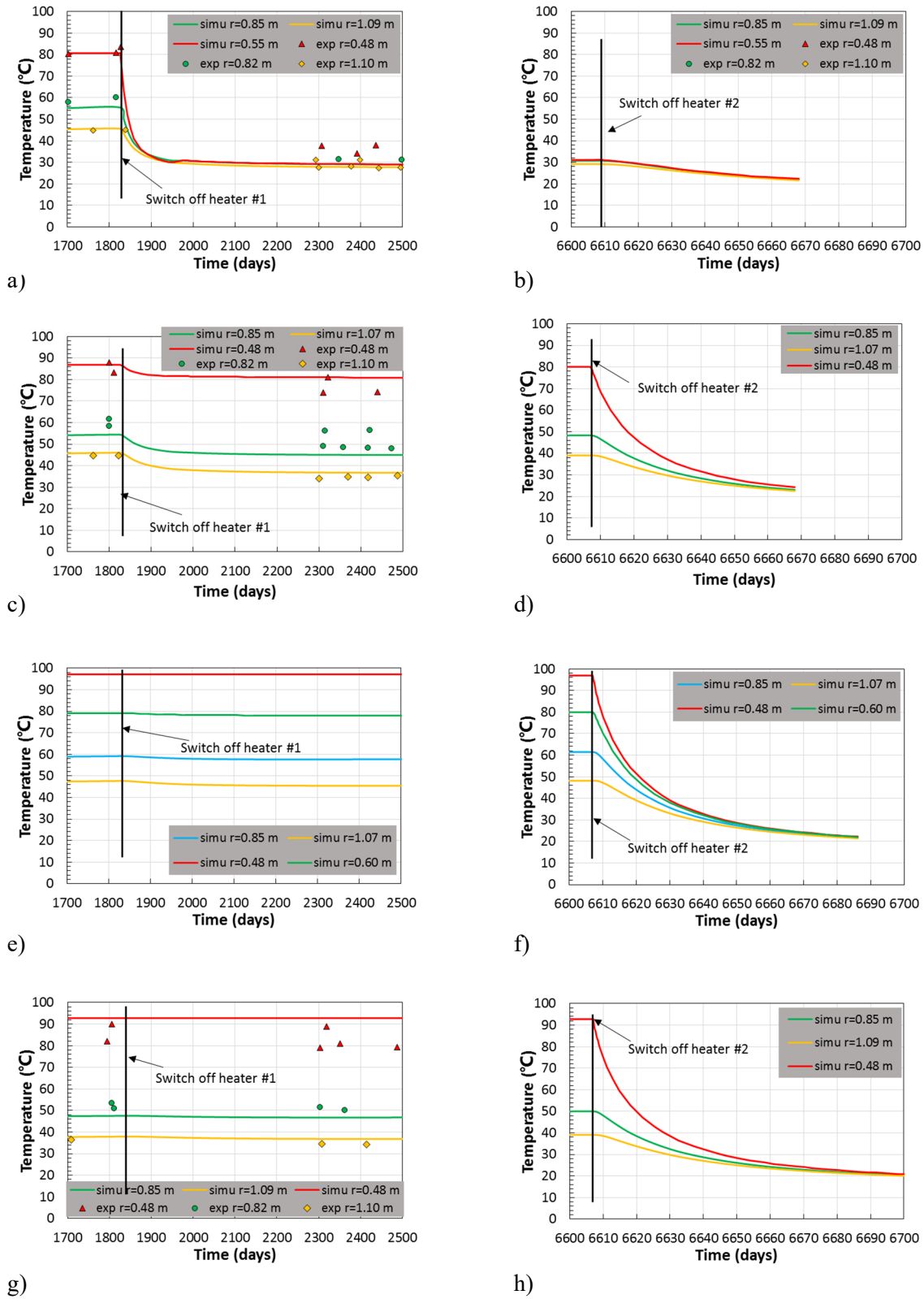
Fig. 3-14:   Impact of heater switch-off on temperature evolution at different sections. Section
             G: (a), (b); Section I: (c), (d); Section F2: (e), (f).

Sixty days after switching off Heater #2, the temperature gradient in all sections disappears and the temperature reaches a final value of about 22 °C. This final temperature is about 10 °C higher than the initial value of 12 °C, suggesting that not enough time was allowed in the simulation to recover the initial condition. As stated in Section 5.3, a decrease of RH can be found after heater switch-off. However, this impact is limited (Fig. 3-13) and can be captured by Kelvin's Law.

3.5   Interpretation of the results

3.5.1   Driving processes

Complex THM coupling processes happen in the buffer region during the test. The significant phenomena that affect the bentonite region are the heating from heaters and hydration for the surrounding granite.

In the period between the emplacement of the materials and the onset of heating (from day 385 to day 520), the temperature is expected to be relatively homogeneous and no thermally induced stresses or deformations take place. The only driving force for transport is the hydraulic gradient between the buffer and the surrounding granite. Due to the high initial suction in the buffer, water flows into the bentonite from the higher-pressure zone in the surrounding rock. During this process, the mechanical behaviour is also affected due to the high swelling capacity of bentonite. Through the expansion into the void volumes associated with the construction gaps between the blocks, and between the blocks and the drift surface, the initial swelling of bentonite induces a higher porosity of the bentonite matrix. This results in a higher intrinsic conductivity. Considering that the degree of water saturation increases with absorbing water, the water flow rate will increase during this phase. This fast water flow will be neutralized by the decease of hydraulic gradient with time. However, the tunnel drift will constrain the swelling deformation and swelling pressure would be generated.

During the heating phase, one additional driving force is the thermal gradient. At the inner part of buffer system, high heat fluxes occur from the heaters to bentonite. This heat flux will generate a thermal gradient in the buffer system as well as in the granite zone. Due to the high temperature, the inner part of buffer system will be associated with high water evaporation, which leads to the drying of bentonite. Thus, the degree of saturation will decrease and suction will increase in this region, as shown in Fig. 3-13. The water vapour will flow outwards and it will condensate in the cooler region, leading to an increase of water content in that region. This process increases the saturation rate of the middle part (see in Fig. 3-13). The reversed process takes place during the cooling phase with the increase of suction in the middle part and the simultaneous flow of water from the middle to the inner part, whereas the middle part cannot absorb enough water from the outer part. Vapour diffusion is a significant mechanism of water transfer and it also contributes to heat transport. Owning to this vapour flux, the transfer of water transfer becomes much more complex under thermally-induced effects.

Owning to thermal loading, the bentonite will shrink, causing an increase in dry density. However, the mechanical response under thermal loading of bentonite needs to be investigated further. A topic of interest is whether this thermally induced shrinking is recoverable or not. Laloui et al. (2009) point out that the thermal loading can cause some plastic deformation for the normally consolidated clays (Laloui & François 2009). The initial stress state of FEBEX blocks can be assumed to be highly over-consolidated. Therefore, no thermal plasticity effects are considered in this work. However, owing to the presence of montmorillonite, the fabric of bentonite can be modified with the absorption of water, which may change the bentonite

consolidation state from over-consolidation to normal consolidation. If that is the case, the thermal irrecoverable deformation would occur in the inner part of buffer system. Moreover, the coupling effects of thermal loading and hydraulic loading on mechanical response also need to be further investigated.

3.5.2 Modelled density and saturation distributions and the remaining uncertainties

3.5.2.1 Results at a cool section during the first dismantling

Fig. 3-15 shows both modelling results and measured data of dry density and water content as a function of the distance from the tunnel axis for a section far away from the heater (Section 15 in the first dismantling). The good agreement between experimental and modelling results indicates that the THM framework can capture the complex coupling process very well. The decrease of dry density observed in the measurements in the part next to granite is due to the swelling deformation of bentonite. The swelling of the outer region will compress the inner part, causing an increase of dry density in the inner part. It is indicated that the model underestimates the decrease of dry density at the outer part. Two reasons are responsible for this deviation. One is that the mechanical law adopted in the simulation has a limitation in modelling the high swelling potential of bentonite for the condition that the degree of saturation is close to one. The other reason could be related to the fact that the construction gaps between the buffer system and the granite can also lead to a higher decrease of dry density in the outer part next to granite. As stated in the previous section, the outer part is almost fully saturated. The underestimation of the swelling deformation also leads to an underestimation of the water content in the outer part of buffer system, see Fig. 3-15b. It is clear that the water content at all radial distances increases during the first five years of heating, although the increase in the inner part is only between 3 % to 5 %. This is related to the thickness of buffer and the low water permeability of the bentonite.

a)   b)
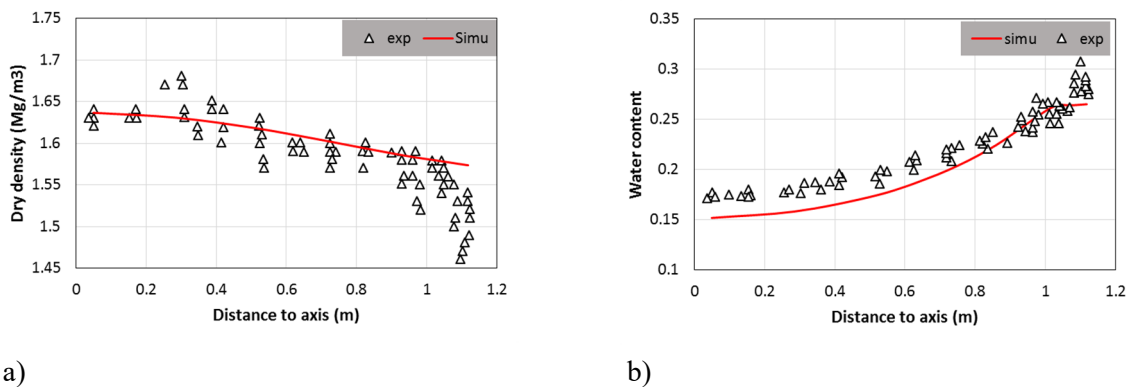
Fig. 3-15:   Comparison between values measured during dismantling and simulation results at a cool section (Section 15): (a) dry density, (b) water content.

3.5.2.2 Results at a hot section during the first dismantling

Fig. 3-16 shows both modelling results and measured data of dry density and water content as a function of the distance from the tunnel axis for a section near Heater #1 (Section 27 in the first dismantling). The dismantling effect on the dry density distribution is also plotted. The modelling results show a good agreement with experimental results for the inner part (ca. 2/3 of

the buffer thickness) while some deviation is observed in the outer part (ca. 1/3 part of the buffer thickness). This deviation can be explained by the effects of swelling and construction gaps on dry density and water content, in the same way as discussed above.

In comparison to the results at the cool section, a higher increase of dry density occurs in the inner part of the hot section. This is due to thermal loading. The high temperature causes the drying of bentonite, leading to shrinking in that region. The water content results show that there is a decrease of water content in the inner part of buffer system. The thermally induced drying effects cannot be compensated by hydraulic flow, even five years after the emplacement of the buffer.

The dry density decreases after dismantling because of unloading during the dismantling or coring processes. The decrease predicted by the simulation is about 0.02 Mg/m^3. Based on the measured dry density after dismantling, an average dry density can be calculated to be 1.57 Mg/m^3, which is about 0.03 Mg/m^3 smaller than the initial average dry density of 1.60 Mg/m^3. However, other reasons that can also lead to the decrease of the dry density are the coring technology and field test technology.
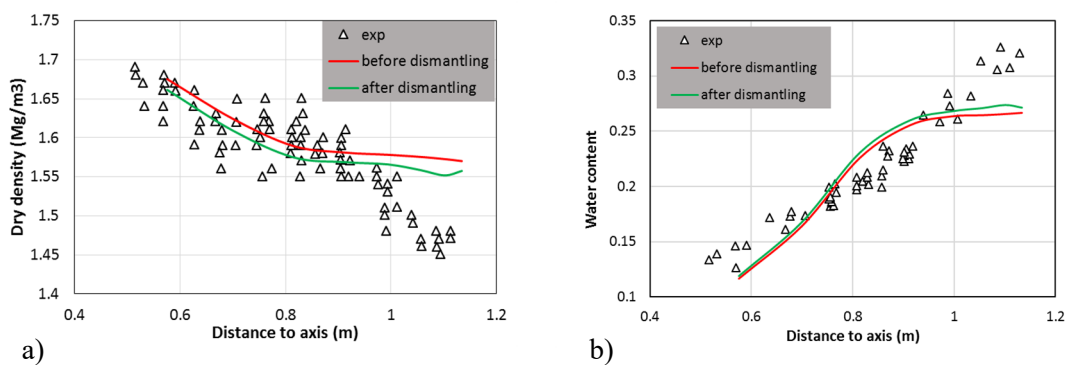
Fig. 3-16:   Comparison between values measured during dismantling and simulation results at a hot section (Section 27): (a) dry density. (b) water content.

3.5.2.3   Predicted results at a cool section during the second dismantling

The dry density and water content predicted for a cool section (Section G) are presented in Fig. 3-17 and Tab. 3-4. After 18 years, the entire Section G is almost fully saturated. It is observed that even in the inner part the degree of saturation reaches about 99.4 %. Looking at the suction values, a suction gradient is still observed along the radial direction and the maximum suction at the inner part of buffer system is about 4.14 MPa. Since the air entry value of 4 MPa is used in the simulation, the full section seems to reach the full saturation state. However, a different value for the air entry pressure could shift the saturation condition. An additional uncertainty comes from effects of fabric modification due to absorbing water on the air entry value.

The dry density at the Section G is almost homogeneous. The reason for this predicted result is that irrecoverable hydraulic swelling deformations are not foreseen by the mechanical law used in the analysis. Therefore, the deformation of the buffer system is assumed to be elastic. Thus, after the buffer system reaches full saturation, a homogeneous dry density with the initial value of 1.6 Mg/m^3 is recovered. This is also concluded by Dixon et al. (2002) who provide the analysis of two large-scale sealing tests conducted at Canada's underground laboratory.

Tab. 3-4:   Predicted results at cool section (Section G) during second dismantling.

Radial distance to axis (m)	Porosity (n)	Degree of saturation Sr (%)	Suction s (MPa)	Dry density (Mg/m³)	Water content (%)
0.05	0.409	99.4	4.14	1.596	25.48
0.28	0.407	99.4	4.14	1.601	25.27
0.50	0.406	99.9	4.02	1.603	25.29
0.63	0.407	100	4.00	1.601	25.42
0.76	0.409	100	3.94	1.596	25.63
0.86	0.409	100	3.89	1.596	25.63
0.95	0.409	100	3.76	1.596	25.63
1.02	0.409	100	3.34	1.596	25.63
1.08	0.410	100	2.65	1.593	25.74
1.12	0.410	100	1.82	1.593	25.74
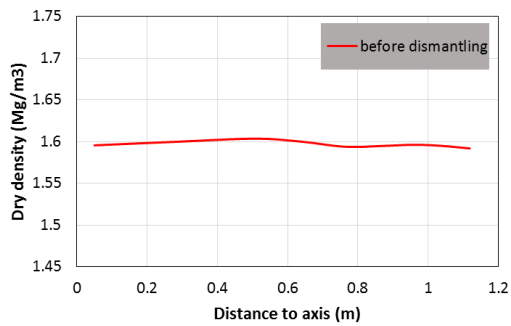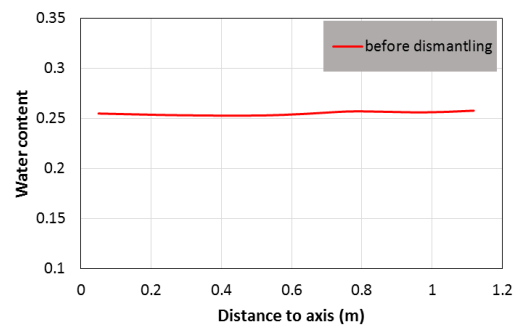
a)   b)

Fig. 3-17:   Prediction results at cool section (Section G): (a) dry density, (b) water content.

3.5.2.4   Predicted results at a hot section during the second dismantling

Fig. 3-18 shows the predicted dry density and water content for a hot section near Heater #2 (Section F2). The detailed results are also given in Tab. 3-5. Owing to thermal effects, the inner part of Section F2 still has high suction, about 12.52 MPa. This means that, although a certain amount of water has reached the inner region, the inner region is still not fully saturated after 18 years. One interesting aspect is the increase of suction predicted in the middle part of the buffer system. This is related to the switch-off of Heater #2 and is similar to that observed for the switch-off of Heater #1, discussed in the previous section. Due to the incomplete saturation of inner part, a dry density gradient is observed in this section. The maximum difference between inner and outer part is about 0.03 Mg/m^3. Since neither thermal plasticity nor irrecoverable hydraulic swelling deformation are considered in the simulation, this dry density gradient may be underestimated. The unloading during dismantling cannot be avoided. Thus, a smaller average dry density than the initial value of 1.6 Mg/m^3 is expected, as discussed for the first dismantling.

Tab. 3-5:   Predicted results at a hot section (Section F2) during second dismantling.

Radial distance to axis (m)	Porosity (n)	Degree of saturation Sr (%)	Suction s (MPa)	Dry density (Mg/m^3)	Water content (%)
0.58	0.401	82.0	12.52	1.617	20.33
0.71	0.406	98.9	4.28	1.604	25.04
0.82	0.4065	98.5	4.39	1.602	24.99
0.92	0.407	98.8	4.29	1.601	25.11
1.00	0.408	99.4	4.16	1.598	25.37
1.06	0.408	100	3.65	1.598	25.53
1.10	0.409	100	2.63	1.596	25.63
1.13	0.411	100	1.53	1.590	25.84
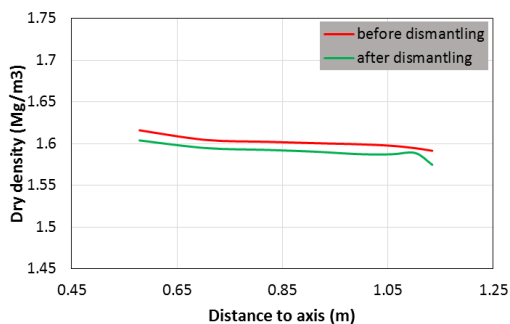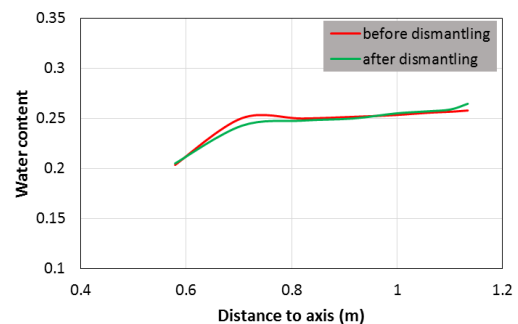
a)   b)

Fig. 3-18:   Prediction results at a hot section (Section F2): (a) dry density, (b) water content.

3.5.3   Progress made in this exercise, remaining uncertainties

The main focus of this simulation work is the thermo-hydro-mechanical behaviour of the buffer system, thus a careful calibration and analysis were carried out based on the experimental results. A much deeper understanding of the hydraulic swelling mechanism was obtained through this exercise. Based on the simulation results and monitoring results, it can be summarized that both the thermal mechanism and hydraulic mechanism can be well captured by the current EPFL model. However, there are still some remaining uncertainties related to the mechanical response of the bentonite. Among these uncertainties is whether thermal plasticity exists for the FEBEX bentonite blocks. Another uncertainty is the swelling mechanism for the material with a very high swelling potential. Behind these two uncertainties, one intrinsic issue is how the fabric of bentonite is modified during the swelling process. This fabric modification happens at both macro and micro level, as well as because of the interaction between them. To fill this gap, much more laboratory tests should be conducted to investigate the swelling mechanism at both macro and micro level.

Another uncertainty of the FEBEX dismantling simulation is related to the effects of the construction gaps on the THM coupling processes. Owning to these construction gaps, the mechanical boundaries of the FEBEX blocks vary with time. As an example, one may consider the outer part of the buffer system. At the initial condition, the blocks can be assumed to swell under free swelling conditions due to the gaps between the buffer and the granite. While the gaps are filled by the swelling of blocks, the blocks swell under constant volume conditions and swelling pressure is generated. Those construction gaps can also affect the water transfer. As presented in previous section, the gaps between the buffer and the granite can delay the time to absorb water from granite. Moreover, the gaps in the radial direction and those in the circular direction can also have different effects. Although some tests have investigated the gaps effects on hydraulic conductivity already, there are not enough results to build a clear concept on the effects of gaps.

3.5.4   Consequences for the early repository evolution

After 18 years of testing, the section far from Heater #2 (Section G) seems to reach full saturation based on both simulation results and monitoring data. However, for the section near the Heater #2 (Section F2), the inner part is still unsaturated owing to the thermal gradient along the radial direction. After Heater #2 switch-off, a fast increase of saturation in the inner part is observed due to a higher hydraulic gradient developing between the middle part and inner part and the absence of a thermal gradient counteracting this hydraulic gradient. Thus, it is expected that after that the canister is beyond the highest thermal peak, the saturation process will become faster and the time required to attain full saturation will decrease. Based on the simulation results, the dry density gradient will disappear after the whole buffer system will reach the full saturation state.

3.6　　　　Conclusions

With the dry density distribution prediction in mind, a careful calibration and analysis of swelling deformation behaviour of the FEBEX bentonite were carried out based on the ACMEG-TS model. The simulation of the FEBEX in-situ test was conducted from the excavation phase to the second dismantling phase. The simulation results reproduce the monitoring data very well. This indicates the soundness of the THM framework adopted in this work. For the dry density distribution and saturation prediction, the following observations can be made.

- The modelled results of dry density gradient and water content show a good agreement with the measured data in the first dismantling phase. The predicted dry density at the outer part is higher than the measured values. Two reasons account for this deviation. One is that the model may underestimate the swelling deformation of FEBEX bentonite. The other reason is the effect of construction gaps.

- The predicted dry density for the cool section during the second dismantling seems to be homogeneous. The dry density gradient measured in the first dismantling disappears. The whole section reaches full saturation based on the water retention curve used in this work. Note that there is still a suction gradient.

- The predicted dry density for the hot section during the second dismantling still has a gradient. The inner part has a higher dry density while the outsider part has a smaller one. The difference between them is about 0.3 Mg/m^3. The dry density gradient is smaller than that measured in the first dismantling. The inner part is still unsaturated with a degree of saturation of about 82 %.

- The dismantling process or coring technology can cause a decrease of the average dry density. In the first dismantling, a decease value of 0.03 Mg/m^3 is measured. Since the measured swelling pressure is still increasing during the second constant temperature heater phase, the unloading effect during second dismantling is expected to be bigger. Thus, a much higher decrease of average dry density is expected.

4   THM modelling by Clay Tech

This chapter describes the modelling analyses performed by Clay Tech. Section 4.1 gives an overview of the model and underlying assumptions. Section 4.2 gives a short overview of the history of the development of the model. Section 4.3 provides the initial and boundary conditions as well as input parameters used in the simulations. Section 4.4 discusses the model outcomes in the following steps:

- evolution of relative humidity and radial stresses

- distributions of water content and dry density

- stress paths

The analysis from Clay Tech concludes with an interpretation of the results in Section 4.5.

4.1   Description of the model and underlying assumptions

The re-saturation and the dry density distribution of the bentonite at the mid-section of Heater #2 in the FEBEX in-situ tests (Section F2) was evaluated and predicted with a 1-D axisymmetric THM model implemented in Code_Bright v4. The problem domain and model geometry is illustrated in Fig. 4-1. A timeline of the model with the main events is given in Tab. 4-1.

The thermo-hydraulic processes were essentially described by the following three transport processes:

i)   heat transport, controlled by the temperature gradients (Fourier's law)

ii) liquid transport, controlled by the liquid pressure gradients (Darcy's law)

iii) vapour diffusion, controlled by vapour mass fraction gradients (Fick's law)

The mechanical processes were modelled with the thermoelastoplastic constitutive laws (implemented in Code_Bright) which are based on the Barcelona Basic Model (BBM).

4.1.1   Thermal model

In order to motivate a specific temperature level for the outer boundary in the numerical model, an analytical thermal model was developed. This was based on two line sources, one for each heater (Fig. 4-2), following the expression reported by Ikonen (2003):

$$\Delta T(r,z,t) = \int_0^t \frac{P(\tau)}{t-\tau} \cdot \frac{\exp\left(\frac{-r^2}{4D(t-\tau)}\right)}{\rho c \cdot 8\pi \cdot HD} \cdot \left[\text{erf}\left(\frac{\frac{H}{2}+z}{2\sqrt{D(t-\tau)}}\right) + \text{erf}\left(\frac{\frac{H}{2}-z}{2\sqrt{D(t-\tau)}}\right) \right] d\tau \qquad (4\text{-}1)$$

where ΔT is the temperature increase, $P(t)$ is the power history, H is the length of the line source, ρ is the density, c is the heat capacity, and D is the thermal diffusivity (equal to $\lambda/\rho c$, where λ it the thermal conductivity). For the analysed case, the following parameter values were used for the rock: $\lambda = 3.6$ W/mK and $c = 793$ J/kgK (Gens et al. 2009) and $\rho = 2'640$ kg/m^3 (Alonso & Alcoverro 2005). Together these values correspond to a thermal diffusivity of

1.72×10^{-6} m^2/s. The initial temperature was set to 12 °C. The used power histories for the two heaters are shown in Fig. 4-3 (upper left).

A resulting contour plot of the temperature field for day 1000 is shown in Fig. 4-3 (lower graph). Temperature evolutions at four points along the rock wall, which correspond to sensor positions in Section D1, G, I and D2 are shown in Fig. 4-3 (centre right). These evolutions can be compared with corresponding sensors data (see Fig. 4-3, upper right). The agreement between these evolutions illustrates the validity of the thermal model, which, therefore, can be used for evaluating the temperature evolution at the mid-sections of the heaters at the rock wall (Fig. 4-3, centre left).
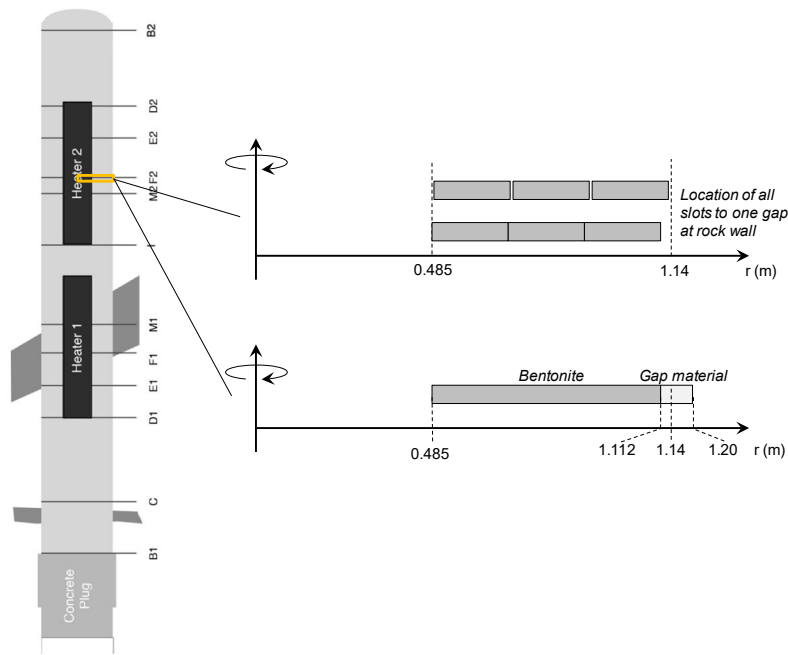
Fig. 4-1:   Problem domain, schematic illustration of location of all slots at rock wall and model geometry.

         The geometry was discretized as an array of 25 elements in the bentonite and two elements in the gap material.

Tab. 4-1:   Model timeline

Date	Event	Day
1996-10-15	Installation	0
1997-02-27	Start heating	135
1997-04-22	Start temp control	189
2002-02-28	First dismantling	1'962
2015-02-28	Second dismantling	6'710
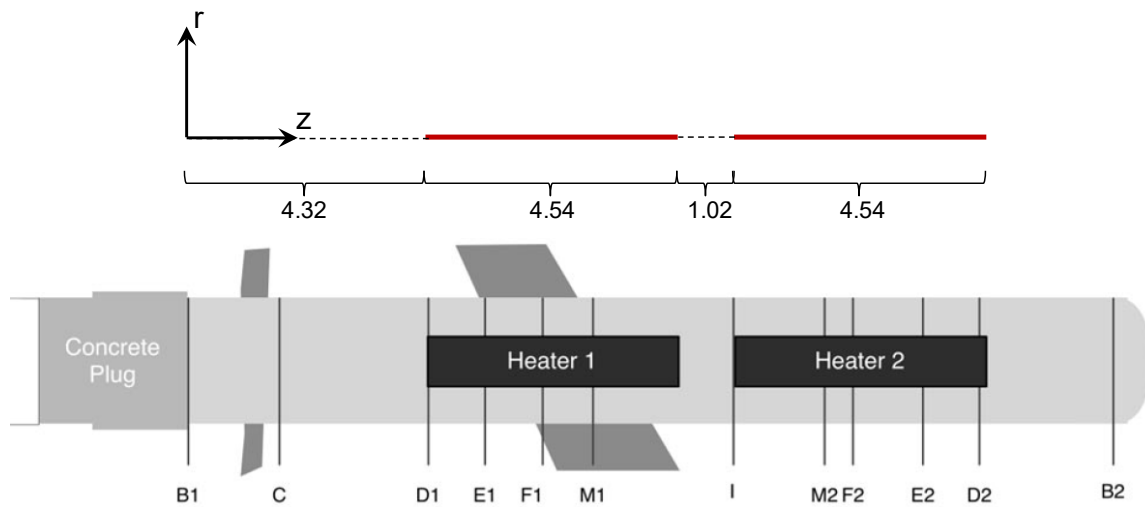
Fig. 4-2:   Geometry of the analytical model.

4.1.2   TH models

Two TH models were developed during the initial phase of this modelling task: one with a porosity corresponding to the homogenized dry density of the bentonite (1'600 kg/m^3), and one corresponding to the initial dry density of the blocks (1'700 kg/m^3). The geometry of the latter model had a geometry with reduced outer radius (Fig. 4-4). The motive for these models was to obtain a general estimate of the re-saturation process before the models were advanced to include the mechanical processes as well. It was found that the time-scale of re-saturation was quite similar to the results of the main THM model. However, since these TH models clearly are inferior to the THM model for predicting the final distributions of dry density and water content, they are not presented any further in this report.
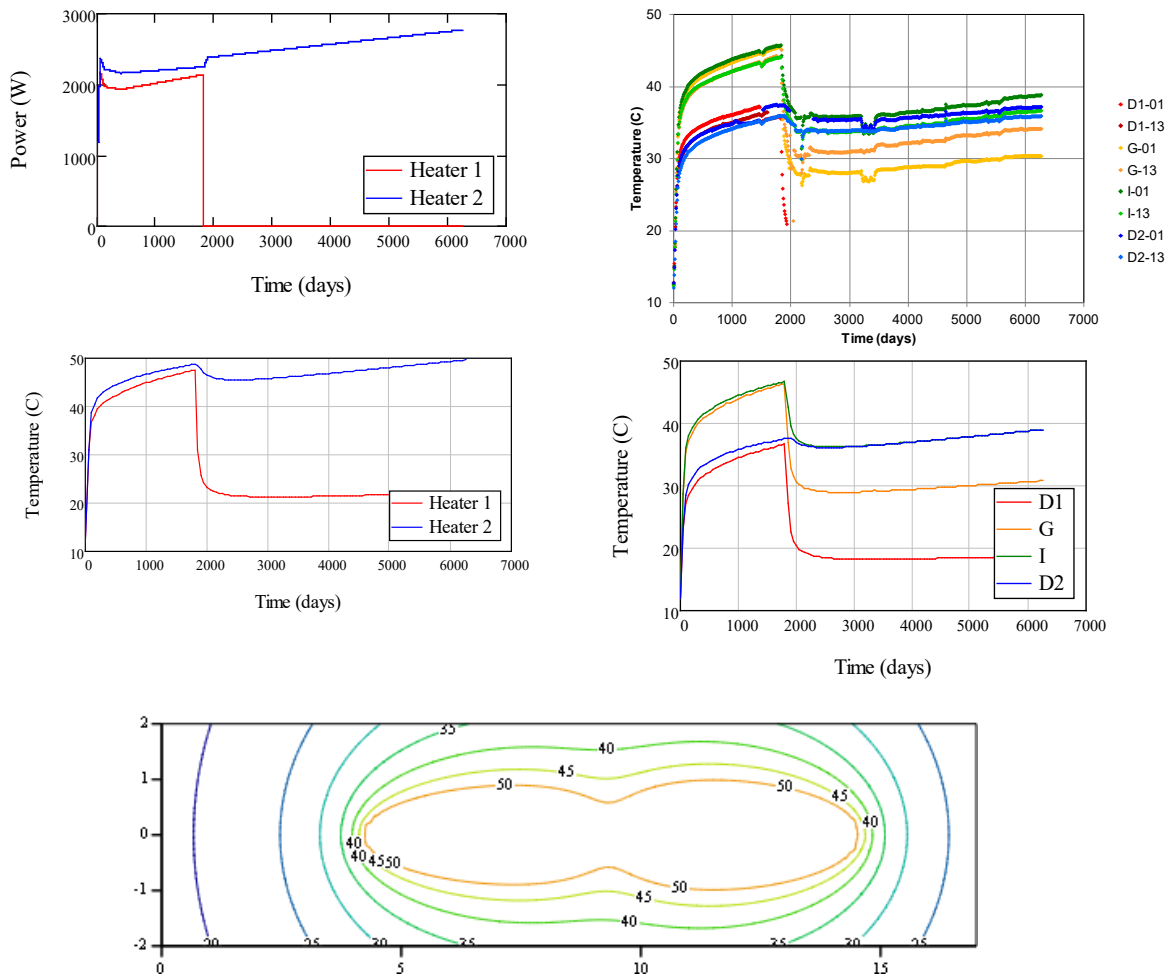
Fig. 4-3:   Power histories used as input for analytical model (upper left).

Measured temperature evolution at rock wall at four sections (upper right), calculated temperature evolution at corresponding four sections (centre right) and at heater mid-sections (centre left). Calculated temperature contour-plots for day 1000.
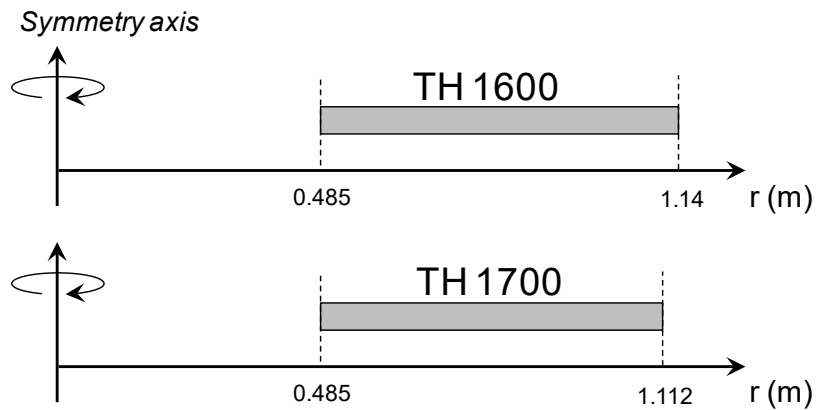
Fig. 4-4:   Geometry of TH models.

4.2   Development of the FEBEX model

The presented THM model was developed as a "pre-dismantling task" and was not a continuation of any previous work. The different models, created during the development of this modelling task, are described in this chapter.

4.3   Description of the initial and boundary conditions, input parameters

4.3.1   Basic data and initial conditions

The initial conditions of the models (Tab. 4-3) were largely based on a few basic data concerning the dry density, the water content, the particle density, and the initial temperature (Tab. 4-2). The initial suction value (i.e. the negative liquid pressure) was based on water retention data for free swelling conditions. The initial water content in this case (14.4 %) corresponds to a RH of 40 % (Fig. 4-5).

4.3.2   Boundary conditions

The thermal problem was simplified by boundary conditions with constant temperatures. This was considered to be a relevant approach since a goal for the heating had been to maintain a maximum temperature of 100 °C at the steel liner-bentonite contact. Measured temperatures at this radius in the mid-section of Heater #2 (F2) indicate however, that the temperatures in three out of four directions (sensor SF-01 at the bottom, SF-04 at the top, SF-02 and SF-03 at the sides) were significantly lower (Fig. 4-6). Based on these measurements a general temperature level of 94 °C was adopted for the inner boundary condition. A corresponding level for the outer boundary was based on the results from the analytical model (Fig. 4-3, centre left), and for this boundary a temperature level of 45 °C was adopted.

The boundary conditions for the model are illustrated in Fig. 4-7. The temperatures were increased linearly from the initial level to the defined boundary levels from day 135 to day 189. The pressure boundary and the mechanical roller boundaries were upheld throughout the entire simulation.

The hydraulic problem was simplified with an outer boundary with constant atmospheric liquid pressure, meaning that the bentonite had free access of water. This was motivated by the findings from earlier modelling attempts presented by Alonso & Alcoverro (2005), who concluded that the "… bentonite permeability controls its own rate of hydration and the rock matrix is capable of providing all the required flow of water". In addition, the gas pressure was kept constant at an atmospheric level throughout the model.

The mechanical problem is characterized by highly compacted bentonite blocks, with an initial dry density of 1'700 kg/m^3, and the occurrence of slots and joints which implies that the average dry density was 1'600 kg/m^3. This was taken into account by adopting initial conditions (and properties) for the bentonite, which were representative for the initial block dry density, and by representing all slots as one single 28-mm wide gap at the rock wall.

Tab. 4-2:   Basic data for the used FEBEX bentonite.

Water content*	Dry density*	Particle density**	Initial temperature†
14.4 %	Blocks: 1'700 kg/m^3 Average: 1'600 kg/m^3	2'735 kg/m^3	12 °C

*   Lanyon & Gaus (2013)
** Svensson et al. (2011)
†   Sensors data

Tab. 4-3:   Initial condition in model.

Void ratio	Porosity	Saturation degree	Liquid pressure	Temperature	Stresses
0.609	0.378	0.65	-124.9 MPa	12 °C	0.01 MPa
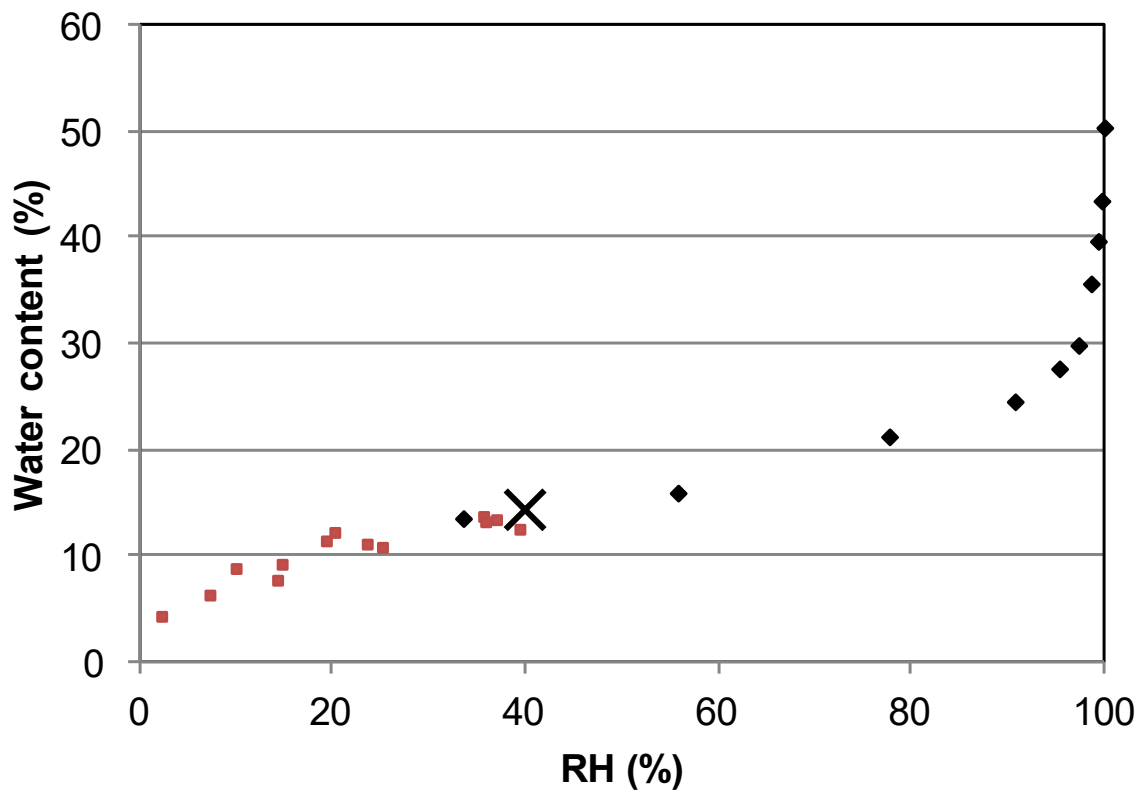
Fig. 4-5:   Water retention data for FEBEX bentonite at free swelling conditions.

Based on data presented by Villar (2002). The initial water content is marked (x).

4.3.3   Material parameters

The thermal and the hydraulic parameter values were all adopted from independent tests with FEBEX bentonite. A linear relation between the thermal conductivity and the degree of saturation was adopted in the following form (Eq. 4-2).

$$\lambda(S_r) = \lambda_{sat} S_r + \lambda_{dry}(1 - S_r)$$
(4-2)

Based on the data presented by Villar (2002), a relation was adopted with the parameter values: $\lambda_{dry} = 0.5$ and $\lambda_{sat} = 1.3$ W/mK (Fig. 4-8, left). For the specific heat, a value of 1'091 J/kgK was adopted from Gens et al. (2009).

A water retention curve was adopted on the following form:

$$S_r(s) = \left(1 + \left(\frac{s}{P_0} \right)^{\frac{1}{1-\lambda}} \right)^{-\lambda} \left(1 - \frac{s}{P_d} \right)^{\lambda_d}$$
(4-3)

Based on the retention data for free volume conditions presented by Villar (2002), a relation was adopted with the parameter values: $P_0 = 22.5$ MPa; $\lambda = 0.09$; $P_d = 1100$ MPa, $\lambda_d = 2.1$ (Fig. 4-8, right). For the vapour diffusion tortuosity, a value of 0.8 was adopted from Alonso and Alcoverro (2005) and Gens et al. (2009)

The intrinsic permeability was evaluated from water-uptake tests presented by Åkesson (2013). These two tests were performed on 50-mm long specimens with free access of water from one side during 2 and 3 weeks (Fig. 4-9 upper left). After dismantling the water content profile in the bentonite was analysed (Fig. 4-9 upper right). From this, a moisture diffusivity value of approximately 5.7×10^{-10} m^2/s could be derived. For unsaturated conditions with a homogenous porosity, this diffusivity is related to the intrinsic permeability (k), the relative permeability ($= S_r^3$), the derivative of the retention curve (dP_l/dS_r), the porosity (n) and the viscosity (μ) through the relation:

$$D(S_r) = \frac{k \cdot S_r^3}{n \cdot \mu} \cdot \frac{dP_l}{dS_r} \qquad (m^2/s)$$
(4-4)
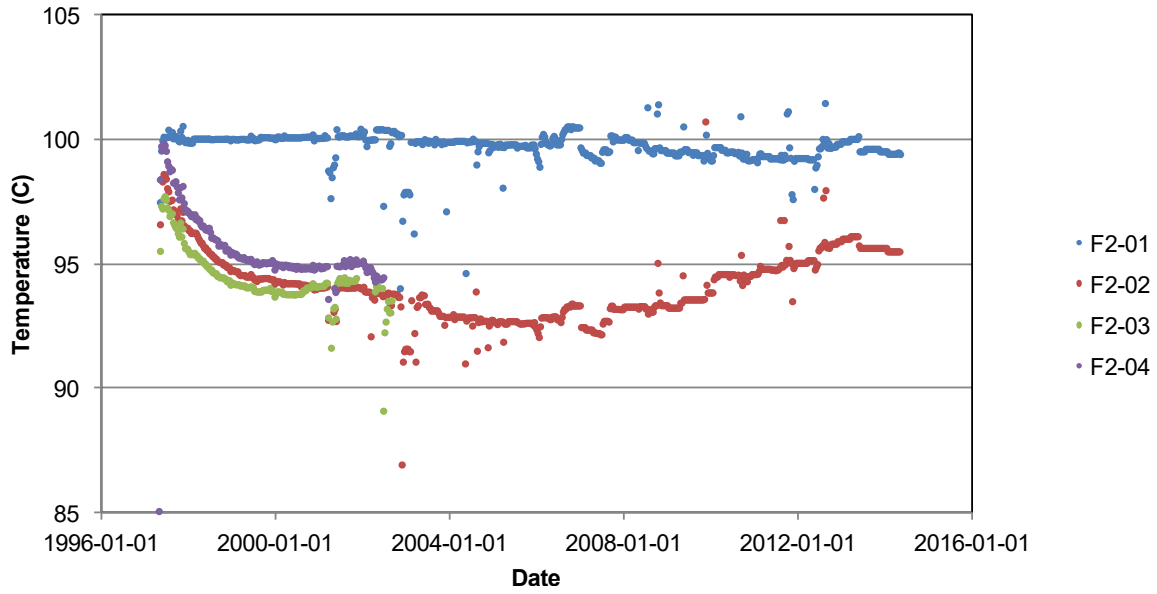
Fig. 4-6:   Measured temperatures at liner-bentonite contact in Section F2 (instrumented cross-Section 48: sensors SF-01 to SF-04 in four directions).
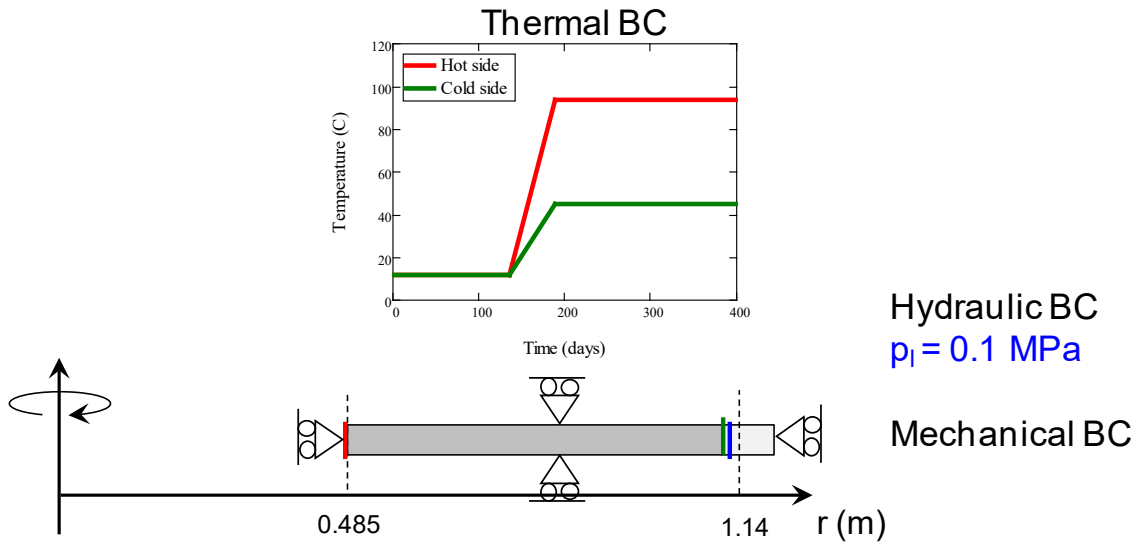
Fig. 4-7:   Schematic illustration of boundary conditions.

Red and green line mark the temperature boundaries and blue line marks the pressure boundary. The conditions applied at the outer boundary were maintained as a "surface condition" over the entire gap material.

For the initial dry density of the blocks (1'700 kg/m^3) an intrinsic permeability value could thereby be calibrated to 1.1×10^{-21} m^2 so that the resulting diffusivity corresponded to the value from the water-uptake tests (at least close to saturated conditions, see Fig. 4-9, lower left). This value was used in the model together with the Kozeny's model for the porosity dependence. A similar evaluation was performed for the homogenised dry density (1'600 kg/m^3) for which a permeability value of 2×10^{-21} m^2 was found. These values were in agreement with hydraulic conductivity data presented by Villar (2002), although in the lower range of this data set (Fig. 4-9 lower right).

All thermo-hydraulic parameter values are compiled in Tab. 4-4.
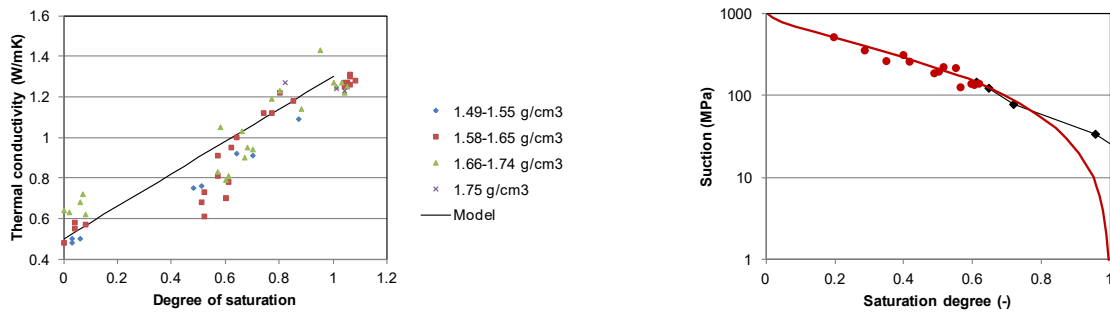
Fig. 4-8:   Adopted functions (lines) for thermal conductivity (left) and water retention curve (right).

Experimental saturation degree values (dots) calculated for a dry density of 1'700 kg/m^3.
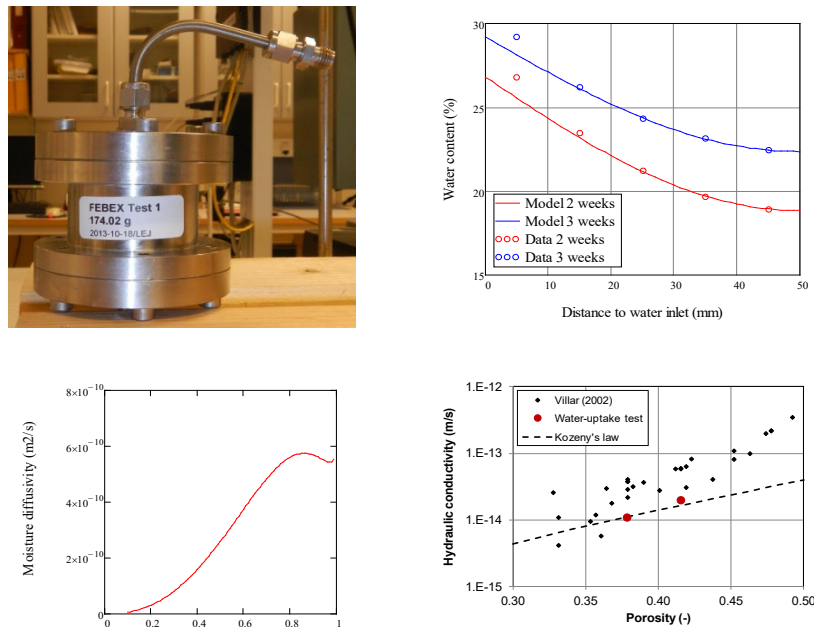
Fig. 4-9:   Adoption of intrinsic permeability from water-uptake tests.

Equipment (upper left), and experimental results and evaluation of diffusivity values (upper right). Evaluated diffusivity for calibrated permeability value (lower left). Comparison of evaluated values (red dots) with independent hydraulic conductivity data (black dots) presented by Villar (2002), lower right.

The adoption of the mechanical parameter values basically followed the same strategy as in the data report for the SR-Site (Åkesson et al. 2010), although this was based on tests on MX-80 bentonite. The elastic mechanical parameters were essentially the same as for buffer rings. The suction dependency of the elastic modules (κ_i and κ_s) were, however, slightly modified due to the extensive dehydration in this case (Fig. 4-10, upper left). It should also be noted that the pressure dependence of the κ_s modulus was modified by Åkesson et al. (2010) with an built-in swelling pressure relation, so that void ratio dependence was incorporated in the κ_s modulus (Fig. 4-10 upper right):

$$\kappa_s(p',e) = \kappa_{s0}f(p',e)$$

$$f(p',e) = \begin{cases} 1 & \text{if } p' < p_{ref} \\ 10^{-20} & \text{if } p' > p_{swell}(e) \\ 1 - \dfrac{\ln p' - \ln p_{ref}}{\ln(p_{swell}(e)) - \ln p_{ref}} & \text{otherwise} \end{cases} \tag{4-5}$$

This means that the swelling stops (i.e. $\kappa_s = 0$) precisely when the mean stress reaches the defined swelling pressure for the current void ratio. The following swelling pressure curve was used:

$$\log^{10}(p_{swell}) = c_2 \cdot \rho_d^{\,2} + c_1 \cdot \rho_d + c_0 \tag{4-6}$$

with the following coefficients (p_{swell} in kPa): $c_0 = -1.74$; $c_1 = 4.12 \times 10^{-3}$; $c_2 = -3.94 \times 10^{-7}$. Note that the relation between the dry density and the void ratio used here was based on the particle density for MX-80 (2'780 kg/m^3). This line is shown in Fig. 4-10 (lower left) together with swelling pressure data for FEBEX bentonite presented by Villar (2002).

The adoption of the *plastic mechanical parameter value* was also based on this swelling pressure curve. The lambda is calculated as an average module between two points on the swelling pressure curve:

$$\lambda = -\frac{e_i - e_f}{\ln(p_{swell}(e_i)) - \ln(p_{swell}(e_f))} \tag{4-7}$$

In this case, a value of 0.2 was adopted for a case in which e_i and e_f are equal to 1.25 and 0.709, respectively (Fig. 4-10, lower left).

The yield surface is described by the following relation (Fig. 4-10, lower right):

$$q^2 = M^2(p' + p_s)(p_0^* - p') \tag{4-8}$$

The tensile strength (p_s) and the critical state parameter (M) are parameters, whereas p_0^* is a hardening variable. The tensile strength (p_s) is regarded to be a void ratio dependent quantity and is derived from the original parameter value adoption by Åkesson et al. (2010). The net mean stress at the critical state point is assumed to be equal to the swelling pressure, ($p' = p_{swell}$). From this it follows that the initial value of p_0^* can be calculated as:

$$p_0^* = p_s + 2 \cdot p_{swell} \tag{4-9}$$

The von Mises stress at the critical state point is assumed to be equal to the von Mises stress at failure in triaxial compression tests which can be described with the empirical relation:

$$q_f = a \cdot p_{swell}{}^b \tag{4-10}$$

were $a = 2.45$ and $b = 0.77$ (for stresses given in kPa). The critical state line parameter can thus be calculated as:

$$M = \frac{a \cdot p_{swell}{}^b}{p_{swell} + p_s} \tag{4-11}$$

These parameters were adopted for a target void ratio, corresponding to the homogenized dry density 1'600 kg/m³, in this case a void ratio of 0.709 for which $p_{swell} = 8.2$ MPa and $p_s = 2.6$ MPa.

All mechanical parameter values are compiled in Tabs. 4-5 and 4-6.
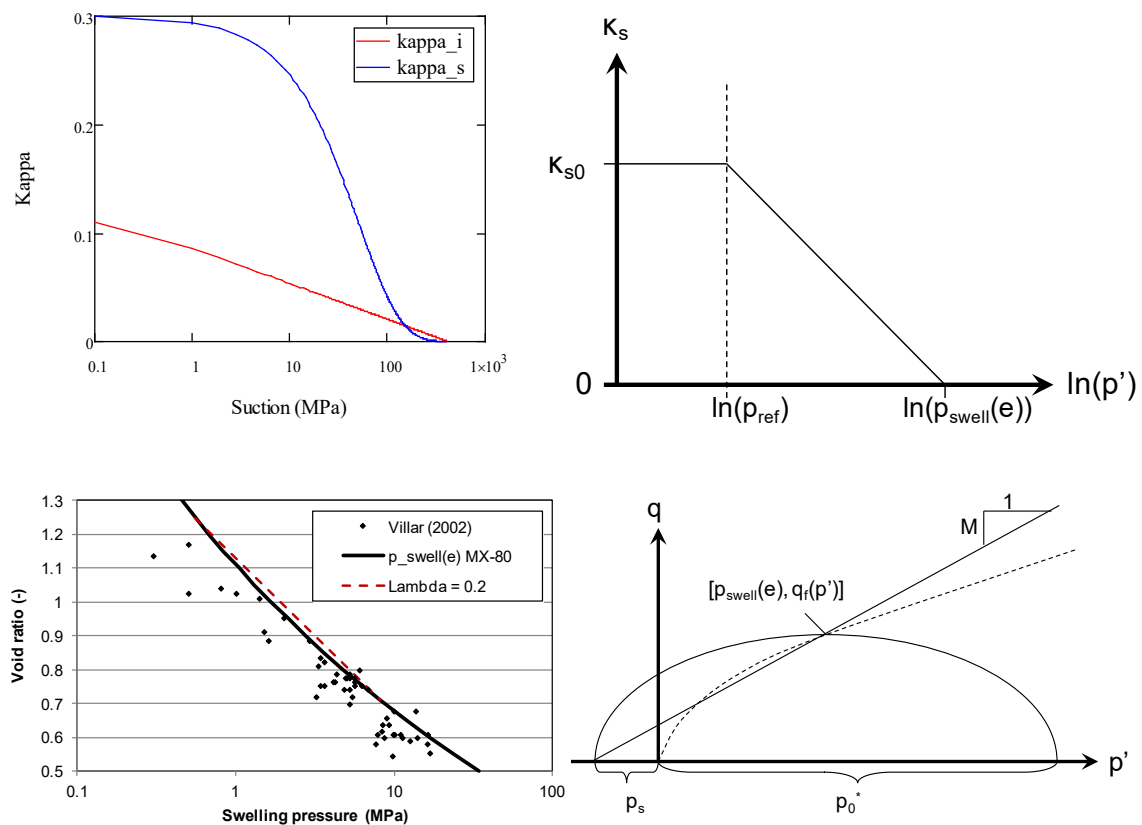
Fig. 4-10:   Adopted functions for elastic parameters (upper row).

Swelling pressure: data (black dots), function (black line) and lambda modulus (red dashed line, lower left). Adoption of yield surface from swelling pressure, yield strength value, and empirical von Mises value at failure (lower right).

Tab. 4-4:   Thermo-hydraulic parameter values.

Thermal conductivity	Specific heat for solid	Intrinsic and relative permeability	Vapour diffusion tortuosity	Water retention curve	Particle density
$\lambda_{dry} = 0.5$ $\lambda_{sat} = 1.3$ (W/mK)	c = 1'091 (J/kgK)	$k_0 = 1.1E\text{-}21$ (m^2) $n_0 = 0.378$ (-) $k_r = S_r^3$ (-)	$\tau = 0.8$ (-)	$P_0 = 22.5$ (MPa) $\lambda = 0.09$ (-) $P_d = 1'100$ (MPa) $\lambda_d = 2.1$ (-)	$\rho_s = 2'735$ (kg/m^3)

Tab. 4-5:   Elastic parameter values.

Porous elasticity	Swelling modulus	Poisson's ratio
$\kappa_{i0} = 0.12$ (-) $\alpha_i = 0$ $\alpha_{ils} = -0.12$ $K_{min} = 20$ (MPa)	$\kappa_{s0} = 0.3$ (-) $\alpha_{ss} = -0.02$ (-) α_{sp} * $p_{ref} = 1$ (MPa)	$v = 0.2$ (-)

*   The α_{sp}-parameter is replaced with an inbuilt swelling pressure relation.

Tab. 4-6:   Plastic parameter values.

Plastic stress strain modulus	Critical state line parameter	Tensile strength	Pre-consolidation stress	Non-associativity parameter
$\lambda_0 = 0.2$ (-) r = 0 (-) $\beta = 0$ (MPa^{-1})	M = 0.234 (-)	$p_{s0} = 2.6$ (MPa) k = 0 (MPa^{-1})	$p_0^* = 19$ (MPa) $p_c = 1$ (MPa)	$\alpha = 0.5$ (-)

4.3.4   Gap material

For the gap material, a bi-linear elasticity model was used (Fig. 4-11). Two Young modulus values were adopted in this way (one low and one high): $E_O = 0.1$ MPa and $E_C = 1'000$ MPa. The volumetric strain limit, $\varepsilon_{v,limit}$ (for changing the elastic modulus) was calibrated to result in a displacement of 28 mm, and was found to be 0.44 for the chosen geometry. No other parameter values for the gap material had any influence on the model results.

4.3.5   Compressibility of water

It should be observed that Code_Bright defines the liquid density as a function of the liquid pressure and the temperature, and therefore has a specified value for liquid compressibility and thermal expansion. However, this liquid compressibility is also used for unsaturated conditions, for which very high negative liquid pressures can be prevalent, which means that the liquid density can get very low if tabulated values for the compressibility of water is used. Since no material with water saturated conditions were included in this model, it was considered safe to use a very low compressibility value (10^{-8} MPa^{-1}) in this case. This meant, for instance, that the initial liquid density was very close to the tabulated value for water even though the initial suction was 125 MPa.

4.4   Model outcomes (impact of heater switch-off, sensitivity analysis)

4.4.1   Evolution of relative humidity and radial stresses

The evolution of relative humidity was evaluated for three radial positions (0.52, 0.81 and 1.06 m), and these results were compared with sensors data from Section F2 (Fig. 4-12). The model showed a fairly good agreement with experimental data, although it displayed trends which were slightly too slow in the inner part.

The evolution of radial stresses was evaluated at the inner and outer radii, and these were found to be almost identical to each other (Fig. 4-13). These trends were also compared with sensors data from Section F2, and this showed that the model was quite similar to the data from one of the sensors (PSF2-01) in the lower part of the section (Fig. 4-13). The model showed, however, a lesser agreement with the other sensors which displayed significantly lower stress levels.

4.4.2   Distributions of water content and dry density

The distribution of water content and dry density was evaluated for four points in time (after 0, 135, 1962 and 6'710 days). The results for day 1962 can be compared with data from the first dismantling (Fig. 4-14). The modelled water content values showed a quite good agreement with experimental data, although the dehydration in the inner part appeared slightly too extensive. Similarly, the modelled dry density also showed quite a good agreement, but the shrinkage in the inner part, and the swelling in the outer part, was slightly too extensive. The results for day 6710 constitute a blind prediction for the outcome of the dismantling of the bentonite around Heater #2 which was performed in 2015. It can be seen that the model results for day 6710 are not very different from the results for day 1962.
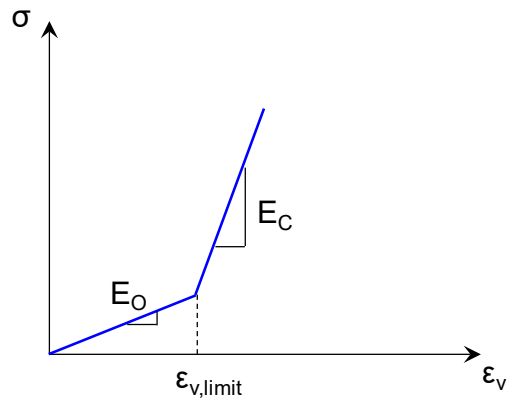
Fig. 4-11:   Schematic behaviour of bi-linear elastic material model.
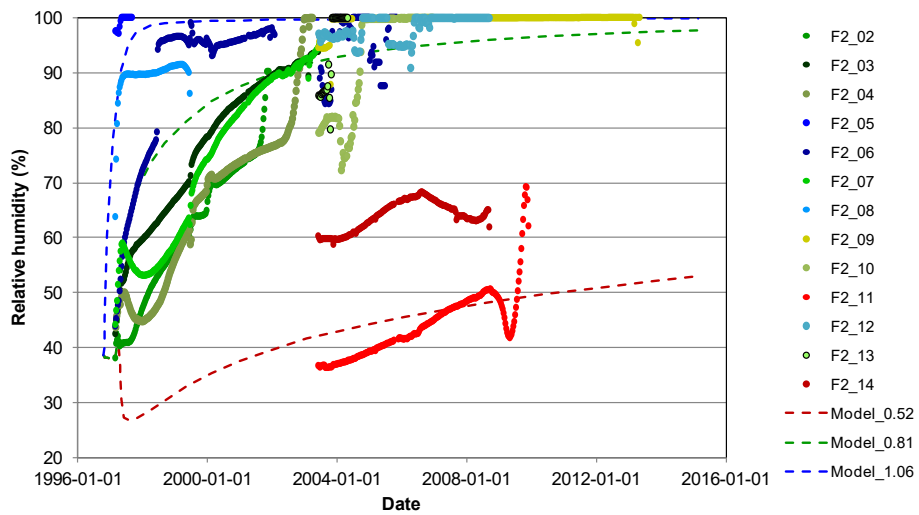
Fig. 4-12:   Modelled (lines) and measured (dots) evolution of relative humidity in Section F2.
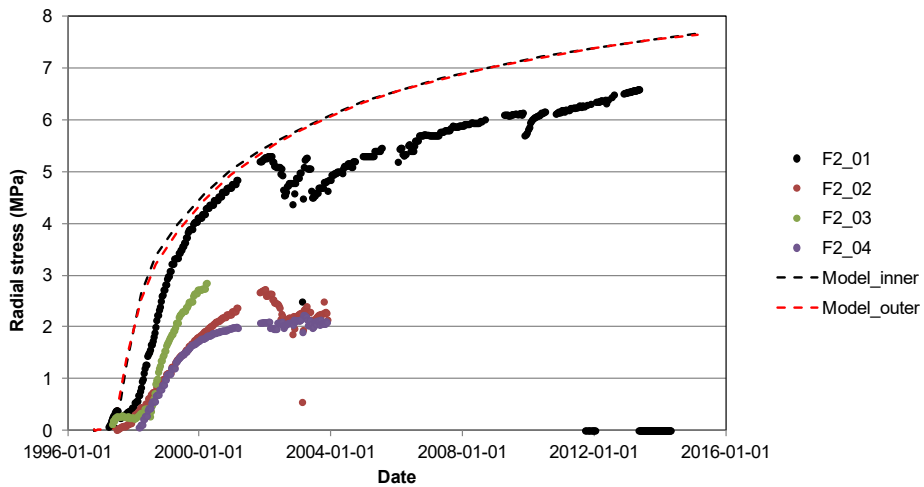
Fig. 4-13:   Modelled (lines) and measured (dots) evolution of radial stresses in Section F2.
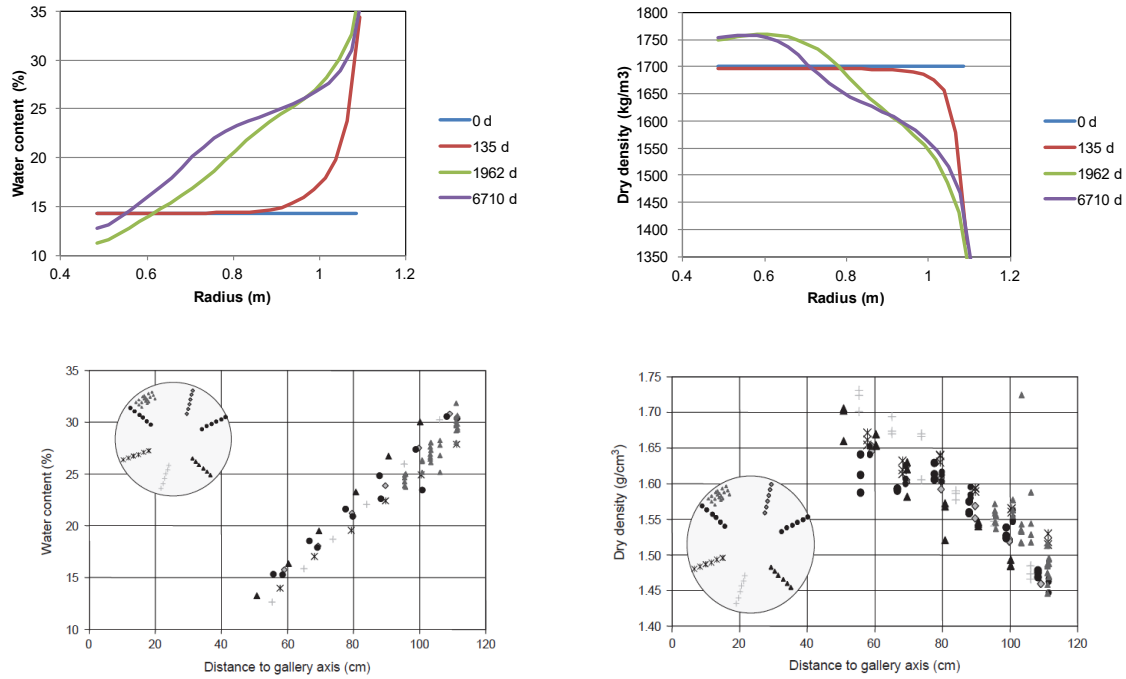
Fig. 4-14:   Modelled (upper graphs) and measured distributions at the time of the 1st dismantling (1962 days) (lower graphs, from Villar et al. 2005) of water content (left) and dry density (right) in Section F2.

4.4.3   Stress paths

An evaluation of stress paths (void ratio vs net mean stress) for three different nodes is shown together with the used swelling pressure curve in Fig. 4-15 (left). It can be noted that the model shrinks slightly at the inner node (no. 56), whereas it also swells to some extent at the centre node (no. 30) where it reaches the swelling pressure curve. In contrast, the model swells dramatically at the outer node (no. 8) before it reaches the swelling pressure curve, and is then compressed beyond this curve. However, the slope is not as steep as the adopted lambda module in Fig. 4-10 (lower left). A tentative explanation for this is illustrated in Fig. 4-15 (right), which shows a stress path in the q-p plane (i.e. von Mises stress vs. net mean stress) for the node in question. At first, the stress path shows a very rapid increase of q (due to the build-up of axial and tangential stresses). Then it hits the yield surface, which contracts due to dilatation. Then follows a period with elastic conditions during which the radial stresses surpass the axial and tangential (with resulting low q values). After this, the stress path hits the yield surface again, and finally it consolidates and pushes the yield surface outward slowly. The interpretation that can be made is that since the yield surface is hit at a relatively high q level, this means that the effective slope in e-ln(p) plane is significantly lower than the adopted lambda module. This in turn explains why the consolidation is not as extensive as it should be, and ultimately why the low dry densities in the outer part do not increase with time (Fig. 4-14 upper right).

4.5   Interpretation of the results

4.5.1   Driving processes

Two main driving forces can be identified:

i)   *The heating power and the non-isothermal conditions*. The most important consequence of this is the moisture redistribution, with dehydration in the warm parts and hydration in the cooler parts, which in turn will lead to shrinkage and swelling, respectively. The thermal expansion of water has some minor influence on these processes, whereas the corresponding expansion of the solids appears to have a negligible influence.

ii) *The bentonite's high affinity for water and the water supply from the rock.* This will lead to water-uptake, which in turn will lead to swelling/consolidation processes and a build-up of swelling pressure.

4.5.2   Modelled distributions of dry density and water content and potential improvements

The presented model shows a fairly good agreement with experimental data although it displays a slightly too extensive dehydration/shrinkage in the inner part, and too low dry density levels in the outer part (Fig. 4-12 – Fig. 4-14). The agreement could possibly be improved through modification of some elements of the model. For instance, the dehydration and shrinkage in inner part could be reduced through modification of some of the transport coefficients (notably the intrinsic permeability and its porosity dependence, as well as the vapour diffusion tortuosity). A similar effect could be achieved through modification of the boundary conditions (thermal and hydraulic). The low dry density level in the outer parts could be increased through modification of the plastic parameters and the approach with one major gap at the rock wall. Such modifications could very well be justified. For instance, a back-analysis of data from laboratory tests presented by Pintado et al. (2002) identified a vapour diffusion tortuosity value which was significantly lower than the value adopted for this model. Still, it was outside the scope of this task to make a systematic analysis of such modifications.
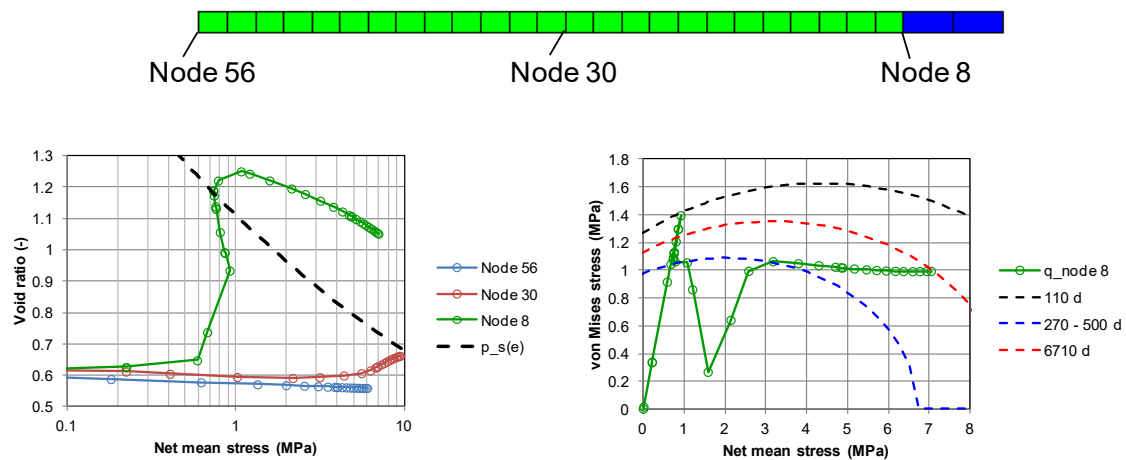
Fig. 4-15:   Stress paths for three nodes in e-lnp plane (left) and for one node i q-p plane (right).

4.5.3   Progress made in this exercise, remaining uncertainties

The validity of the different elements of the used material model can be assessed in the following way: i) The *thermal* material model is generally found to be simple and in good agreement with experimental data. In the presented model, this was, however, circumvented with constant temperature boundaries and therefore these only had a minor influence on the results. ii) The *hydraulic* material model for *isothermal* conditions has also reached a fairly high level of validity, and this was used by adopting the intrinsic permeability value from the evaluated moisture diffusivity value. Still, it should be noted that the retention curve used was adopted for the initial dry density of the blocks, and this may therefore not be fully accurate since some parts of the model have undergone swelling or shrinkage. iii) The *hydraulic* material model for *non-isothermal* conditions, which describes the moisture redistribution through vapour transport, still appears to be a fairly weak model. The influence of this appears to be less significant in a problem like this, with free access of water, than in a corresponding problem with a very low water inflow. Still, this is the main uncertainty for predicting the time-scale of the re-saturation. iv) The *mechanical* model is generally found to be the weakest element in a fully-coupled THM model. Nevertheless, some mechanical aspect can be captured to some extent (see Fig. 4-13 and 4-14), although the prospects for simulating the complex processes (e.g. swelling/consolidation cycles with hysteretic effects) with the used constitutive laws appears to be limited.

4.5.4   Consequences for the early repository evolution viewpoint

If the bentonite installation would be left in place, then this would mean that the water uptake in the bentonite would continue and eventually it would reach full water saturation. This would lead to a less extensive heterogeneity through the homogenization process. Nevertheless, some level of heterogeneity is expected. According to the current understanding, this is caused by the hysteretic behaviour of the retention properties/swelling pressure. This is currently investigated in the homogenization task within the EBS Taskforce.

5   Joint interpretation of the modelling results

5.1   Scope of the modelling benchmark

Mathematical models and numerical codes are essential tools needed to assess the performance of deep geological repositories over long time periods. Model analyses of the entire repository system or components thereof are required to address transport processes related to radionuclide release, but also to get insight in the thermo-hydro-mechanical (THM) evolution of the repository near-field. In the context of the FEBEX-DP project, the repository near-field comprises the waste canister, the buffer system built of bentonite blocks and the excavation damaged zone (EDZ), enclosed by the intact host rock. The representation of coupled THM processes, together with complex model geometries and the associated boundary conditions pose major challenges for the mathematical models and their implementations in numerical codes. Code verification and model validation exercises are common methods to build confidence in the capabilities of THM codes. Recalling the fact that the inherent complexity of coupled THM process models prevents in most cases the use of analytical solutions for verification and validation (V&V) tests, benchmark exercises have proved to be of value for confidence building. It is essential to perform a benchmark study that can be used for model comparisons and for assessing the reliability and accuracy of the different numerical models. In this context, the simulations presented in the previous three chapters formulate an excellent benchmark. The comparison of the modelling results allows for the understanding of the differences in the model concepts and numerical approaches, eventually building confidence in the predictive capability of the thermo-hydro-mechanical (THM) models.

This chapter provides an overview of the modelling teams, their numerical codes and applied model formulations (Section 5.2). Thereafter, the modelling strategies and general modelling approaches are given (Section 5.3), as well as an evaluation and comparison of the numerical results of the three modelling studies (Section 5.4). An attempt is made to interpret the differences and similarities from the benchmark studies (Section 5.5). Finally, Section 5.6 gives some concluding remarks.

5.2   Modelling teams, codes and models

Fig. 5-1 illustrates an overview of the modelling teams and corresponding models presented in the previous chapters (CIMNE, Spain; EPFL, Switzerland; Clay Technology, Sweden). CIMNE and EPFL were involved in modelling activities related to the FEBEX experiment, including material parameter calibration, model set-up, and preliminary evaluations up to the first dismantling stage. Readers are referred to the publications of Sánchez et al. (2012) and Dupray et al. (2011) for more details about the earlier model analyses by CIMNE and EPFL, respectively. In contrast, Clay Tech had to set-up a new model for simulating the FEBEX-DP experiments.

As shown in Fig. 5-1, two numerical codes were used in the three studies: (i) Code_Bright, which was developed at UPC (Gens & Olivella 2001; Olivella et al. 1994) has been used by CIMNE and Clay Tech, (i) Lagamine, developed at ULG (Collin 2003; Gerard et al. 2008) was used by EPFL. The constitutive models chosen to describe the mechanical behaviour of the bentonite, differ between each team as well, namely BBM for CIMNE and Clay Tech, and ACMEG for EPFL. According to Fig. 5-1 the BBM-FB represents the BBM model which is calibrated to non-isothermal behaviour of FEBEX bentonite, whereas the BBM-80 model is calibrated for MX80 bentonite, neglects the thermal expansion of bentonite mineral but accounts for the thermal expansion of water (Börgesson et al. 1995). This section gives a brief

introduction to the numerical codes, followed by a comparison of formulations and assumptions in the fundamental THM models of the two numerical codes and in their constitutive models.
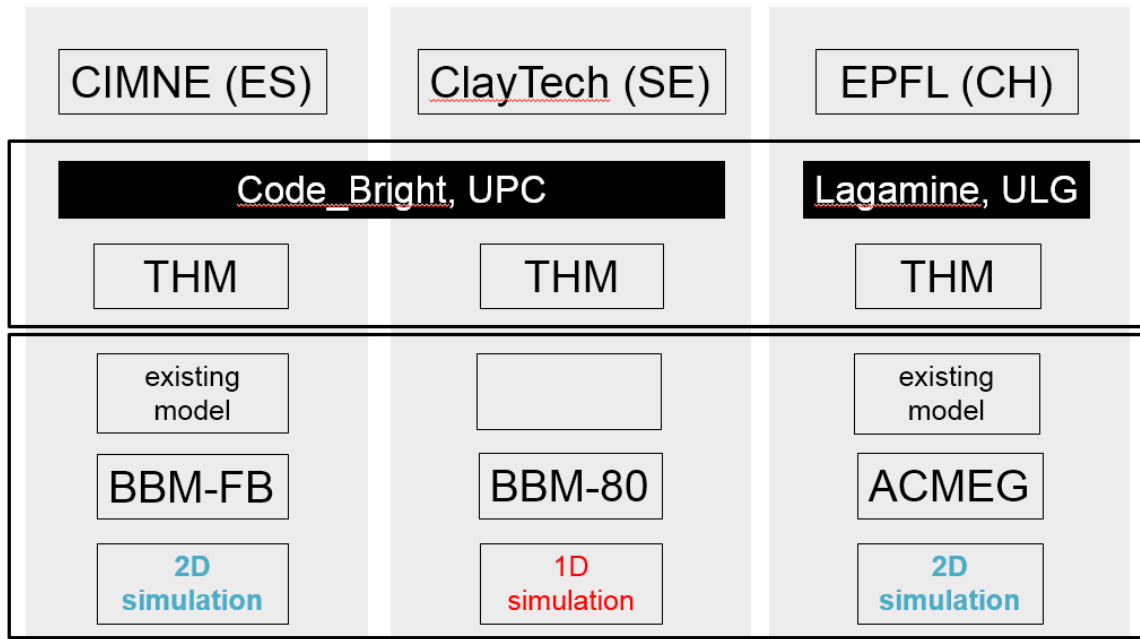
Fig. 5-1:   Overview of the modelling teams, numerical codes, coupled model (THM: thermal-hydro-mechanical coupled processes), availability of earlier works, mechanical constitutive models and conceptual model dimension.

5.2.1   Coupled THM formulations in Code_Bright and Lagamine

Lagamine was initially developed for modelling of metal forming process. It can handle large deformations/displacements and rigid body motions, relying on the updated Lagragian approach (Charlier et al. 2011). Code_Bright was initially developed for the coupled analysis of saline media with a classical small deformation approach. In this particular study, the application of both codes is focused on simulations of non-isothermal multiphase flow in deformable porous media for the repository assessment. The theoretical THM frameworks are similar, drawing on the three main balance equations: (i) mass balance, (ii) energy balance and (iii) momentum balance equations. The state variables chosen in both codes to describe the state of the material are water phase pressure p_w, gas phase pressure p_g, temperature T and displacement field $\boldsymbol{u}$.

Mass balance

Both codes adapt the compositional approach by formulating the mass balances equations of each chemical species (water, air and mineral) rather than of the phases. Using this approach, the phase exchange terms are taken into consideration implicitly.

The chemical species *water* is presented in liquid and gaseous phases. The mass balance of the *water* expressed in Eq. (3-2) and Eq. (A1-1) are equivalent. Omitting the terms that are neglected for the simulation of FEBEX-DP by the three teams, the mass balance equation of *water* reads as:

$$\frac{\partial(nS_w\rho_w)}{\partial t}+\mathbf{div}\left(\rho_w\mathbf{q}_w\right)+\frac{\partial\left(\rho_v n(1-S_r)\right)}{\partial t}+\mathbf{div}\left(\mathbf{i}_v\right)=0 \tag{5-1}$$

where the terms $\mathbf{q}_w$ represents the advective water flux, governed by Darcy's law and the terms $\mathbf{i}_v$ represents the non-advective water flux in the gaseous phase (i.e. the diffusion of vapour in the air), governed by Fick's law.

The gas pressure is assumed constant in this particular study. The equation of the mass balance of *air* is therefore not used.

Energy balance

The assumption of the thermal equilibrium between phases is made by both codes. Consequently, only one equation is required to establish the energy balance for the whole medium. The energy balance in Lagamine shown in Eq. (3-4) is expressed in terms of the enthalpy whereas the energy balance in Code_BRIGHT is expressed in terms of internal energy as shown in Eq. (A1-2). Although the two codes use different extensive properties to describe the energy balance, the final equations used in the simulations are most likely equivalent as described hereafter. A general form of the energy balance equation is expressed below, which is adopted in a similar way to that of Lagamine:

$$\underbrace{\frac{\partial(1-n)\rho_s h_s + nS_r\rho_w h_w + n(1-S_r)\rho_g h_g + n(1-S_r)\rho_v L}{\partial t}}_{\text{Heat storage}} + \underbrace{\underbrace{\mathbf{div}\left(\mathbf{\Gamma}\right)}_{\text{conduction}}+\underbrace{\mathbf{div}\left(\mathbf{f}_\Gamma\right)}_{\text{convection}}}_{\text{Heat transfer}}=0 \tag{5-2}$$

where h_s, h_w and h_g represent specific enthalpy of solid, liquid and gaseous phase respectively if they are expressed in terms of the product of temperature variation and the specific heat capacity at constant pressure, i.e., $h=c_p\,\Delta T$. They could represent specific internal energy if they are expressed in terms of the product of temperature variation and the specific heat capacity at constant volume, i.e., $h=c_v\,\Delta T$. The parameter L is the latent energy of the vapour.

The use of the internal energy requires the specific heat capacity at constant volume, which is actually difficult to measure for liquids and solids. Consequently, the specific heat capacity at constant pressure is used in Code_BRIGHT (Gens & Olivella 2001). That is to say that the energy conservation of Code_BRIGHT is also expressed with enthalpy rather than internal energy for liquids and solids. For the gaseous phase, the latent energy due to vaporisation is taken into account implicitly by adding the latent energy, L, as a constant in the expression of the specific internal energy of gas, Eg, in Code_BRIGHT, while it is expressed explicitly with the term $n(1-S_r)L$ in Lagamine as shown in Eq. (5-2).

In addition, both codes adopt the same physical laws to describe heat conduction and convection. The energy balance equations of both codes are, therefore, most likely equivalent.

Momentum balance

The momentum balance equations are the same for both codes.

In summary, the THM theoretical models of both codes are similar. Both solve the set of balance equations simultaneously to allow for solving the problem in a fully coupled manner. Both adopt the Newton-Raphson method to solve the non-linear problem and finite differences to discretise the equations in time.

5.2.2 Constitutive models

The three teams adopt similar sets of constitutive formulations for thermo-hydraulic processes which are not addressed in detail in this report. In the following paragraph, a brief summary is given on the two main mechanical constitutive formulations, BBM (Alonso et al. 1990) and ACMEG (François & Laloui 2008). The difference in terms of model calibration and parameter assignment is highlighted in Section 5.3

Both constitutive models BBM and ACMEG are based on elasto-plastic frameworks, which are used to capture mechanical responses of bentonite to hydration and temperature variations. Both models are formulated in terms of stress invariants, suction and temperature. Both are capable of taking into account the thermal-elasticity and irreversible deformations due to loading increments or wetting (collapse compression). ACMEG is also able to take into account the thermal collapse. The major difference between the two models is the adaptation of different effective stress principles: BBM is formulated in terms of net stress and suction whereas ACMEG uses a generalized formulation of effective stress and suction. This subject is still one of the most fundamental scientific questions in the mechanics of porous media, leading to unsettled debates on validity and applicability. In this regard, the comparison of these two constitutive models is rather complex and beyond the objective of this study. For a detailed analysis, the reader is referred, for example, to Laloui & Nuth (2009) and Nuth & Laloui (2008).

5.3 Modelling strategies and modelling approaches

In this section, the comparison of the modelling strategies and approaches is presented. The modelling approaches in this task can be grouped as follows:

(i) a detailed approach adopted by CIMNE and EPFL which deal with a two-dimensional THM fully coupled simulation

(ii) a simplified approach with one-dimensional modelling by Clay Tech

The first approach is presented in a more detailed way by comparing the EPFL and CIMNE configurations, whereas the approach of Clay Tech is briefly summarized and the consequences of the geometrical simplification are emphasised. The differences of the modelling approaches between a 1-D and a 2-D configuration are highlighted at the end of this section.

5.3.1 2-D approach

Conceptual model and main assumptions

CIMNE and EPFL adopt a 2-D axisymmetric longitudinal section of the horizontal disposal drift, as shown in Fig. 2-1 and in Fig. 3-3 respectively. The domain considered by EPFL is 10 meters larger in both longitudinal and radial directions than that considered by CIMNE. The presence of the Lamprophyre dyke is not explicitly implemented in the models; the justification is given in Gens et al. (2009). Non-consideration of the Lamprophyre dyke allows for the 2-D representation as the drift is axisymmetric with respect to the horizontal axis of the disposal drift. However, an unavoidable limitation of a horizontal axisymmetric representation is the exclusion of gravity. Gravity is the main driving force for certain interactions between adjacent materials, such as stress development at heater-bentonite-liner interfaces, gap opening and etc. But, gravity would not play a significant role within the bentonite blocks and host rock, in flow behaviour which is driven mainly by the important pressure gradient, or in stress variation which is dominated by heating and hydration. The investigation herein focuses, to some extent, on the key phenomena occurring within the bentonite. In this regard, the neglect of gravity is acceptable.

The concrete plug, host rock (granite), bentonite buffer and two heaters are included in both conceptual models. Additionally, CIMNE considers the existence of a steel liner surrounding the heaters. Although gaps would play an important role in stress development and in flow and heat transfer, both teams assume that there is no gap between adjacent materials, i.e., between the host rock and the bentonite, between the bentonite and the heaters, and between the liner and the heaters. A full contact between bentonite blocks is also assumed. Nevertheless, the presence of gaps among the bentonite blocks is taken into account by adapting the initial density $\rho_0 = 1.70$ Mg/m^3 of the bentonite to $\rho_0 = 1.60$ Mg/m^3. This approximation can introduce some uncertainty in the model predictions of the bentonite's mechanical response.

The history of construction and operation phases of the FEBEX experimental set-up is represented in the THM models in a simplified manner. Given the high relevance of the test history for the simulation of the experiment's progress, most essential sequences are reproduced in both studies. Starting from tunnel excavation, the long-term stage of subsequent equilibration, two dismantling steps after each switch-off of the heater, and impacts of these operations on the repository performance are investigated in detail. The simulated sequences and the main relevant THM impacts are summarized below:

- Tunnel excavation – HM modelling
  (a) Redistribution of stresses around the tunnel
  (b) Redistribution of pore water pressure around the tunnel

- Ventilation stage – HM modelling
  (a) Pore pressure release
  (b) Stresses re-equilibrium

- Construction and equilibrium stage – THM modelling
  (a) Canister emplacement
  (b) Bentonite block installation
  (c) Concrete plug-in
  (d) Limited amount of isothermal bentonite hydration

- Heating stage – THM modelling
  (a) Thermal-hydro-mechanical coupling
  (b) Hydration in the bentonite from the surrounding rock
  (c) Swelling development
  (d) Vapour transfer
  (e) Heating effect in the near field

- Switch-off and dismantling phases – THM modelling
  (a) Cooling-induced stress reduction
  (b) Swelling pressure release in the bentonite due to the dismantling

Material groups, THM properties and formulations

The model implementations by the two teams are representing the FEBEX experiment in great detail in terms of both model geometry and temporal evolution of the experiment. The main difference arises in constitutive formulations and certain material properties. Tab. 5-1 summarizes the main THM properties and formulations that govern the physical processes.

The heaters, the liner and the host rock are considered as elastic materials. The THM properties are taken as averaged values based on literature. For the intrinsic permeability of the granite there are three orders of magnitude difference between the EPFL and CIMNE setting. As both teams assume a fully saturated state of the granite during the whole experiment, no desaturation is possible. The water supply to the bentonite therefore does not depend on the flow in the granite. The other properties are within the same order of magnitude, but have different values. Depending on the loading condition, these differences could nevertheless be non-negligible. For example, the thermal stress variation is proportional to the combination of the Young modulus, thermal expansion coefficient and Poisson's ratio, $E\alpha_s/(1-2v)$, when an elastic material is subjected to a given temperature variation under deformation constrained conditions. After the numerical application, the thermal stress increase within the host rock will be 46 % higher when considering the EPFL parameter settings compared to the CINME setting. From a thermo-mechanical point of view, this could be a potential reason for the difference in the stress development at the bentonite-granite interface.

In the bentonite, liquid flow is governed by Darcy's law of which the intrinsic permeability is a porosity-dependent parameter in all three studies. As shown in Fig. 5-2, the formulation of EPFL results in the higher bounds of the experimental data; the permeability increases fast with the increase of the porosity whereas the other two feature the lower bound. The permeability varies slightly with respect to the variation in porosity. Upon hydration, a quick increase in the porosity is expected which would have a direct impact on the permeability.

Fig. 5-2 illustrates the variation of the thermal conductivity with saturation and porosity. Fourier's law is adopted to describe the heat conduction. CIMNE and Clay Tech formulate saturation-dependent thermal conductivities, whereas EPFL adds the dependency of the porosity. An overall agreement exists between the three models.

On the mechanical side of the problem, the simulation of the confined swelling behaviour of bentonite is the most important feature to reproduce. Both teams incorporate the experimental measurement data of the FEBEX bentonite to calibrate the chosen constitutive models, i.e., BBM and ACMEG. Both state a good agreement between prediction and experiments.
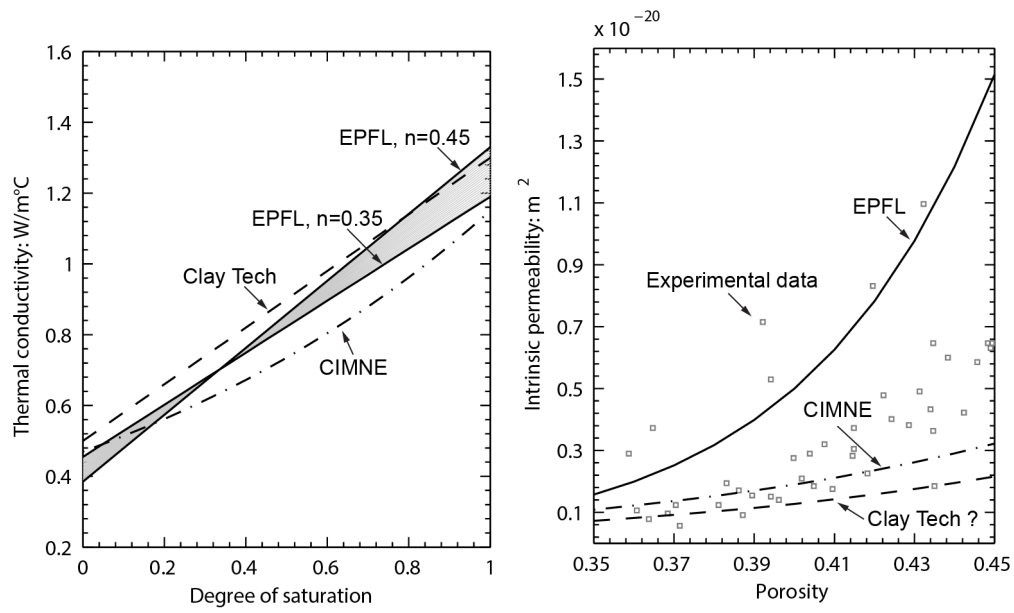
Fig. 5-2:   Model responses of the thermal conductivity formulation (left) and Kozeny–
            Carman model (right) adopted by the three teams.

Tab. 5-1:   Parameters used by CIMNE and EPFL.

Element in the model	CIMNE	EPFL
Material groups, their THM models and initial properties		
Heaters	Solid material & thermal-elasticity [Info not available]	Solid material & thermal-elasticity
Liner	Elastic [Info not available]	Not present
Concrete plug	Saturated material & thermal-elasticity $K = 25'100$ MPa ($E = 32'161$ MPa) $G = 12'500$ MPa ($v = 0.30$) $n_0 = 0.05$ $\alpha_s = 6.9e\text{-}6$ K^{-1} $\lambda_{sat} = 1.40$ W/mK	Saturated material & thermal-elasticity $K = 16'667$ MPa ($E = 30'000$ MPa) $G = 12'500$ MPa ($v = 0.20$) $n_0 = 0.15$ $\alpha_s = 3.3e\text{-}6$ K^{-1} $\lambda_{sat} = 1.7$ W/mK
Host rock (Granite)	Saturated material & thermal-elasticity $K = 39'200$ MPa ($E = 36'330$ MPa) $G = 13'500$ MPa ($v = 0.35$) $n_0 = 0.01$ $\alpha_s = 7.8e\text{-}6$ K^{-1} $\lambda_{sat} = 3.3$ W/mK $k_0 = 8.8e\text{-}21$ m^2	Saturated material & thermal-elasticity $K = 55'556$ MPa ($E = 50'000$ MPa) $G = 18'519$ MPa ($v = 0.35$) $n_0 = 0.01$ $\alpha_s = 8.3e\text{-}6$ K^{-1} $\lambda_{sat} = 3.34$ W/mK $k_0 = 4.5e\text{-}19$ m^2
Bentonite blocks	Unsaturated material THM-BBM $\rho_0 = 1.60$ Mg/m^3 $n_0 = 0.40$ $\alpha_s = 1.5e\text{-}4$ K^{-1} $\lambda = f(S_r)$ see figure $k_0 = 1.9e\text{-}21$ m^2 see figure	Unsaturated material THM-ACMEG $\rho_0 = 1.60$ Mg/m^3 $n_0 = 0.4074$ $\alpha_s = 7e\text{-}4$ K^{-1} $\lambda = f(n,S_r)$ see figure $k_0 = 5e\text{-}21$ m^2 see figure

5.3.2   1-D Approach

Conceptual model and main assumptions

Clay Tech adopts two models based on a 1-D axisymmetric configuration which represents a bentonite slice at hot Section F2, as shown in Fig. 4-1. The experimental history mentioned above is neglected. The models focus on thermal impacts on the hydraulic and mechanical processes only within the bentonite buffer during the heating stage. Given the simplification of the conceptual models, the modelling effort is significantly reduced with respect to the 2-D approaches.

A 2-step modelling approach is adopted:

- Analytical prediction of the temperature field: Temperature simulated at the rock wall is used as the boundary condition for the next step.

- Numerical prediction of bentonite THM behaviour during heating: 1-D axisymmetric model which takes into account the hydro-mechanical behaviour of the bentonite and the effect of the gaps between bentonite blocks.

In relation to the first step, an analytical prediction of the temperature field is initially established. The analytical solution used by Clay Tech is developed for heat transfer in the granite only (a thermal conductivity of 3.6 W/mK is adopted). The conceptual model uses the calculated temperature, in the second step, as a boundary condition in the two 1-D models. The calculated temperature is imposed on the outer boundary, which can introduce some inward-directed heat fluxes that are, however, very limited. In terms of the imposed temperature at the inner boundary, the value is directly taken from the in-situ measurement.

Material groups and THM formulations

One of the two 1-D models adopts a 28-mm-wide bi-linear elastic material as an equivalence to the presence of the gaps between bentonite blocks as illustrated in Fig. 4-7. The gap material was calibrated so that it would allow a displacement (on the inside) of 28 mm, which occurred already after about 100 days of heating. The thermal and boundary conditions are located in contact with the bentonite, on the inside of the gap material, thus no thermo-hydraulic properties were attributed to the gap material.

It is worth noting that unlike the other two modelling teams, Clay Tech adopts the model parameter setting that is attributed to MX80 bentonite instead of FEBEX bentonite. This BBM-80 model does not consider the thermal expansion of bentonite minerals based on the data presented in Börgesson et al. (1995).

The thermo-hydraulic constitutive formulations are very similar to those of the CIMNE, as shown in the comparison in Fig. 5-2

5.4   Comparison of results

The objective of this section is to present results of the three teams evaluated at the same locations and to interpret the differences of model responses starting from the heater switch-off, through the heating phase, to the first dismantling phases. Three THM processes are selected for comparison in a progressive way: thermal, thermal-hydraulic coupling and thermo-hydro-mechanical coupling processes. Important results available in the previous chapters are regrouped hereafter so as to clearly show the differences among the models at similar locations. The interpretation is focused on the fundamental reasons that could explain the different model behaviour, especially the theoretical formulations.

5.4.1   Thermal evolution of the buffer system

Results in terms of temperature

In general, the three models predict the thermal processes well, i.e., the temperature increases due to the heaters switch-on, the cooling down due to the switch-off, and the development of a temperature gradient in the heater near-field match the measurements. As shown in Fig. 2-7 and Fig.3-12, the good agreement of the simulation results with the measured data validates the hypothesis adopted in both studies that the heat transfer is dominated by conduction whereas heat convection is not significant. Furthermore, the analytical solution in Clay Tech's appraisal is derived by considering only heat conduction. Therefore, the three models confirm that the dominant heat transfer mechanism is heat conduction.

However, a small difference is observed between the two 2-D simulations. Fig. 5-3 compares the simulated evolution of temperatures by EPFL and by CIMNE along the sections I and D2 in the bentonite buffer. As can be seen, the thermal system reaches steady state very quickly in both cases as measured in situ. Both models capture the rapid decrease of temperature at Section I after Heater #1 turns off. It can be noted that at Section I, the EPFL model features a lower temperature and captures a sharper temperature decrease than the CIMNE model. The results tend to converge in the radial direction. At Section D2, both models capture the small influence due to the disconnection of Heater #1. But, the EPFL model predicts a higher temperature in the vicinity of Heater #2 than does the CIMNE model. In relation to the measurements, the EPFL result features a higher temperature prediction than the measurements, whereas the CIMNE model predicts a lower temperature than the measured data at this location. Equivalent to Section I, the results converge and agree well with the measurements in both models.
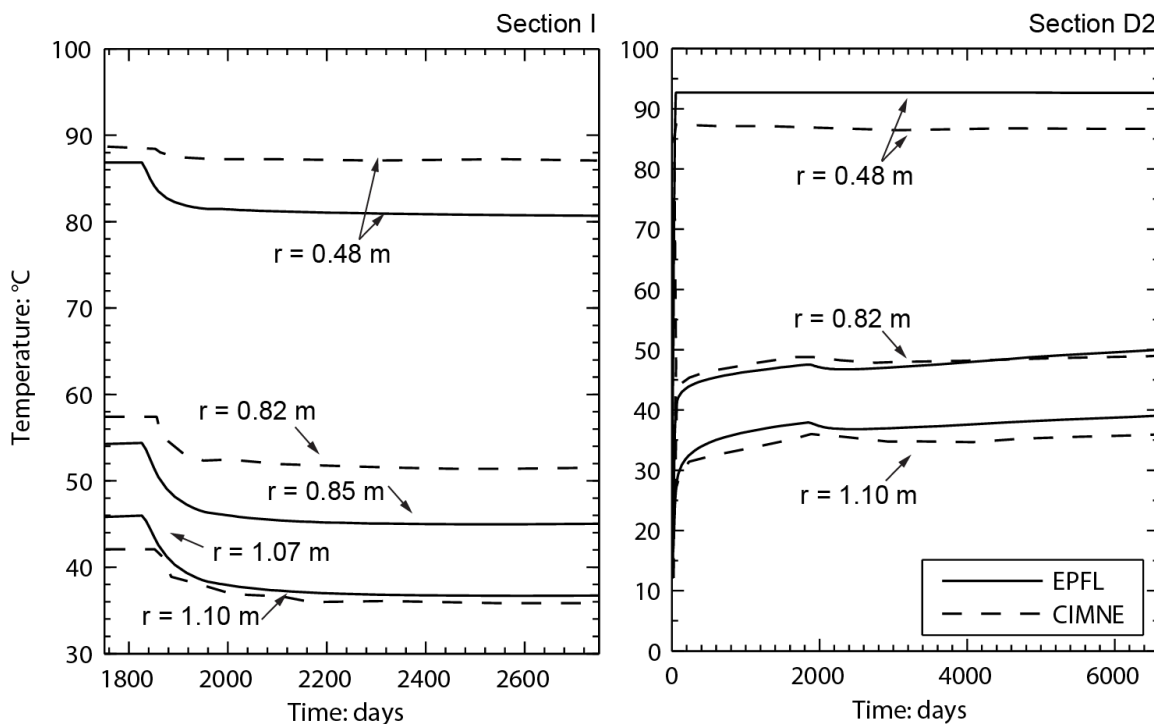
Fig. 5-3:   Simulated evolution of temperatures on the sections I and D2 in the bentonite buffer by CIMNE and EPFL.

Interpretation of the differences

It is worth noting that the heat transfer process is considered to be governed by the heat conduction mechanism in all three models, which are all described by Fourier's law. In other words, the thermal evolution is controlled by the thermal diffusivity. In this particular case, the system reaches the steady state very quickly; therefore, the thermal conductivity is the most important parameter that governs the temperature distribution in the vicinity of the heaters. In this regard, the different coupled formulations of the thermal conductivity lead to different model responses to hydraulic and mechanical loadings. EPFL adopts a hydro-mechanical coupled thermal conductivity formulation whereas the other two teams adopt a hydraulically coupled one. As shown in Fig. 5-2, the thermal conductivity increases nearly by a factor of two

with the increase of saturation from zero to one, as water plays a vital role in the heat transfer mechanism. It can be noted that the EPFL model features a higher thermal conductivity than CIMNE does across most of the range of the possible variation of porosity. This explains why EPFL, in general, predicts higher temperatures in the vicinity of the heaters and a more rapid cooling in response to the dismantling. Especially in a high saturated state where the porosity increases upon wetting, the thermal conductivity consequently increases leading to a higher temperature throughout the model.

In relation to the 1-D model, the temperature function used by Clay Tech is developed by considering only the heat conduction without hydro-mechanical coupling. The good agreement with the measurements suggests that the heat transfer is nearly de-coupled from the mechanical deformation. Together with the consistent results between EPFL and CINME, it can be concluded that the porosity changes are not significant enough to have a major influence on the thermal response. In the second phase of the Clay Tech model, a similar formulation to the CIMNE model is adopted for thermal conductivity, to account for the saturation-dependent behaviour.

5.4.2   Thermo-hydraulic evolution of the buffer system

Results in terms of relative humidity

Fig. 5-4 shows the comparison of simulated relative humidity in sections E1, H, and F2. The responses of the models developed by the three teams are in good qualitative agreement with the measurements. Overall, satisfactory agreement is achieved in terms of the general trend as well as the order of magnitude. It can be noted that in the vicinity of the host rock at the Section E1 and F2, all three models capture that relative humidity increase rapidly just after the buffer emplacement. This is universally followed by a gradual monotonic increase and relative humidity reaches 100 % in a short amount of time. This behaviour reflects that the host rock provides sufficient water for the unsaturated bentonite to rapidly hydrate. The hydration governs the hydraulic processes at the contact of the host rock.

In the immediate vicinity of the heaters, vaporisation incurred by the heating, results in an increase in the relative humidity as predicted in the early heating phase. This is followed by a period of significant decrease during which heating-induced drying effects become more significant than the vaporisation. Later on, relative humidity starts to increase gradually upon hydration from the host rock and the arrival of the vapour front. The behaviour close to the heaters is strongly affected by temperature, as stated by each of the three teams in the analysis.

The predicted relative humidity in Section H of Fig. 5-4 illustrates the hydraulic responses to the switch-off of the Heater #1. In response to the decrease of the temperature, the relative humidity decreases correspondingly due to the restricted vaporisation from the side of Heater #1. Subsequently, during and after the first dismantling, a gradient of vapour concentration develops which leads to a movement of the vapour outwards. This represents a typical diffusive process. At the same time, a temperature gradient develops as well, forming a hotter region at Heater #2 and a cooler region at Heater #1. The vapour moves from the hotter region towards the cooler one, and it condensates into liquid increasing the saturation rate of the bentonite. During this particular period and at this particular location, the thermal-hydraulic coupling is very strong.

Interpretation of the differences

Although the numerical results are comparable to the measurements, some differences are observed between model responses. In the vicinity of the rock wall, the hydration occurs immediately after the emplacement of bentonite in the form of advective flow governed by Darcy's law. The incoming water increases in saturation and the bentonite swells (consequently porosity increases), and the relative permeability and intrinsic permeability increase correspondingly. As shown in Fig. 5-2, the relationship adopted by EPFL features a higher increase in the permeability upon wetting than that adopted by CIMNE and Clay Tech. The comparison between the permeability model and experimental data shows that the EPFL model features the upper bound whereas the other two model responses are situated in the lower bound of the experimental data. This corresponds also to the observation of relative humidity prediction in comparison to the measurements, where the EPFL model slightly overestimates the relative humidity whereas the CIMNE predicts slightly lower values than the measurements. This also explains the significant difference in Section H, where an increase in water flow occurs after Heater #1 is switched off. With a higher permeability, the water flows faster, increasing the availability of liquid water to be evaporated.

In relation to the 1-D model of Clay Tech, the model responses show a good agreement with 2-D predictions in the vicinity of the host rock. This could suggest that, in the radial direction, thermal-hydraulic processes are indeed one dimensional in the hot section. The hydration process is independent of the host rock, as long as it is considered to be in a saturated state and has sufficiently high permeability. In addition, the processes are controlled dominantly by the hydraulic properties of the bentonite. Nevertheless, the difference between the 1-D and 2-D models becomes more important closer to the heater. This difference potentially relates to the different treatment of the bentonite's mechanical response to heating in the two models, which eventually affects the variation in permeability and accordingly the flow behaviour.
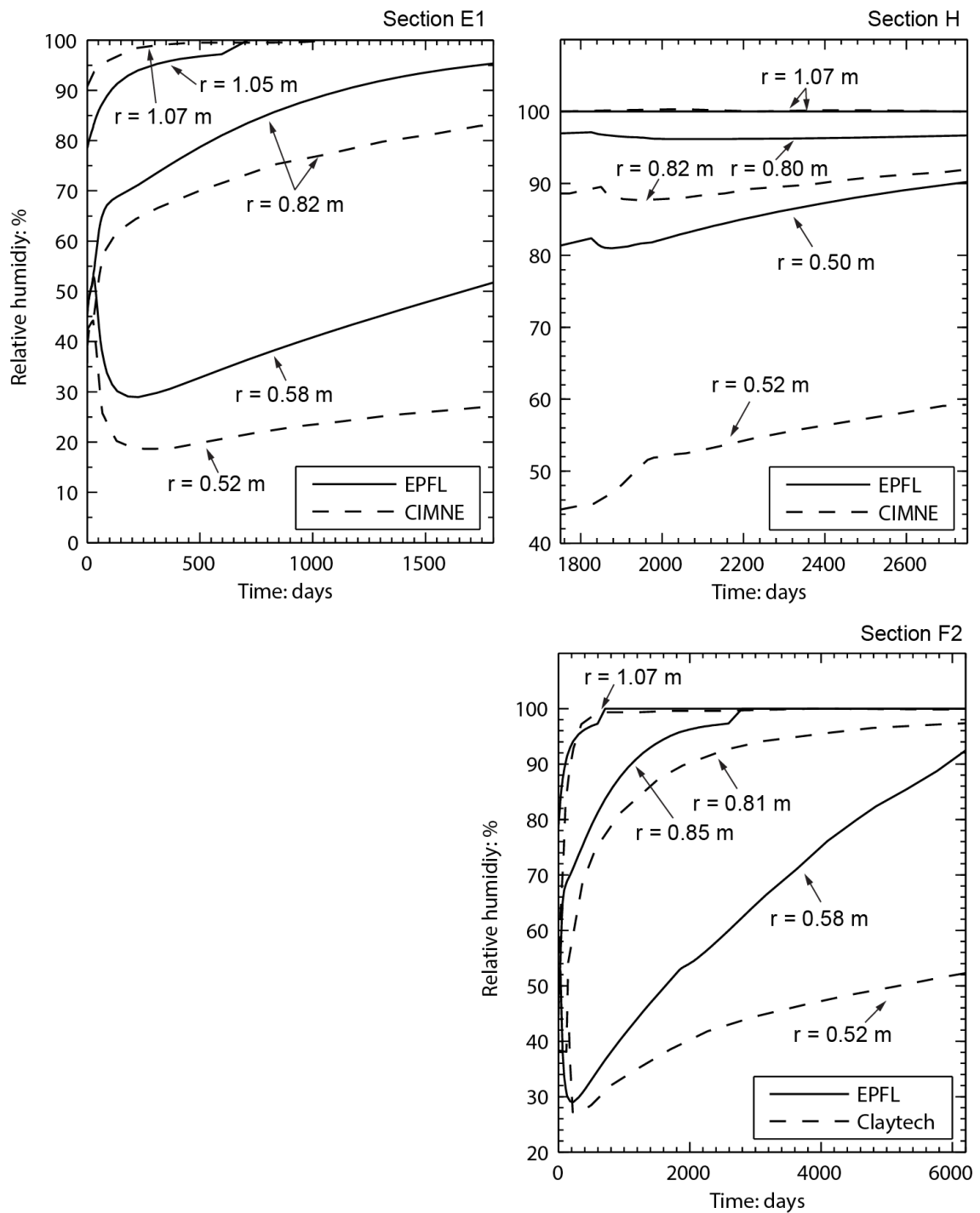
Fig. 5-4:   Simulated evolution of relative humidity on the sections E1, H and F2 in the
             bentonite buffer by Clay Tech, CIMNE and EPFL.

5.4.3 Thermo-hydro-mechanical evolution of the buffer system

Results in terms of dry density, water content and stress

The prediction of dry density and water content strongly depends on the constitutive mechanical law adopted in the study, which is the most essential coupling mechanism in THM modelling studies. The dry density is directly calculated from porosity variations while both porosity and saturation contribute to the calculation of water content. As can be noticed in Fig. 5-5, the predicted dry density distributions after dismantling show significant differences. At the Section G, the EPFL model predicts an even distribution of dry density along Section G whereas CIMNE predicts a lower dry density in the vicinity of the host rock and closed to the heater. Because of the presence of the liner, a higher dry density at the location of the liner is predicted. As the water content is linked to dry density, the model responses of water content and dry density are similar but in an inverse way. The predicted water content by CIMNE is higher in the vicinity of the host rock and is lower near the liner location.

Section F2 provides a better representation of the THM responses of the three models. Between CIMNE and Clay Tech, an agreement in general trend can be established. Differences can be observed closer to the heater: a higher value of dry density is predicted by Clay Tech. The EPFL model provides nearly evenly distributed values along the section except near the heater where it predicts higher density and lower water content. The predicted variations are, however, much smaller than those from CIMNE and Clay Tech in terms of density and water content. Fig. 5-6 illustrates the simulated normal stress on the host rock wall by CIMNE and Clay Tech. Because the bentonite is constrained between the stiff heater and host rock, the bentonite starts to build up the swelling pressure in response to the hydration. The swelling pressure reaches values of several MPa as observed in the measurements as well as in the simulation. The values predicted by CIMNE are lower than those from Clay Tech. As can be evaluated from Tab. 3-5, EPFL predicted the swelling pressure of 1.53 MPa by the end of the saturation process. The elastic bulk modulus decreases upon wetting in the adopted model by ACMEG while it increases upon wetting for BBM in constant volume conditions. As a consequence, the swelling pressure is lower in the prediction with ACMEG compared to that with BBM and its derivatives.

Interpretation of the differences

The comparison between CIMNE and Clay Tech reveals, that the results are similar since the constitutive models adopted by the two teams are based on the BBM constitutive model. The one adopted by CIMNE is extended to take into account the thermal expansion of the bentonite whereas Clay Tech uses an isothermal version. This can be noted by the fact that the predicted dry density and water content in Section F2 only differ in the vicinity of the heater due to heating whereas the predictions are nearly equivalent in the vicinity of the host rock. Given the high increase in temperature near the heater, the thermal effects on the mechanical responses are quite important. The heating induced expansion leads to a lower dry density in the case of CIMNE which is not seen in Clay Tech's model. As for the stress development, the general trends are predicted in a different manner. The CIMNE model predicts that the stress increases upon hydration rapidly in the initial stage. As hydration continues, the hydraulic gradient decreases, and the stress development upon hydration tends to stabilize. On the other hand, Clay Tech predicts a monotonic increase of stress development. Plasticity is occurring upon hydration. This may be explained by the fact that the lateral displacement is completely constrained (which is also supported by the fact that the dry density in the inner part was the same as for the blocks at installation), whereas the swelling pressures in the lateral directions are higher, leading to a higher shear stress state. In addition, the model adopted by Clay Tech is

calibrated to the MX80 bentonite which is however similar to that of FEBEX bentonite below $1'600$ kg/m^3 in dry density.

In comparison, the prediction by EPFL shows a homogenized dry density after the dismantling which is nevertheless nearly equal to the initial value along both sections G and F2. The reason stated by the authors is that since the irreversible hydro-mechanical mechanism is not activated, the modelled process remains elastic. After the saturation of the bentonite, the initial density is recovered. From the perspective of CIMNE, the dry density distribution after the dismantling nearly doesn't change with respect to the distribution in the very early stages of the experiment. The reason stated by CIMNE is that the material becomes stiffer and more difficult to deform since its elastic bulk modulus increases with the increase of swelling pressure. Two different model responses are the direct consequence of the chosen constitutive formulations for the bentonite.
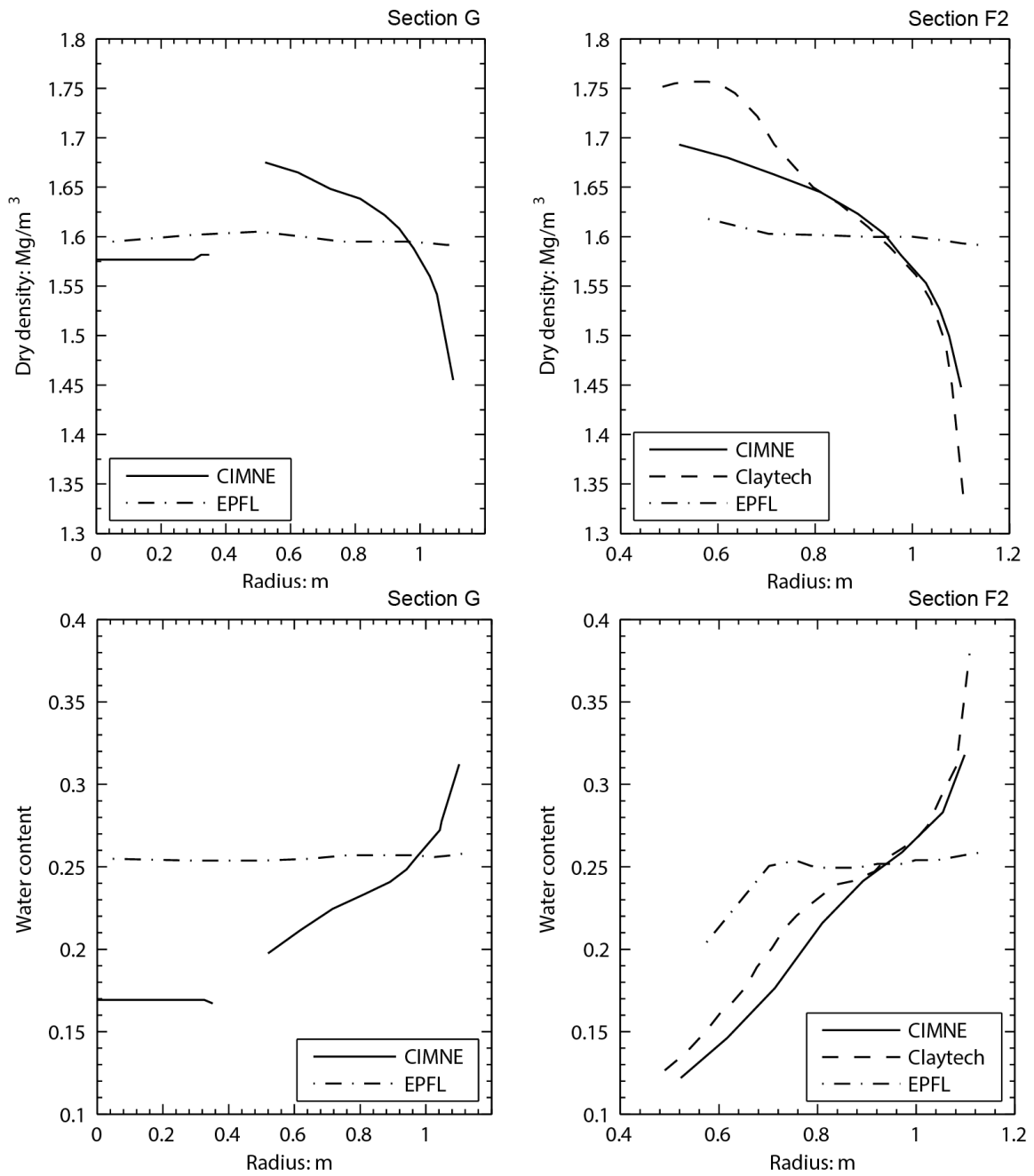
Fig. 5-5:   Water content and dry density calculated from the simulated results at the sections
              G and F2 by Clay Tech, CIMNE and EPFL.
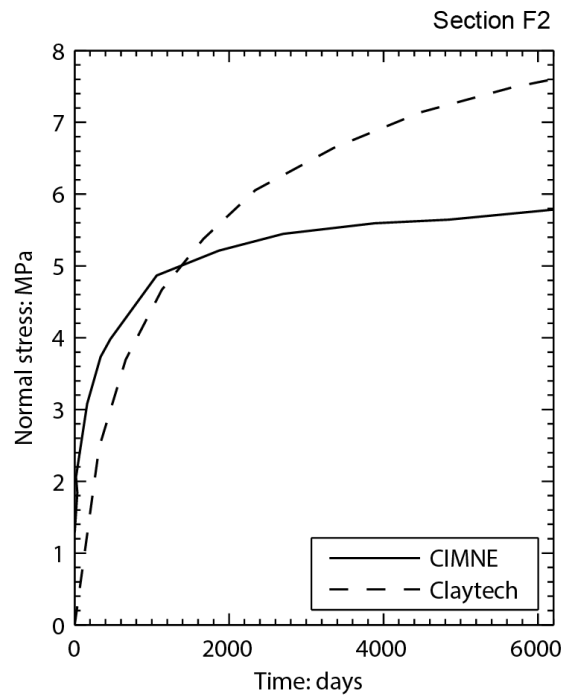
Section F2

Fig. 5-6:   Simulated normal total stress on the wall of the host rock at the Section F2 by Clay Tech and CIMNE.

5.5   Comparison of accomplishments

5.5.1   Main processes

The conclusions on the main processes are consistent amongst the three teams. The main drivers that affect the bentonite region are the heat flux from heaters and the capillary hydration from the surrounding host rock. In the vicinity of the heater, the bentonite buffer is subjected to a strong temperature increase. Heat conduction is considered as the key process for thermal transfer, as found by the three teams. The good agreement between the simulation on the temperature evolution and the measurements confirms this conclusion. The dominant property is the thermal conductivity of the bentonite and the host rock. With the increase of temperature, a thermal gradient develops in the region between the heater wall and the surrounding host rock.

With the thermal loading from the heaters and the pore water inflow from the host rock, the bentonite undergoes a more complex THM coupled process. The increase of temperature leads to the generation of vapour, and the vapour flows outwards from the heater wall by diffusion condensing in the cooler region. This leads to an increase of water content in that region. This process increases the saturation rate of the middle part. The water permeability and the thermal conductivity change with the variation of porosity and water saturation, which consequently modifies the thermal transfer and the water flow in this region. In response to the TH loading, the temperature increase induces both the expansion (thermal expansion) and the compression (drying shrinkage) of the bentonite buffer close to the heater. As a consequence, the void ratio of the bentonite buffer changes.

In the vicinity of the host rock, the bentonite with an initial high suction takes water from the saturated rock, i.e., hydration. Three models conclude the same observation that the bentonite controls the water inflow processes. During the hydration, the mechanical behaviour is affected due to the high swelling capacity of bentonite. No thermal plasticity and hydraulic swelling plasticity are foreseen by the two teams of EPFL and CIMNE. Due to the presence of stiff surrounding rock and heaters, the bentonite buffer is under a nearly constant volume condition. The main mechanical response is the build-up of the swelling pressures, reaching values of several MPa, as observed in the FEBEX in-situ test and simulated by CIMNE and Clay Tech.

5.5.2   Progress made in this exercise, remaining uncertainties

The numerical models presented in this study include essential physical mechanisms, and demonstrate the ability to properly capture most of the observed phenomena and features during the experiment. It can be concluded that both the thermal response and hydraulic response are well captured by the current models because of a good understanding of the governing physical processes. Progress has been made on capturing the swelling behaviour of the bentonite, providing a better understanding of the interaction between the bentonite and the other components of the repository near-field. The swelling stress prediction is in qualitative agreement with the measurements.

CIMNE points out that it is likely that different constitutive laws and parameter settings may provide consistent responses with the available experimental observations. This is also observed when comparing the CIMNE and Clay Tech results, models with two different versions of the BBM model and two different parameter settings, feature similar trends, and even display the same results at certain locations (Fig. 5-5). In this regard, the three teams all agree on the point that research efforts are still required to improve the predictive capability of the constitutive models (not only in terms of mechanical behaviour but also in flow properties) of the swelling bentonite, especially when it is of high swelling potential.

EPFL also points out another uncertainty of the FEBEX dismantling simulation that is related to the effects of the gaps on the THM coupling processes. The effect of gaps between the bentonite blocks is simplified by three teams while it may play an important role in saturation, stress development, and heat and flow transfer (Cerfontaine et al., 2015). However, it is known that the consideration of such gap effects would require much more computational effort and more complex contact elements to be included in the models. In addition, more fundamental research needs to be carried out to investigate the importance (or not) of these gaps.

5.5.3   Consequences for the early repository evolution

The three teams conclude that, in terms of the hydraulic evolution, the bentonite buffer will reach a fully saturated state in the long term. After the heater switch-off, the decrease of the temperature leads to vapour condensation, causing a local increase in water saturation in the immediate vicinity of the heater. A hydraulic gradient is developed fast between the inner part and the middle part, eventually accelerating the hydration progress by the advective flow mechanism. In response, the saturation rate increases.

Both CIMNE and Clay Tech expect a higher density of the bentonite near the canister, with a lower density in the vicinity of the host rock. On the other hand, EPFL suggests that the dry density gradient disappears after the complete saturation of the bentonite buffer. As explained above, this difference comes from the choice of constitutive model that requires further investigation.

5.6   Conclusions and lessons learned

The physical THM processes considered by the three models are non-linear and highly coupled. The fluid and mechanical properties are non-linear functions of temperature, pressure, and deformation, adding complexity to the system. The results of the FEBEX-DP modelling benchmark study as presented and discussed above show that a good qualitative agreement of model predictions can be achieved in the overall THM behaviour of the bentonite, whereas a quantitative agreement can be achieved in terms of temperature and relative humidity. This demonstrates that current models are capable of accounting for the relevant material properties and processes reasonably well in order to predict the fate of the buffer that is subjected to complex environmental loadings.

Although there are differences in the numerical implementations of the simulation codes, the fundamental formulations that describe the THM processes can be considered equivalent. For a given well-defined problem, the differences of model responses are thus only due to the choice of constitutive models and parameter settings. Within this comparison task, two teams (CIMNE and EPFL) adopted a very similar conceptual 2-D model with the consideration of engineering operations involved in the FEBEX experiment. Clay Tech identified a simplified 1-D configuration to focus on the heating induced physical variations. Therefore, deviations between results from CIMNE and EPFL arise from the different constitutive laws and parameters; deviations between Clay Tech and the other two teams also relate to different interpretations of the problem description.

It is worth noting that the three teams adopt different parameters for the same problem, based on the same experimental data shown in Fig. 5-1, as well as different effective properties for the host rock (cf. Tab. 5-1). Such different interpretations can also be the source of deviations in the results. This highlights the importance of choosing input parameters across large datasets. The consistency of input parameters with laboratory evidence and their relevance to the investigated problem could be used to assess that uncertainty. Besides, the difference in the two mechanical constitutive models used in this study also arises from the concept of effective stress. The use of stress pair (net stress and suction, i.e., Eq. A11) in BBM is an efficient approach to formulate the constitutive model, but fails in the transition from unsaturated state to saturated one. The generalized effective stress in ACMEG (Eq. 3-23) offers advantages in model capacities, allowing a natural transition from unsaturated to saturated state, taking the increase in material strength with increase in effective stress directly into account, as well as using a unique critical state line independent from the degree of saturation. Nevertheless, this topic is still debated in modern unsaturated soil mechanics.

The comparison of the detailed implementation between the three models cannot be carried out on a one-to-one basis. The three models apply a series of different assumptions and simplifications, and to some extent also different geometries. Different model parameters and properties add another source of uncertainty in the results. The comparative analysis presented here does not provide a detailed investigation of all sources of deviations in the results, but sets the base for future work on well-designed benchmark problems increasing the confidence in the predictive ability of THM models.

6   Post modelling comparison to the observations

Following the completion of the modelling activities by the three teams (CIMNE, EPFL, Clay Tech; Chapters 2, 3, and 4, respectively) and the comparison between the models (Chapter 5), model results are compared to post-mortem measurements following the dismantling of Heater #2. The comparison is performed for Sections F2 and G corresponding to the middle of Heater #2 and the edge of the dummy, respectively (Fig. 1-2). The corresponding post-mortem measurements are from sections S49 and S39, respectively. The comparison is performed for water content and dry density.

6.1   Comparison at Section F2 (S49)

Fig. 6-1 shows the comparison between model predictions and measurements at Section F2, respectively section S49 of the measurements. The model results are illustrated separately for each modelling team. The measurements are illustrated for the different radii used to evaluate water content and dry density with increasing distance from the central axis. Moreover, the mean value and range of measured values is indicated at different increments of distance from the central axis (red lines, i.e. for distance 0.5 – 0.6 m, for distance 0.6 – 0.7 m, etc.).

It is indicated that the three models predict higher water contents with increasing distance from the central axis (see also Chapter 5). As discussed in Chapter 5, water contents are higher away from the central axis due to the water evaporation near the heater and the associated condensation of water and re-saturation closer to the tunnel wall. Closer to the central axis, the water content predicted by EPFL (values between 0.2 and 0.25) is higher than the water content from Clay Tech and CIMNE (values between 0.12 and 0.22). With increasing distance from the central axis (i.e., distances above 0.8 m), the water content gradient is higher in the predictions by Clay Tech and CIMNE. Accordingly, water contents from Clay Tech and CIMNE are higher compared to EPFL at distance larger than 1.0 m. The comparison to the measurements indicates a reasonable agreement between the models and the experiment, with the measured values lying within the range of predictions provided by the three teams. Measured water contents range between 0.17 and 0.25 for distances below 0.8 m, and between 0.25 and 0.31 for distances above 0.8 m, respectively. The measured values vary across the different radii, whereas the 1-D and 2-D models provide axial-symmetric representations.

The dry densities predicted by the three modelling teams (Fig. 6-1) show an overall decrease with increasing distance from the central axis. In general, this behaviour is due to the compaction of the bentonite near the heater and the expansion of bentonite closer to the tunnel walls (see also Chapter 5). Closer to the central axis (i.e., distances below 0.8 m), the dry densities predicted by EPFL are the lowest among the three models (approximately 1.60 kg/m^3), whereas dry densities from Clay Tech are the highest (up to 1.75 kg/m^3), and those from CIMNE lie in between. As discussed in Chapter 5, the model from Clay Tech does not include thermal expansion in the bentonite which can affect the dry density change due to thermal expansion compared to the other two models. With increasing distance from the central axis (i.e., distances above 0.8 m), dry densities decrease significantly in the Clay Tech and CIMNE predictions (down to approximately 1.35 to 1.45 kg/m^3) whereas EPFL predicts a milder decline (dry densities slightly below 1.60 kg/m^3).

The comparison to the measurements indicates reasonable agreement, with measured values mostly within the range of predictions provided by the three teams. Measured dry densities range between approximately 1.60 and 1.75 kg/m^3 for distances below 0.8 m from the central axis, and between approximately 1.48 and 1.65 kg/m^3 for distances above 0.8 m from the central axis, respectively. As observed for water content, dry density measurements correspond to different radii and therefore depict a higher variability compared to the model representation.

6.2   Comparison at Section G (S39)

Fig. 6-2 shows the comparison between model predictions and measurements at Section G, respectively S39. Only model results from EPFL and CIMNE are presented, as the 1-D model from Clay Tech corresponds to a section at the middle of the heater. Similar to the previous post-mortem, measurements are illustrated for different radii together with the mean and the minimum/maximum range.

The water content predicted by EPFL is almost constant across the tunnel, with a minor increase indicated at distances from the central axis larger than 0.6 m (water content values from 0.255 near the centre to 0.27 near the wall). The water content predicted by CIMNE is significantly lower below the dummy (values of approximately 0.17 at distances below 0.5 m), and then increases towards the tunnel wall (values from 0.2 to 0.33). Overall, the CIMNE prediction shows a higher water content gradient between the dummy and the tunnel wall, compared to EPFL. As discussed in Chapter 5, this relates to the different response in permeability to hydration adopted in the two models. The post-mortem measurements indicate a behaviour between the two model predictions. Water contents measured at distances below 0.8 m from the central axis are relatively uniform and similar to the EPFL prediction, albeit somewhat higher (values between 0.26 and 0.27). At distances larger than 0.8 m from the central axis, measured water content increases gradually to approximately values between 0.26 and 0.29, in a similar fashion to the CIMNE prediction. This effect presumably also relates to the transport of water through the dummy. In the experiment, the dummy is perforated, allowing some transport of water across it as the buffer hydrates with water from the surrounding host rock. On the other hand, the dummy in the CIMNE simulation limits the transport of water towards the inner part, resulting in lower water contents below the dummy.

A similar effect is observed in the dry densities. Both models predict similar and relatively constant dry densities below the dummy (approximately 1.57 to 1.60 kg/m^3). Between the dummy and the tunnel wall, EPFL predicts a mild decrease of dry density (from 1.60 to 1.58 kg/m^3) whereas CIMNE predicts a significant increase of dry density directly outside the dummy (up to 1.67 kg/m^3), followed by a steep decrease towards the tunnel wall (down to 1.45 kg/m^3). The post-mortem measurements show once more a behaviour that lies between the two model results. Measured dry density is somewhat lower inside the dummy (values between 1.50 and 1.56 kg/m^3), then increases directly outside the dummy (up to approximately 1.60 kg/m^3), and consequently decreases towards the tunnel wall (values between 1.50 and 1.57 kg/m^3). These differences between measurements and the predictions are also associated with the different constitutive models used by EPFL and CIMNE (see Chapter 5), as well as the perforated dummy and its representation in the 2-D models.

6.3   Closing remarks

It is shown that the differences between the models and the post-mortem measurements after the dismantling of Heater #2 are traced back to the conceptualizations adopted in the models through the model geometries and the constitutive relationships used for the THM coupling described in Chapter 5. The constitutive models used by EPFL and CIMNE lead to a different hydration process, providing an envelope of water content predictions that encompass the measurements. Moreover, the thermo-mechanical coupling will mostly affect the dry density prediction near the heater, as shown by comparing the post-mortem measurements to the Clay Tech prediction (see also Chapter 5). At the "cold" Section G, the impact of the perforated dummy on water content and dry densities is clearly seen when compared to the models, and depends on the model approach adopted for the dummy.

Despite these differences, the comparison of water content and dry densities predicted by the modelling teams and measured in the post-mortem analyses draws a consistent picture of the THM evolution associated with the hydration and drying of the bentonite in the FEBEX in-situ experiment. It can be stated that, given the model approximations made by the three teams in this study, the predictions capture the evolution in the selected "hot" (Section F2) and "cold" (Section G) sections reasonably well. The range of values obtained through measurement at different radii in the bentonite is within the observed range of model predictions considering the conceptual uncertainties related to the model approach.

Fig. 6-1:   Comparison between water content (top) and dry density (bottom) simulated by CIMNE, EPFL, and Clay Tech at Section F2 and post-dismantling measurements at Section 49.
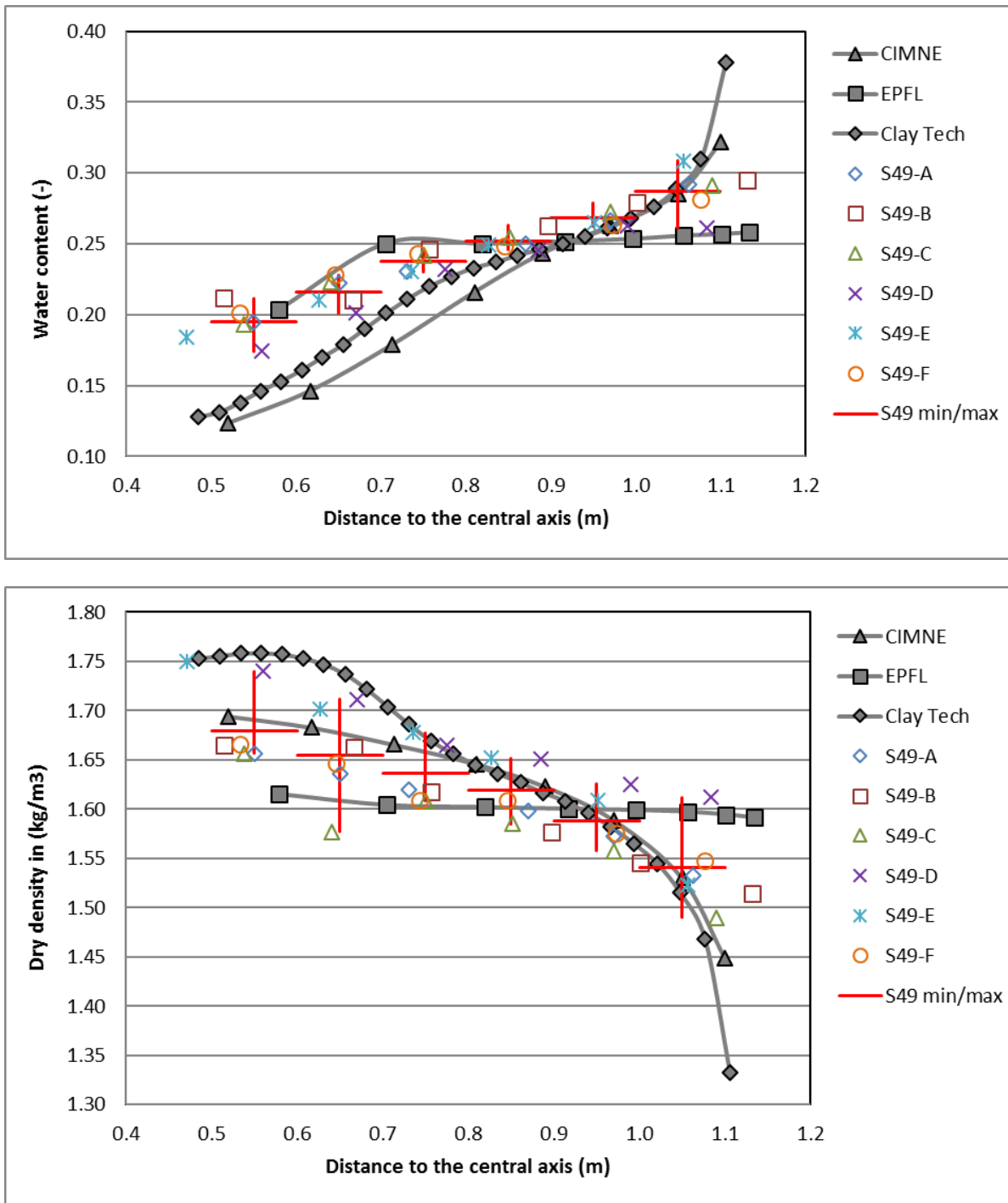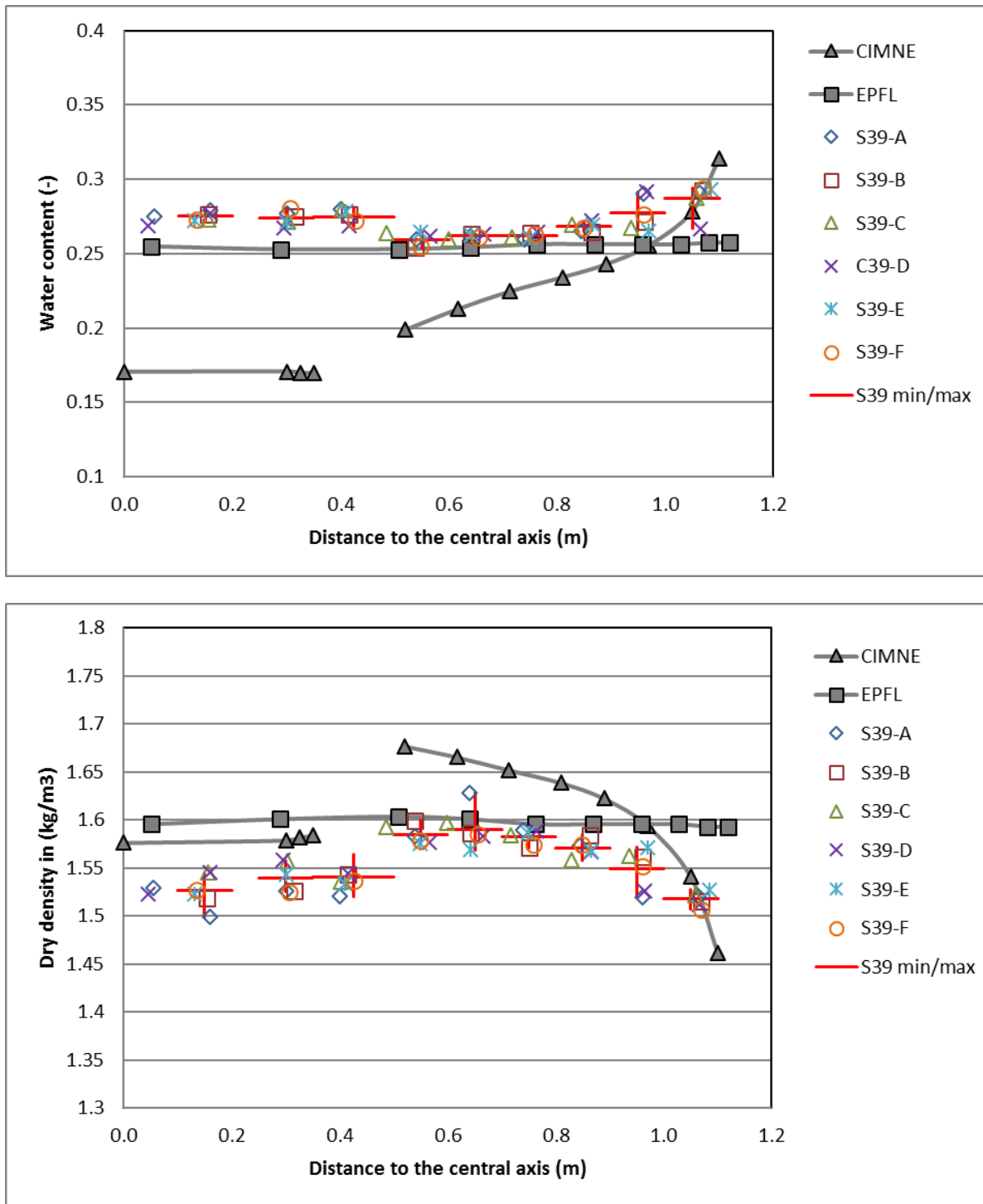
Fig. 6-2:   Comparison between water content (top) and dry density (bottom) simulated by CIMNE, EPFL, and Clay Tech at Section G and post-dismantling measurements at Section 39.

7   Conclusions

The FEBEX "in-situ" experiment was a full-scale test performed under natural inflow conditions at the Grimsel Test Site (GTS) in Switzerland. Objectives of the experiment were to demonstrate the practicality of implementing a horizontal disposal concept for high-level waste (HLW) in crystalline host rock, validate the performance of the engineered barrier system (EBS), and improve the understanding of coupled thermo-hydro-mechanical (THM) and geochemical (THMC) processes. The experiment was performed in a horizontal drift excavated in the Grimsel granodiorite. Two electrical heaters were placed in the axis of a drift within a buffer of pre-compacted FEBEX bentonite blocks. The backfilled area was sealed with a plain concrete plug placed into a recess excavated in the rock. The heating of the in-situ test began in 1997 maintaining a temperature of 100 °C at the heater surface while the bentonite slowly hydrated with water from the granite host rock. The evolution of temperature, water saturation, relative humidity, total pressure, pore pressure, and displacement was monitored by sensors placed in the buffer and the geosphere. In 2002, Heater #1 was dismantled (after 5 years of heating) while Heater #2 remained in operation. A shotcrete plug was placed and a perforated dummy was used to replace Heater #1. In 2015 Heater #2 was switched off and the second (and final) dismantling of the in-situ experiment took place. After each dismantling operation (2002 and 2015), samples were collected and tested to obtain additional post-mortem measurements.

Numerical models are essential tools to assess the performance of the EBS in deep geological repositories. Comparison of modelling analyses to the observations in the in-situ experiment aims to improve the understanding of the THM processes taking place in the near-field, build confidence through model validation, and provide evidence to complement and extend the existing modelling capabilities. Three teams were tasked with the pre-dismantling modelling of the THM evolution in the FEBEX in-situ experiment: CIMNE (International Center for Numerical Methods in Engineering, Spain), EPFL (Laboratory for Soil Mechanics at the Swiss Federal Institute of Technology in Lausanne, Switzerland), and Clay Technology AB (Sweden). The teams were free to choose the modelling approach and tools used for their analyses. CIMNE and EPFL were involved in FEBEX modelling activities including material parameter calibration and preliminary evaluations. Modelling by CIMNE and EPFL was performed using 2-D axisymmetric longitudinal representations of the drift with the heaters, bentonite buffer, concrete plug, and surrounding rock in Code_Bright and Lagamine, respectively. Both models assumed an effective dry density of 1.60 kg/m^3 (i.e., including the construction gaps between the blocks) rather than the compacted block density of 1.70 kg/m^3. On the other hand, Clay Technology AB (Clay Tech) was engaged at a later stage to develop a 1-D axisymmetric model in Code_Bright focusing on the mid-section of Heater #2. In this case, an initial dry density of 1.70 kg/m^3 was used for the blocks whereas a dry density of 1.60 kg/m^3 was used for a separate material representing the gaps and intersections. Temperature distribution in the Clay Tech model was calculated with a 2-D analytical solution that was used to infer the thermal boundary conditions for the 1-D simulations. The mechanical constitutive model used by CIMNE was the Barcelona Basic Model (BBM) after Alonso et al. (1990), calibrated to the non-isothermal behaviour of FEBEX bentonite. The initial operation of the experiment and the CIMNE model configuration overlapped for a few months at the start of the test. However, the model was established prior to the heating phase to incorporate all information from laboratory tests and no adjustments were made during the heating phase. Given the length of the experiment, the predictions can be classified as blind predictions. The EPFL model was developed with the ACMEG elasto-thermoplastic constitutive model (François and Laloui, 2008). The model by Clay Tech was built with the BBM model calibrated to MX80 bentonite without thermal expansion of the bentonite mineral. All three teams were asked to describe in detail their modelling approach, present and interpret their predictions through direct comparison to sensor

data as well as post-mortem measurements from the first dismantling, evaluate the driving processes in the in-situ test, and assess the progress made and the associated uncertainties. Moreover, each team provided "blind" predictions of dry density and relative humidity for subsequent comparison to measurements from the second dismantling.

Synthesis

All three modelling teams conclude that the THM evolution in the FEBEX in-situ experiment is controlled by the high affinity of bentonite for water and the water supply from the rock, combined with the non-isothermal effects introduced by the heating. The main driving processes identified in the THM modelling are summarized as follows.

After the emplacement of the bentonite buffer and prior to heater switch-on, hydration of the buffer begins with water flow induced by the hydraulic gradient established between the bentonite and the surrounding host rock. During this phase, the mechanical behaviour is not affected by the negligible temperature variations and no thermally induced stresses or deformations take place. However, the high swelling capacity of the bentonite results in expansion of the bentonite matrix into the gaps between the blocks as well as into the available volumes at the bentonite-granite interface. This increases the matrix porosity and the intrinsic hydraulic conductivity. As the degree of saturation increases in the bentonite, the water flow through the partially saturated buffer also increases. With the increasing saturation of the buffer the hydraulic gradient eventually decreases so that water flow at later times will decrease. However, the drift will constrain the swelling deformation and swelling pressure will be generated.

With the onset of the heating phase, the thermal gradient becomes an additional driving process. At the inner part of the buffer, high heat fluxes occur from the heaters to the bentonite. The primary heat transfer mechanism is conduction through the partially saturated bentonite, which is controlled mainly by the (saturation-dependent) thermal conductivity of the barrier and the surrounding host rock. The high temperatures developing near the heater result in high water evaporation which leads to drying of the bentonite. Thus, the degree of saturation will decrease and suction will increase again in the inner part of the buffer. Vapour arising from the evaporation flows outwards until it reaches the cooler outer part of the buffer, where it condensates, causing a local increase in saturation. Vapour diffusion also contributes, albeit to a much lesser extent, to heat transport. The thermal loading at the inner part causes shrinking of the bentonite with the associated decrease in dry density.

The reversed process takes place during the cooling phase with the gradual increase of saturation in the inner part of the buffer due to suction. Hydration of the bentonite will eventually lead to full saturation, but the time required for full saturation can be very long depending on the hydraulic properties of the buffer and the host rock.

The three teams report the following observations made with the adopted modelling approaches:

CIMNE

For the first phase of the experiment prior to switch-off and excavation of Heater #1, the THM simulation results in overall reasonable agreement with the sensor measurements in terms of temperature and relative humidity. Stress predictions pose, however, a challenge due to uncertainty related to the early-phase contacts and gaps between bentonite blocks. For the cooling of Heater #1 the simulation provides a quantitative prediction of temperatures,

especially close to the heater, and a qualitative prediction of relative humidity for as long as the sensors were operative. The prediction deviates from the sensor data somewhat more in the cool section between the heaters. The prediction of temperatures in the rock during cooling shows good agreement to the measured values. On the other hand, a relatively poor agreement is reached in terms of liquid pressures and stresses in the rock. The mechanical effects affecting the stress prediction in the near-field are the cooling (more influential) and the removal of the clay barrier (less influential). The simulation of the different stages of the first dismantling (i.e., plug demolition, bentonite excavation, etc) show the effect on longitudinal displacement and axial stress. The comparison of predicted water contents and dry densities to the post-mortem tests from the first dismantling shows overall a reasonable agreement. In the hot section, the model reproduces the pattern of water contents and dry densities showing the drying of the inner part of the bentonite and associated shrinking and expansion of the bentonite close to the heater and the tunnel wall, respectively. In the cold section the model reproduces the hydration reasonably well, which is, nevertheless, slower than in the experiment, and the dry density changes measured post-mortem. After the first dismantling and during switch-off and excavation of Heater #2, the model once more provides a reasonable agreement to sensor data in terms of temperature and relative humidity albeit with increased uncertainty associated with failing sensors at this later stage of the experiment. The uncertainty in stress predictions associated with the gaps propagates to this later stage as well, compromising the comparison between model and experiment. In the host rock, the model provides a reasonably good prediction of temperatures and a more qualitative prediction of liquid pressures. Predictions of water content and dry density in the hot section after the second dismantling show overall similar patterns to the predictions after the first dismantling (i.e., slow hydration, similar dry densities). It is, however, indicated that this behaviour depends on the constitutive laws used. In the cool section, the water content and dry density prediction is strongly affected by the representation of the liner that replaced Heater #1. In both sections, estimates of dry density changes due to the unloading process indicate a relatively moderate effect.

Despite some differences, the model performance is globally satisfactory. The behaviour related to relevant THM variables is captured reasonably well by the model both in terms of time evolution (i.e., comparison to sensors) as well as in terms of post-mortem results. However, the model tends to under-predict water saturation measured post-mortem in the buffer due to slower hydration of the bentonite from the surrounding host rock. On the other hand, the model over-predicts water saturation in several sections of the buffer when compared to sensor data. Moreover, the prediction of stresses and liquid pressures in the near-field are challenged by the lack of a quantitative characterization and description of the contacts and gaps between the bentonite blocks and between the bentonite and the granite.

EPFL

The modelling initiates with the simulation of the tunnel excavation followed by the emplacement of the buffer and the ongoing hydration with porewater from the surrounding rock before the onset of the heating phase. The simulated time-histories of temperature and relative humidity for the entire heating phase (5 years of heating of heaters #1 and #2, then 13 years of heating only of Heater #2) show overall a good agreement with the sensor data at different sections around the heaters. Some deviations are observed in relative humidity that can potentially be attributed to the construction gaps affecting the adsorption of porewater in different parts of the buffer. Overall, the hydration and swelling of the bentonite is expected to lead to homogenization of the buffer over time. For the cooling of Heater #1 the simulation provides a quantitative prediction of the temperature decline. The comparison of simulated water contents and dry densities to the post-mortem tests from the first dismantling shows overall a good agreement. Water contents and dry densities were simulated before and after

dismantling. In the hot section, the model provides a reasonably good prediction of water content values and dry densities mainly in the inner section close to the heater. Some deviation is observed in the outer part near the tunnel wall possibly due to construction gaps that are not taken into account in the model, resulting in an overestimation in the model. In the cold section, the model reproduces the dry density and water content with some deviations near the tunnel wall. This is attributed to the mechanical law that has a limitation for the high swelling potential of the bentonite close to full saturation. An additional source of deviation is the presence of the construction gaps, as indicated for the hot section. The prediction of water content and dry density in the hot section after the second dismantling shows more uniform distributions compared to the first dismantling. A low gradient in dry density and water content is observed in the radial direction with lower water content near the heater, indicating that the inner part is still not fully saturated and has significant suction. Dry density is partly even below the initial value and thus may be underestimated because irrevocable swelling deformations are not foreseen by the mechanical law used in the analysis. Dry densities before and after dismantling show a relatively moderate change. In the cool section, water content and dry density are approximately constant along the radial direction. This indicates full saturation of the bentonite and homogeneous dry density that is equal to the initial value as no irrevocable swelling deformation is taken into account. It is, however, indicated that the hydration process and associated mechanical response depend on the constitutive laws used in the model.

The prediction of the TH evolution in terms of temperature and relative humidity over 18 years of heating is in good agreement with the sensor data overall. Some deviations occur in relative humidity, potentially due to the construction gaps that affect the hydration. Moreover, the predicted dry density and water content show good agreement with the post-mortem measurements from the first dismantling at the cool and hot sections. Some deviation in the dry density is attributed to the construction gaps as well as the mechanical law used in the model that may underestimate the swelling deformation of the FEBEX bentonite. After the second dismantling, the model predicts a relatively uniform water content and dry density along the radial direction.

Clay Tech

The temperatures calculated with the 2-D analytical thermal model at different sections are, overall, in good agreement with the sensor data during the entire heating phase (5 years of heating in heaters #1 and #2, followed by 13 years of heating only in Heater #2). The evolution of relative humidity predicted with the 1-D simulation shows, overall, a good agreement with the sensor data from the hot section. The simulated stresses also show a good agreement with sensor data in the lower part of the hot section. Nevertheless, increasing deviations from other sensor data, that display overall lower stress levels, are observed. The comparison of the simulation to the post-mortem tests from the first dismantling shows reasonable agreement. Some deviation is observed in the water content distribution, indicating that the predicted dehydration in the inner part is too extensive in the model. This can be attributed to transport coefficients (i.e., dependence of intrinsic permeability on porosity, vapour diffusion tortuosity), as well as the hydraulic and thermal boundary conditions used in the model. Moreover, the modelled dry density indicates somewhat more extensive shrinkage in the inner part and swelling in the outer part, respectively. The low dry density simulated in the outer part can be due to the plastic parameters used as well as the conceptualization of the construction gaps as a single major gap at the rock wall.

Summary of modelling performance

The three models incorporate similar processes with partly different constitutive models, and to some extent different input parameters and geometry approximations. Overall, all modelling teams can claim qualitative agreement to the observed evolution of the buffer. Temperature responses to heating as well as cooling are reproduced with a good match to the measured temperature time-histories. The predicted evolution of relative humidities captures the overall pattern observed in the sensors, although the comparison also indicates the difficulty to reproduce the hydration rates from the experiment. The comparison in terms of stresses and liquid pressures, when available, shows relatively poor agreement. The comparison of water content values and dry densities simulated in the hot and cold section to the post-mortem measurements from the first dismantling show overall good agreement. Some deviations between the models and the tests are due to conceptual representation of the modelled system (i.e., construction gaps), as well as the constitutive relationships used for the thermal, hydraulic, and mechanical behaviour of the bentonite.

Lessons learned

Following the initial configuration and calibration of parameters to data on bentonite behaviour, the models were not subjected to any re-calibration to data from the experiment throughout the heating and dismantling phases. In this sense, the predictions provided by the three teams for a period of 18 years, comprising the heating and dismantling phases, can be considered as blind predictions. The comparison between measurements and predictions achieved with the current modelling approaches show overall a good agreement, with some uncertainties that are discussed hereafter.

The thermal and hydraulic evolution is captured by the models fairly well, although the exact patterns (i.e., water content and dry densities after first and second dismantling) depend on the constitutive models used and the data-fit used for the model calibration. This constitutes a first source of uncertainty that relates to the different sets of parameters and constitutive laws that are likely to be applicable and at the same time consistent with available experimental observations. Moreover, uncertainty in the TH predictions is introduced by the conceptualizations used in the models. For example, the description of construction gaps (i.e. explicit gap material versus homogenized) between bentonite blocks and between the buffer and the rock can affect the water transfer and hydration process, whereas the representation of the perforated dummy in the model can impact predictions in the cool section. The mechanical behaviour of the bentonite is tied to some more challenging uncertainties. A first uncertainty relates to whether thermal plasticity exists for the FEBEX bentonite blocks. Another uncertainty lies in the mechanism of swelling for this material that has a very high swelling potential. An intrinsic question behind these uncertainties is how the fabric of bentonite is modified during the swelling process. This fabric modification happens on both macro- and micro level, as well as in the interaction between them. Another uncertainty relates to the effects of the construction gaps on the mechanical response. Owning to these gaps, the mechanical boundaries of the FEBEX blocks vary in time and space. As an example, the blocks can be assumed to initially swell under free swelling conditions due to the gaps between the buffer and the granite. While the gaps are filled by the swelling of blocks, the blocks swell under constant volume conditions and swelling pressure is generated. Moreover, the gaps in radial direction and those in the circular direction may develop and impact the THM evolution differently.

The modelling analyses presented in this report do not indicate any processes that hinder the extrapolation of the main tendencies over longer timescales, as long as the associated uncertainties are taken into account. In the long term, full saturation will be reached in the

buffer from water inflow from the surrounding rock. As indicated in the modelling results and post-mortem tests, the decrease of temperature after the thermal peak will lead to faster hydration and the time required to attain full saturation will decrease. This would also lead to less extensive heterogeneity in water content and dry density through the homogenization process. However, some heterogeneity might be expected due to the hysteretic behaviour of the retention properties and swelling pressure.

Missing bits

The analyses performed by the three modelling teams indicate that the construction gaps between the bentonite blocks and between the buffer and the rock can impact the hydration rate of the buffer and also affect the mechanical response of the bentonite as it swells into the gaps. Although some tests have already been done to investigate the effect of gaps on hydraulic conductivity, there is currently not enough evidence to develop a systematic conceptualization of their effect in the THM evolution of the buffer.

The long timescales involved in the FEBEX in-situ experiment pose a challenge for any model verification and further developments. The model results as well as post-mortem measurements indicate that full saturation has not been reached after 18 years of operation of the experiment. As such, the long-term state of water content and dry densities has not been reached to provide relevant evidence. The time that would be needed for full re-saturation could not be predicted with confidence due to the uncertainty related to the constitutive relationships assumed in the THM coupling.

The mechanical response under thermal loading of bentonite needs further investigation. A topic of interest is whether the thermally-induced shrinking of bentonite is recoverable or not. Laloui et al. (2009) point out that the thermal loading can cause some plastic deformation for the normally consolidated clays. In the presented modelling analyses, no thermal plasticity effects were considered. However, owing to the presence of montmorillonite, the fabric of bentonite can be modified with the absorption of water, which may change the bentonite state from over-consolidation to normal consolidation and lead to thermal irrecoverable deformation. Moreover, the coupling of thermal loading and hydraulic loading on mechanical response also needs further investigation. Additional laboratory tests could also be conducted to investigate the fabric modification and associated swelling mechanism on the macro- as well as on the micro-level. Finally, whereas some mechanical aspects have been captured, the prospect for simulating more complex processes (i.e. swelling/consolidation cycles with hysteretic effects) with the constitutive laws used in this study appears to be limited.

Closing remark

The three models described in this report employ different approaches and constitutive models for the prediction of the THM evolution in the FEBEX in-situ experiment and therefore result in partly different predictions. However, it is indicated that the deviations in their predictions are relatively moderate. All three models reproduce, at least qualitatively and in some cases also quantitatively, the TH evolution and to a certain degree also the mechanical response of the buffer. Following the conclusion of all modelling activities, an additional comparison was performed between water content and dry densities measured with post-mortem tests after the second dismantling and the blind predictions provided by the teams after 18 years comprising the different heating and dismantling phases. The comparison confirms that the predictions envelope the values measured at different radii in the cold and the hot sections. The model responses associated input parameters and conceptual assumptions are once more identified by

comparing to the data, in a similar fashion to the first dismantling. It is thus concluded that deviations between the simulations and the measurements are traceable over the entire 18 years to uncertainties that have been identified mainly in the constitutive models and conceptualizations used in the models. Despite these deviations, the quantitative comparison of processes predicted by the modelling teams and measured in the post-mortem analyses draws a consistent picture of the THM evolution associated with the hydration and drying of the bentonite in the FEBEX in-situ experiment. The synthesis identified the strong and weak points of the models, and improved the understanding of processes that need to be accounted for in order to improve predictions on the buffer evolution. The analysis also draws the picture of additional evidence that is required to enhance the current model capabilities for reliable predictions of the long-term evolution in a geological repository.

8   References

Abós, H. & Martínez, V. (2015): Sample Log Book 34 to 62 FEBEX-DP. AN 15-578, September 2015.

Åkesson, M. (2013): SSM question Issue 1.4 Bentonites other than MX-80. Clay Technology, SKBdoc 1415875, version 1.0, Svensk Kärnbränslehantering AB.

Åkesson, M., Börgesson, L. & Kristensson, O. (2010): SR-Site data report. THM modelling of buffer, backfill and other system components. SKB TR 10-44, Svensk Kärnbränslehantering AB.

Alonso, E., Alcoverro, J., Coste, F., Malinsky, L., Merriensoukatchoff, V., Kadiri, I., Nowak, T., Shao, H., Nguyen, T. & Selvadurai, A. (2005): The FEBEX Benchmark Test: Case Definition and Comparison of Modelling Approaches. International Journal of Rock Mechanics and Mining Sciences 42(5-6) (July), 611–638.

Alonso, E., Gens, A. & Josa, A. (1990): A constitutive model for partially saturated soils. Géotechnique, 40(3): 405-430.

Alonso, E.E. & Alcoverro, J. (2005): DECOVALEX III project: modelling of FEBEX in-situ test: task 1: Final Report SKI, Sweden, Statens Kärnkraftinspektion Editor.

Bárcena, I. & García-Siñeriz, J.L. (2015a). FEBEX-DP (GTS) Full Dismantling Test Plan. Nagra Arbeitsbericht NAB 15-15.

Bárcena, I. & García-Siñeriz, J.L. (2015b): FEBEX-DP (GTS) Full Dismantling Sampling Plan. Nagra Arbeitsbericht NAB 15-14.

Bárcena, I., Fuentes-Castillana, J. & Garcia-Siñeriz, J. (2003): Dismantling of heater No. 1 at the FEBEX in-situ test. Descriptions of operations, Report: 70-AIT-L-6-03.

Börgesson, L., Johannesson, L-E., Sanden, T. & Hernelind, J. (1995): Modelling of the physical behaviour of water saturated clay barriers. Laboratory tests, material models, and finite element application. SKB TR 95-20, Svensk Kärnbränslehantering AB.

Bowen, R.M. (1982): Compressible porous media models by use of the theory of mixtures. International Journal of Engineering Science, 1982. 20: 697–735.

Cerfontaine, B., Dieudonné, A.C., Radu, J.P., Collin, F. & Charlier, R. (2015): 3-D zero-thickness coupled interface finite element: Formulation and application. Computers and Geotechnics 69, 124–140. doi:10.1016/j.compgeo.2015.04.016.

Charlier, R. (1987) : Approche unifiée de quelques problèmes non linéaires de mécanique des milieux continus par la méthode des éléments finis. PhD Thesis, Université de Liège in Department ArGEnCo, Liège, Belgium.

Charlier, R., Radu, J.-P., Collin, F. (2011): Numerical modelling of coupled transient phenomena. Revue Française de Génie Civil 5, 719–741. doi:10.1080/ 12795119.2001.9692324.

CODE_BRIGHT User's Manual (2015): CODE_BRIGHT User's Manual, Technical University of Catalonia.

Collin, F. (2003) : Couplages thermo-hydro-mécaniques dans les sols et les roches tendres partiellement saturés. PhD Thesis, Université de Liège in Department ArGEnCo, Liège, Belgium.

Collin, F., Chambon, R. & Charlier, R. (2006): A finite element method for poro mechanical modelling of geotechnical problems using local second gradient models. International Journal for Numerical Methods in Engineering, 65(11):1749-1772.

Collin, F., Li, X.L., Radu, J.P. & Charlier, R. (2002): Thermo-hydro-mechanical coupling in clay barriers. Engineering Geology, 64(2-3):179-193.

Dixon, D., Chandler, N., Graham, J. & Gray, M.N. (2002): Two large-scale sealing test conducted at Atomic Energy of Canada's underground research laboratory: the buffer-container experiment and the isothermal test. Canadian Geotechnical Journal, 39:503-518.

Dupray, F. (2013): Statement regarding FEBEX in-situ experiment simulations of heating scenarios. Preliminary simulation note.

Dupray, F., François, B. & Laloui, L. (2011): Analysis of the FEBEX multi-barrier system including thermoplasticity of unsaturated bentonite. International Journal for Numerical and Analytical Methods in Geomechanics 37, 399–422. doi:10.1002/nag.

Dupray, F., François, B. & Laloui, L. (2013b): Analysis of the FEBEX Multi-barrier System Including Thermoplasticity of Unsaturated Bentonite. International Journal for Numerical and Analytical Methods in Geomechanics 37(4), 399–422.

Dupray, F., Lamure, E. & Laloui, L. (2013a): Study of the second phase of the real-scale in-situ test FEBEXe. technical report, EPFL- Nagra project 9499.

Enresa (1996): FEBEX. Full scale engineered barrier experiment in crystalline host rock. Test Plan.

Enresa (1998): FEBEX Pre-Operational Stage Summary Report. Publicaciones Técnicas 01/98, Enresa, Madrid, Spain.

Enresa (2000): FEBEX Project: Full-scale engineered barriers experiment for a deep geological repository for high level radioactive waste in crystalline host rock, Publicación técnica 1/2000, ENRESA.

Enresa (2004): FEBEX II Project Final report on thermo-hydro-mechanical laboratory tests, Publicación técnica 10/2004, ENRESA.

Enresa (2006a): Full-scale Engineered Barriers Experiment. Updated Final Report 1994-2004. Enresa Report 05-0/2006, Enresa, Madrid, Spain.

Enresa (2006b): FEBEX Project final report. Final report on the thermo-hydro-mechanical modelling. Enresa Report 05-2/2006, Enresa, Madrid, Spain.

François, B. & Laloui, L. (2008): ACMEG-TS: A constitutive model for unsaturated soils under non-isothermal conditions. International Journal for Numerical and Analytical Methods in Geomechanics 32, 1955–1988. doi:10.1002/nag.712

Fuentes-Cantillana, J.L. & García-Siñeriz, J.L (1998b): "FEBEX Full-scale Engineered Barriers Experiment in Crystalline Host Rock. FINAL DESIGN AND INSTALLATION OF THE "IN SITU" TEST AT GRIMSEL". Enresa Technical Report 12/98.

Fuentes-Cantillana, J.L., García-Siñeriz, J.L., Franco, J.J., Obis, J., Pérez A., Jullien, F., Alberdi, J., Barcala, J.M., Campos, R., Cuevas, J., Fernández, A.M., Gamero, E., García, M., Gómez, P., Hernández, A., Illera, A., Martín, P.L., Melón, A.M., Missana, T., Ortuno, F., Pardillo, J., Rivas, P., Turrero, M.J., Villar, M.V., Mingarro, M., Pelayo, M., Caballero, E., Cuadros, J., Huertas, F., Huertas, F.J., Jiménez de Cisneros, C., Linares, J., Bazargan-Sabet, B., Ghoreychi, M., Jockwer, N., Wieczorek, K., Kickmaier, W., Marschall, P., Martínez, M.A., Carretero, P., Dai, Z., Delgado, J., Juncosa, R., Molinero, J., Ruiz, A., Samper, J., Vázquez A., Alonso, E., Carrera, J., Gens, A., García-Molina, A.J., Guimera, J., Guimaraes, L.N., Lloret, A., Martínez, L., Olivella, S., Pintado, X., Sánchez, M., Elorza, F.J., Borregón, J.L., Canamon, I., Rodriguez, P., Esparver, R., Fariña, P., Farias, J. & Huertas, F. (2000): FEBEX full-scale engineered barriers experiment for a deep geological repository for high level radioactive waste in crystalline host rock Final Report. Enresa Technical Report 1/2000.

Fuentes-Cantillana, J.L., García-Siñeriz, J.L., Obis, J., Pérez, A., Alberdi, J., Barcala, J.M., Campos, R., Cuevas, J., Fernández, A.M., Gamero, E., García, M., Gómez, P., Hernández, A., Illera, A., Martín, P.L., Melón, A.M., Mingarro, M., Ortuno, F., Pardillo, J., Pelayo, M., Rivas, P., Rodríguez, V., Turrero, M.J., Villar, M.V., Caballero, E., Jiménez de Cisneros, C., Linares, J., Martínez, M.A., Samper, J., Delgado, J., Juncosa, R., Molinero, J., Alonso, E., Carrera, J., Gens, A., García-Molina, A.J., Guimera, J., Guimaraes, L.do N., Lloret, A., Martínez, L., Elorza, F.J., Borregón, J.L, Fariña, P., Farias, J. & Huertas, F. (1998a): "FEBEX Full-scale Engineered Barriers Experiment in Crystalline Host Rock. Pre-operational Stage Summary Report". Enresa Technical Report 1/98.

García-Siñeriz, J.L., Abós, H., Martínez, V., De la Rosa, C., Mäder, U. & Kober, F. (2016): FEBEX DP: Dismantling of heater 2 at the FEBEX "in situ" test. Description of operations. Nagra Arbeitsbericht NAB 16-11.

Gens, A. & Olivella, S. (2001): THM phenomena in saturated and unsaturated porous media. Revue Française de Génie Civil 5, 693–717. doi:10.1080/12795119.2001.9692323

Gens, A. (1995): Constitutive Laws. Modern issues in non-saturated soils. Springer-Verlag, 129-158.

Gens, A., Garcia-Molina, A., Olivella, S., Alonso, E.E. & Huertas, F. (1998): Analysis of a full scale in-situ test simulating repository conditions. International Journal for Numerical and Analytical Methods in Geomechanics, 22: 515- 548.

Gens, A., Sánchez, M., Guimaraes, L., Alonso, E.E., Lloret, A., Olivella, S., Villar, M.V. & Huertas, F. (2009): A full scale in situ heating test for high level nuclear waste disposal. Observations, analysis and interpretation. Géotechnique, 59(4): 377-399.

Gerard, P., Charlier, R., Chambon, R. & Collin, F. (2008): Influence of evaporation and seepage on the convergence of a ventilated cavity. Water Resources Research, 44: W00C02.

Huertas, F., Farina, P., Farias, J., Garcıa-Sineriz, J.L., Villar, M.V., Fernandez, A.M., Martın, P.L., Elorza, F.J., Gens, A., Sánchez, M., Lloret, A., Samper, J. & Martınez, M. A. (2006): Full-scale engineered barrier experiment, Updated Final Report, Technical Publication 05-0/2006. Madrid. ENRESA.

Hughes, T.J. (1980): Generalization of selective integration procedures to anisotropic and nonlinear media. International Journal for Numerical and Analytical Methods in Engineering, 15: 1413-1418.

Ikonen, K. (2003): Thermal analyses of spent nuclear fuel repository. Posiva report 2003-04.

Laloui, L. & François, B. (2009): Soil Thermoplasticity Model. Journal of Engineering Mechanics, 135(9):932-944.

Laloui, L. & Nuth, M. (2009): On the use of the generalised effective stress in the constitutive modelling of unsaturated soils. Computers and Geotechnics 36, 20–23. doi:10.1016/j.compgeo.2008.03.002.

Lanyon, G.W. & Gaus, I. (2013): Main outcomes and review of the FEBEX In Situ Test (GTS) and Mock-Up after 15 years of operation. Nagra. Arbeitsbericht NAB 13-96.

Lloret, A., Villar, M.V., Sánchez, M., Gens, A., Pintado, X. & Alonso, E.E. (2003): Mechanical behaviour of heavily compacted bentonite under high suction changes. Géotechnique; 53(1): 27-40.

Martínez, V., Abós, H. & García-Siñeriz, J.L. (2016): FEBEXe: Final Sensor Data Report (FEBEX in situ Experiment). Nagra Arbeitsbericht NAB 16-19.

Nuth, M. & Laloui, L. (2008). Effective stress concept in unsaturated soils: Clarification and validation of a unified framework. International Journal for Numerical and Analytical Methods in Geomechanics 32, 771–801. doi:10.1002/nag.645.

Olivella, S., Carrera, J., Gens, A., & Alonso, E.E. (1994): Non-isothermal multiphase flow of brine and gas through saline media. Transport in Porous Media 15, 271–293. doi:10.1007/BF00613282.

Olivella, S., Gens, A. & Mokni, N. (2012): Modelling the FEBEX in-situ experiment including dismantling operations – incorporating the effect of additional phenomena. Proceedings Clays in Natural and Engineered Barriers for Radioactive Waste Confinement. 5th international Conference. Montpellier, France, 633–634.

Olivella, S., Gens, A., Carrera, J. & Alonso, E.E. (1996): Numerical formulation for a simulator (CODE-BRIGHT) for the coupled analysis of saline media. Engineering Computations, 13(7): 87-112.

Panday, S. & Corapcioglu, M.Y. (1989): Reservoir transport equations by compositional approach. Transport in Porous Media, 4(4):369-393.

Pardillo, J., Campos, R. & Guimera, J. (1996): Caracterizatión Geológica del al zona de Ensayo FEBEX (Grimsel – Suiza). Ciemat FEBEX Report, 70-IMA-M-2-01.

Philip, J.R. & De Vries, D.A. (1957): Moisture movement in porous materials under temperature gradients. Transactions, American Geophysical Union, 38:222-232.

Pintado, X., Ledesma, A. & Lloret, A. (2002): Back-analysis of thermohydraulic bentonite properties from laboratory tests. Engineering Geology, 64(2-3):91-115.

Prager, W. (1949): Recent Developments in the Mathematical Theory of Plasticity. Journal of Applied Physics, 20(3):235-241.

Rey, M., Bárcena, I. & García-Siñeriz J.L. (2015): Full Dismantling Sampling Plan. Rev. 5. AITEMIN May 2015.

Rey, M., Sanz, J-L. & García-Siñeriz, J.L. (2016): FEBEX-DP Post-mortem analysis: Sensors. Nagra Arbeitsbericht NAB 16-20.

Romero, E., Villar, M.V. & Lloret, A. (2005): Thermo-hydro-mechanical behaviour of two heavily overconsolidated clays. Engineering Geology, 81(3):255-268.

Sánchez, M., Gens, A. & Guimarães, L. (2012b): Thermal–hydraulic–mechanical (THM) behaviour of a large-scale in situ heating experiment during cooling and dismantling. Canadian Geotechnical Journal 49, 1169–1195. doi:10.1139/t2012-076.

Sánchez, M., Gens, A. & Olivella, S. (2012a): THM Analysis of a large-scale heating test incorporating material fabric changes. International Journal for Numerical and Analytical Methods in Geomechanics, DOI: 10.1002/nag.1011.

Sánchez, M., Gens, A., Guimarães, L. & Olivella, S. (2008): Implementation algorithm of a generalized plasticity model for swelling clays. Computers and Geotechnics, 35: 860–871.

Svensson, D., Dueck, A., Nilsson, U., Olsson, S., Sandén, T., Lydmark, S., Jägerwall, S., Pedersen, K. & Hansen, S. (2011): Alternative buffer material. Status of the ongoing laboratory investigation of reference materials and test package 1. SKB TR-11-06, Svensk Kärnbränslehantering AB.

Tsang, C.F., Jing, L., Stephansson, O. & Kautsky, F. (2005): The DECOVALEX III Project: A Summary of Activities and Lessons Learned. International Journal of Rock Mechanics and Mining Sciences 42(5-6), 593–610.

van Genuchten, R. (1978): Calculating the unsaturated hydraulic permeability conductivity with a new closed-form analytical model. Water Resources Research, 37(11): 21-28.

Villar, M. V., Inglesias, R. J., Abós, H., Martínez, V., De la Rosa, C. & Manchon, M. (2016): FEBEX-DP on-site analyses report. Nagra Arbeitsbericht NAB 16-12.

Villar, M.V. (2002): Thermo-hydro-mechanical characterisation of a bentonite from Cabo de Gata: A study applied to the use of bentonite as sealing material in high-level radioactive waste repositories, Technical Publication 01/2002. Madrid: Enresa.

Villar, M.V., Garcia-Sineriz, J., Barcena, I. & Lloret, A. (2005): State of the Bentonite Barrier after Five Years Operation of an in-situ Test Simulating a High Level Radioactive Waste Repository. Engineering Geology 80, pp.175–198.